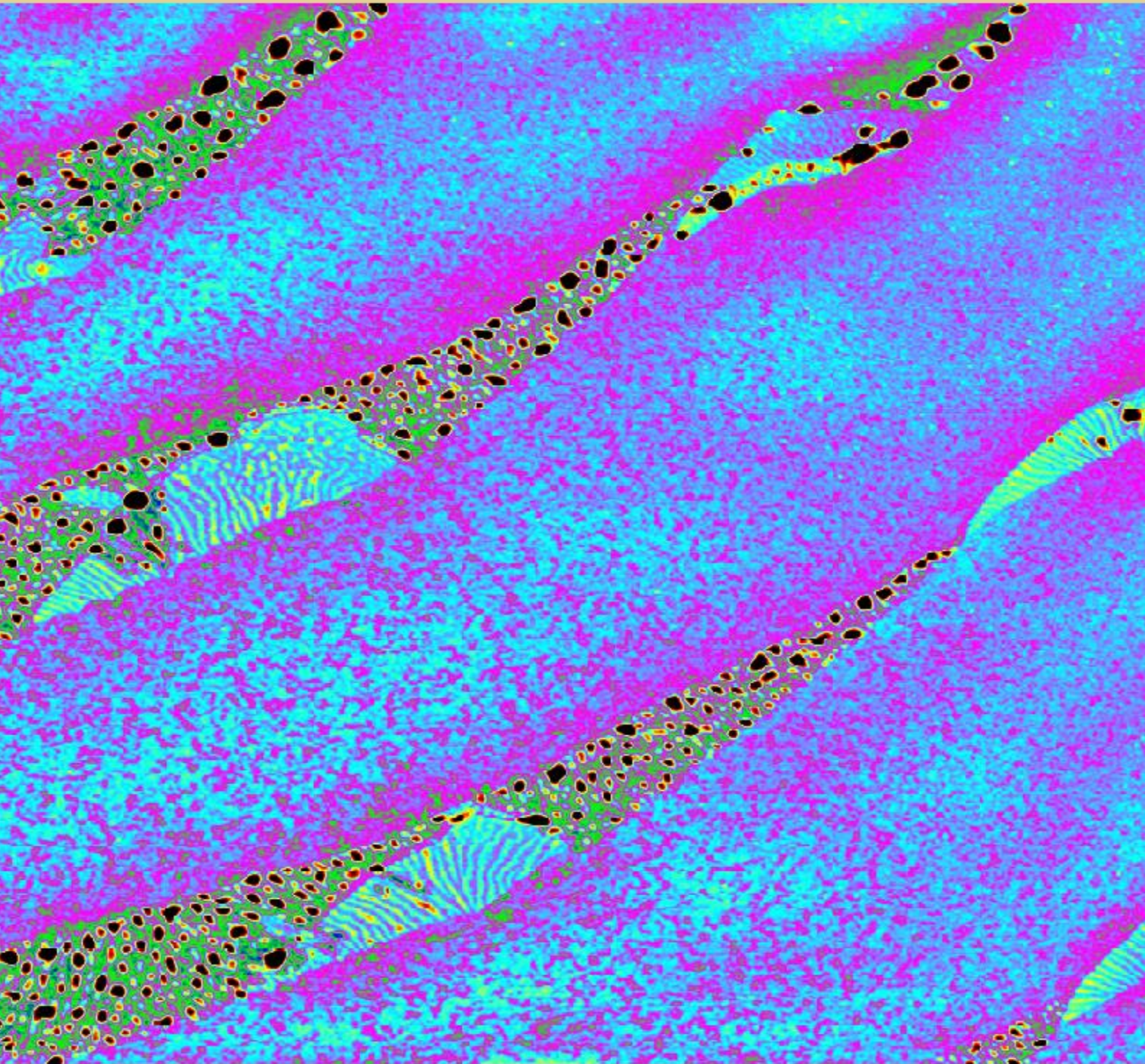


Volume 2, Number 4

December 2020

Nanomaterials Science & Engineering



Volume 2, Number 4

December 2020

Nanomaterials Science & Engineering

Title

Nanomaterials Science & Engineering (NMS&E), Vol.2, No.4, 2020

Editors-in-Chief

Igor Bdikin

Paula Alexandrina de Aguiar Pereira Marques

Duncan Paul Fagg

Editorial Board

Alexander Titov, Andrei Kovalevsky, António Manuel de Amaral Monteiro Ramos, António Manuel de Bastos Pereira, António Manuel Godinho Completo, Bagautdinov Bagautdin, Binay Kumar, Budhendra Singh, Cicero R. Cena, D. Pukazhselvan, Dmitry A. Kiselev, Dmitry Karpinsky, Eudes Borges de Araujo, Gil Gonçalves, Gonzalo Guillermo Otero Irueta, Indrani Coondoo, João Paulo Davim Tavares da Silva, José Coutinho, Maciej Wojtas, Manoj Kumar Singh, Margarida Isabel Cabrita Marques Coelho, Maxim Silibin, Münir Tasdemir, Neeraj Panwar, Nikolai Sobolev, Oleksandr Tkach, Paula Celeste da Silva Ferreira, Philip Leduc, Radheshyam Rai, Sergey Bozhko, Svitlana Kopyl, Vincent Ball, Vítor António Ferreira da Costa, Vladimir Bystrov, Yuri Dekhtyar

Editorial Managers

Igor Bdikin

Gil Gonçalves

Raul Simões

Cover and Logo

Igor Bdikin, Andrey Maljuk, A.B. Kulakov ($\text{Bi}_2\text{Sr}_2\text{CaCu}_2\text{O}_{8+x}$ single crystal, AFM image, $5 \times 5 \times 0.05 \mu\text{m}^3$)

Publisher

University of Aveiro

Support

Serviços de Biblioteca, Informação Documental e Museologia

Centre for Mechanical Technology & Automation (TEMA)

Mechanical Engineering Department

University of Aveiro

Copyright Information

All work licensed under Creative Commons Attribution License that allows others to share the work with an acknowledgement of the work's authorship and initial publication in this journal. Copyrights to illustrations published in the journal remain with their current copyright holders. It is the author's responsibility to obtain permission to quote from copyright sources.

Mailing Address

Department of Mechanical Engineering

University of Aveiro

Aveiro 3810-193

Portugal

E-mail: bdikin@ua.pt

ISSN: 2184-7002

Amel Bahfir, Messaoud Boumaour, Chaieb Zoubir, Hadjira Labeche Improved performance of Silicon solar cells by ZnMgO front layer	148-153
Milan Vukšić, Mihaela Ljubek, Irena Žmak, Lidija Ćurković Hybrid Microwave Sintering of Alumina Ceramics which Contain Waste Alumina	154-161
Martina Kocijan, Lidija Ćurković, Tina Radošević, Matejka Podlogar Photocatalytic degradation of organic pollutant using TiO₂/rGO nanocomposites under simulated sunlight	162-169
S.I. Latushka, D.V. Zhaludkevich, A.L. Zhaludkevich, A. Pakalniškis, A.N. Chobot, M.V. Silibin, G.M. Chobot, T.V. Latushka, R. Skaudžius, A. Kareiva, D.V. Karpinsky Crystal structure and magnetic properties of Bi_{1-x}Sm_xFeO₃ ceramics across the phase boundary: effect of high pressure	170-174
Miguel Fernandes and Francisco Brojo Carbon fiber reinforced polymer use in space launch vehicle propellant tanks - concept and finite element method study	175-182
V. S. Bystrov, E.V. Paramonova, A.V. Saprionova, Hong Shen, Xiangjian Meng, Jianlu Wang, L.A. Avakyan Modeling of the 2D-materials hybrid nanostructures based on Ferroelectric polymer PVDF/P(VDF-TrFE) and MoS₂ Dichalcogenide	183-196

Improved performance of Silicon solar cells by ZnMgO front layer

Amel Bahfir *, Messaoud Boumaour, Zoubir Chaieb, Hadjira Labeche

DDCS / Research Centre in Semiconductor Technology for Energetics (CRTSE). 2, Bd. Frantz Fanon, B.P. 140 -7 Merveilles, Algiers, Algeria

**Corresponding author, e-mail address: bahfir.amel@yahoo.fr, a.bahfir@crtse.dz*

Received 22 July 2020; accepted 1 December 2020; published online 15 December 2020

ABSTRACT

Silicon solar cells play a dominant role in the photovoltaic market. However, their manufacturing process is quite expensive and involves complex processes. Therefore, new materials are intensively explored for the aim of potentially higher efficiency and lower cost solar cells.

ZnMgO alloy is a very promising transparent conductive oxide layer and which acts as front layer as well as an anti-reflective coating in silicon solar cells reducing costs and complexity of process.

Numerical simulation using the SCAPS-1D software enables to find the optimized parameters of p-Si/ZnMgO hetero-junction in comparison with the structure comprising ZnO front layer. Even with the effect of stress caused by the high lattice mismatch at the ZnMgO/Si interface, our calculations show a conversion efficiency of 16.57%. Introduction of a thin layer of hydrogenated amorphous silicon improves the cell output performance to 17.14%.

1. INTRODUCTION

The main energy sources used today are fossil fuels, which represent more than 80% of current global primary energy demand, but their increasing consumption has led to serious environmental pollution and global warming [1, 2]. Solar energy, which is totally inexhaustible and sustainable has a double benefit: environmentally friendly and low cost energy sources [3, 4]. Since 2000 to 2013, the mean annual installation of solar panels increased by 48% [5].

Silicon-based solar cells play dominant role in production technology for electricity from sunlight [6]. They are prepared from either multicrystalline (mc-Si), crystalline (c-Si) or amorphous (a-Si) silicon substrates. The best silicon solar cell, developed by Kaneka Corporation, is able to achieve a conversion efficiency of 26.7% [7, 8]. However, the cells with best performance requires a very high cost and complicated processing techniques to reduce cost and improve the

manufacturing process. Recently, major work has been proposed to produce low cost devices using thin film technology [9, 10]. Recent research shows that the use of a transparent conductive oxide (TCO) on the front face with the silicon substrate facilitates the transport of charge carriers from the active layer to the metallic contact [11]. Among several TCO materials available, ZnO that is still under development has become a suitable front layer material due to the better optical and electrical properties [12].

The use of the ZnMgO alloy as TCO will further improve performance. Indeed, at low concentrations of Mg, ZnMgO has similar properties to ZnO with the advantage of being able to adjust the band gap with different levels of Mg content. The increase of Mg content increases the band gap from 3.2 to 3.9 eV. With a wider band gap, more incident light in the short wavelength region can be absorbed in the absorber layer. Furthermore, the interface between the front and absorbent layers can be adjusted appropriately by

adjusting the Mg / (Zn + Mg) ratio thus creating an optimal band alignment, which improves the transport of charge carriers [13].

2. DEVICE SIMULATION DETAILS

This new model of Si-based single heterojunction solar cells is modelled using the simulator SCAPS-1D (Solar Cell Capacitance Simulator - version 2.9.4) developed at the University of Gent [14]. It is based on the numerical resolution of the basic semiconductor device equations: Poisson equation as well as the hole and electron continuity equations, completed with appropriate boundary and limit conditions.

The parameters of each material used in the numerical simulation are presented in table 1. They have been carefully selected, based on data extracted from either experimental or other published values [15-17]. All numerical simulations for this work uses a surface recombination velocity of 10^7 cm/s, which corresponds more or less to the thermal agitation speed of the electrons [18]. AM1.5G illumination spectrum (incident light power 1000 W/m^2) was used as the incident light source based on the standards of the American Society for

Testing and Materials (ASTM). The operating temperature was set to 300K.

ZnO front layer presents a disadvantageous lattice mismatch ($> 40\%$) at the interface between ZnO and Si(100) which leads to high interfacial defect density ($5 \times 10^{14} \text{ cm}^{-2}$). When replacing ZnO by a $\text{Zn}_{1-x}\text{Mg}_x\text{O}$ alloy, the lattice constant of a-axis in the $\text{Zn}_{1-x}\text{Mg}_x\text{O}$ increases slightly with increasing Mg content, which slightly decreases the lattice mismatch at the Si/ $\text{Zn}_{1-x}\text{Mg}_x\text{O}$ interface.

This study was carried out for low Mg concentrations. Therefore, a slightly lower interfacial defect density was considered ($1 \times 10^{14} \text{ cm}^{-2}$).

3. RESULTS AND DISCUSSION

Several studies show that ZnO grown on Si is one of the inexpensive alternatives that can act both as an active n layer and as anti-reflection coating [16]. However, the poor lattice mismatch and high conduction band offset at the Si/ZnO interface are known to degrade the performance of cells.

Table 1. Baseline Values of Physical Parameters.

Material properties	p-Si	i-a-Si	n-ZnO	n-Zn _{1-x} Mg _x O
Layer Thickness (nm)	2.00E+5	5	2.00E+2	2.00E+2
Relative permittivity ϵ/ϵ_0	11.90	11.90	7.80	8.75
Electron mobility μ_n ($\text{cm}^2/\text{V.s}$)	1.04E+3	20	1.00E+2	1.00E+2
Hole mobility μ_p ($\text{cm}^2/\text{V.s}$)	2.5 E +1	5	2.50 E +1	2.50E +1
Acceptor concentration ($1/\text{cm}^3$)	2.0E+16	0	0	0
Donor concentration ($1/\text{cm}^3$)	0	0	1.0E+19	1.0E+19
Effective density of state N_c ($1/\text{cm}^3$)	2.8E+19	1.00E+20	2.22E+18	2.22E+18
Effective density of state N_v ($1/\text{cm}^3$)	1.04E+19	1.00E+20	1.8E+19	1.8E+19
Band gap E_g (eV)	1.12	1.72	3.3	3.208+1.509x
Electron affinity χ (eV)	4.05	3.9	4.5	4.6+0.16-1.056x

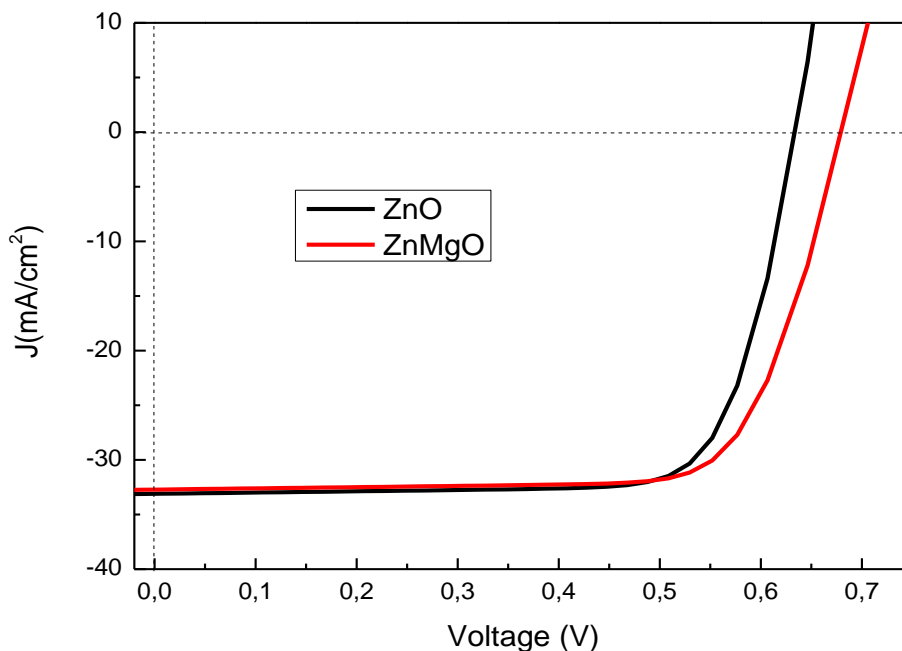


Figure 1. I-V curve of Si/ZnO compared to Si/ Zn_{0.8}Mg_{0.2}O.

Replacing ZnO by ZnMgO provides a significant improvement in the band alignment at the p-n heterojunction and a slight decrease in lattice

mismatch thanks to appropriate adjustment of the Mg concentration of ZnMgO ternary alloy.

A comparative study of both structures has been carried out. Figure 1 presents the I-V curve of

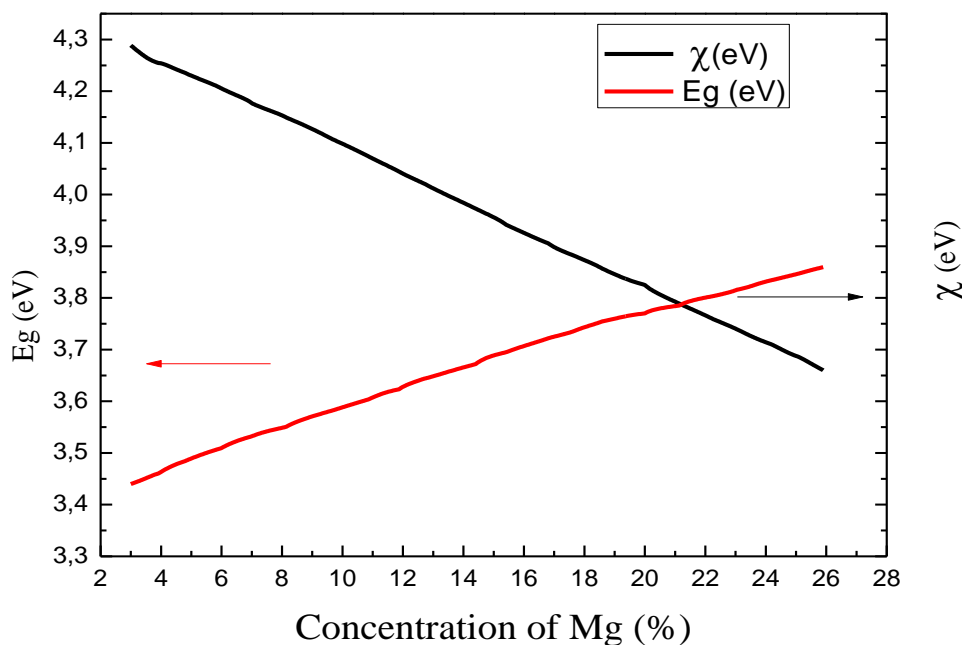


Figure 2. Band gap and electronic affinity as a function of the Mg content of ZnMgO.

Si/ZnO compared to Si/ZnMgO with 20% Mg. The results show almost similar J_{sc} values but the open-circuit Voltage ($V_{oc}=635.1$ mV) is lower than that of the Si/ZnMgO structure ($V_{oc}=655.0$ mV) which leads to a relative lower conversion efficiency ($\eta=16.10\%$), compared to 16.57% for Si/ZnMgO.

The effect of conduction and valence band offset (CBO, VBO) at the interface of ZnMgO/Si layers on output performance, have been theoretically studied. In fact, the optimization of the conduction/valence band offset in Si-based solar cells makes it possible to reduce the recombination of charge carriers.

The electron affinity (χ) and bandgap (E_g) variation of ZnMgO as a function of the Mg content is shown in figure 2. These values have been chosen based on literature where ZnMgO is used as a window layer in CIGS-based solar cells [19].

To keep the wurtzite phase, one should consider an Mg content below 30%. This is because of several experimental studies have argued that it can be considered as an upper limit due to the thermodynamic solubility limit of MgO in ZnO which is caused by precipitation of the secondary phases [20].

Variations of CBO and VBO at interface between Si and ZnMgO depending on the alloy composition are shown in figure 3.

The presence of a band offset in the form of a "spike" or a "cliff" results in an increase in the recombination current at the interface thus inducing a reduction in the conversion efficiency. This band offset is strongly influenced by the width of the bandgap and the electronic affinity of ZnMgO and Si. These two parameters are controlled by the Zn / Mg ratio.

The discontinuity in the conduction and valence band edges are given by:

$$\Delta E_c = \chi_{Si} - \chi_{ZnMgO} \quad (1)$$

$$\Delta E_v = \chi_{ZnMgO} - \chi_{Si} + (E_{g ZnMgO} - E_{g Si}) \quad (2)$$

Where ΔE_c , ΔE_v are conduction and valence band edge discontinuities, χ is electron affinity.

Figure 4 shows the detailed effects of Mg content on cell performance parameters. At the low concentration of Mg, V_{oc} , fill factor (FF) and short circuit current (J_{sc}) increase depending on the composition of the alloy and then remains almost stable beyond $x = 40\%$. The optimum Mg concentration is found at 20%.

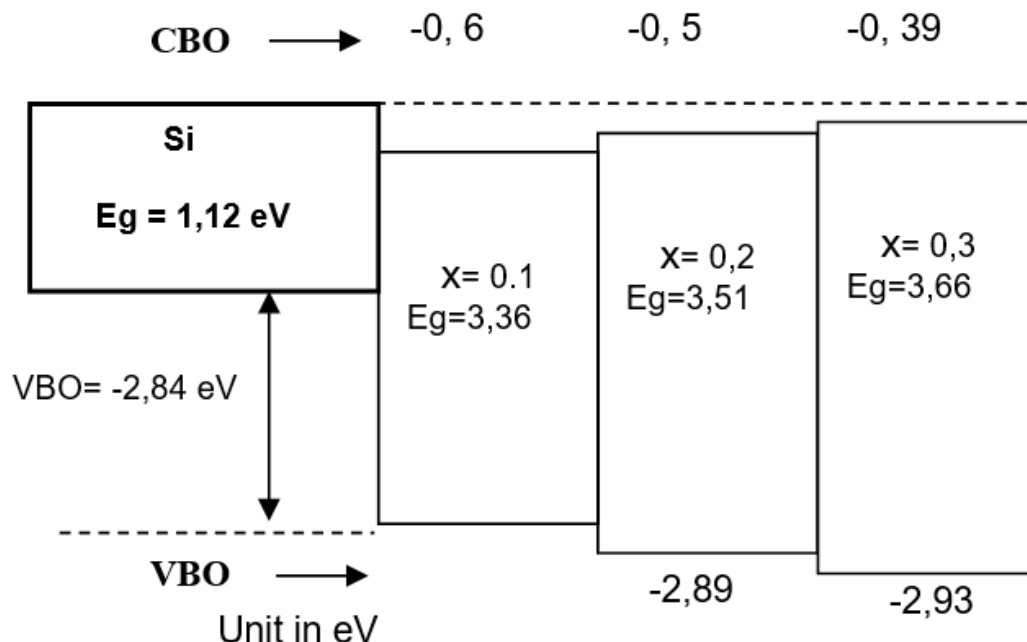


Figure 3. Band alignment at the Si/ Zn_{1-x}Mg_xO interface with different Mg concentration.

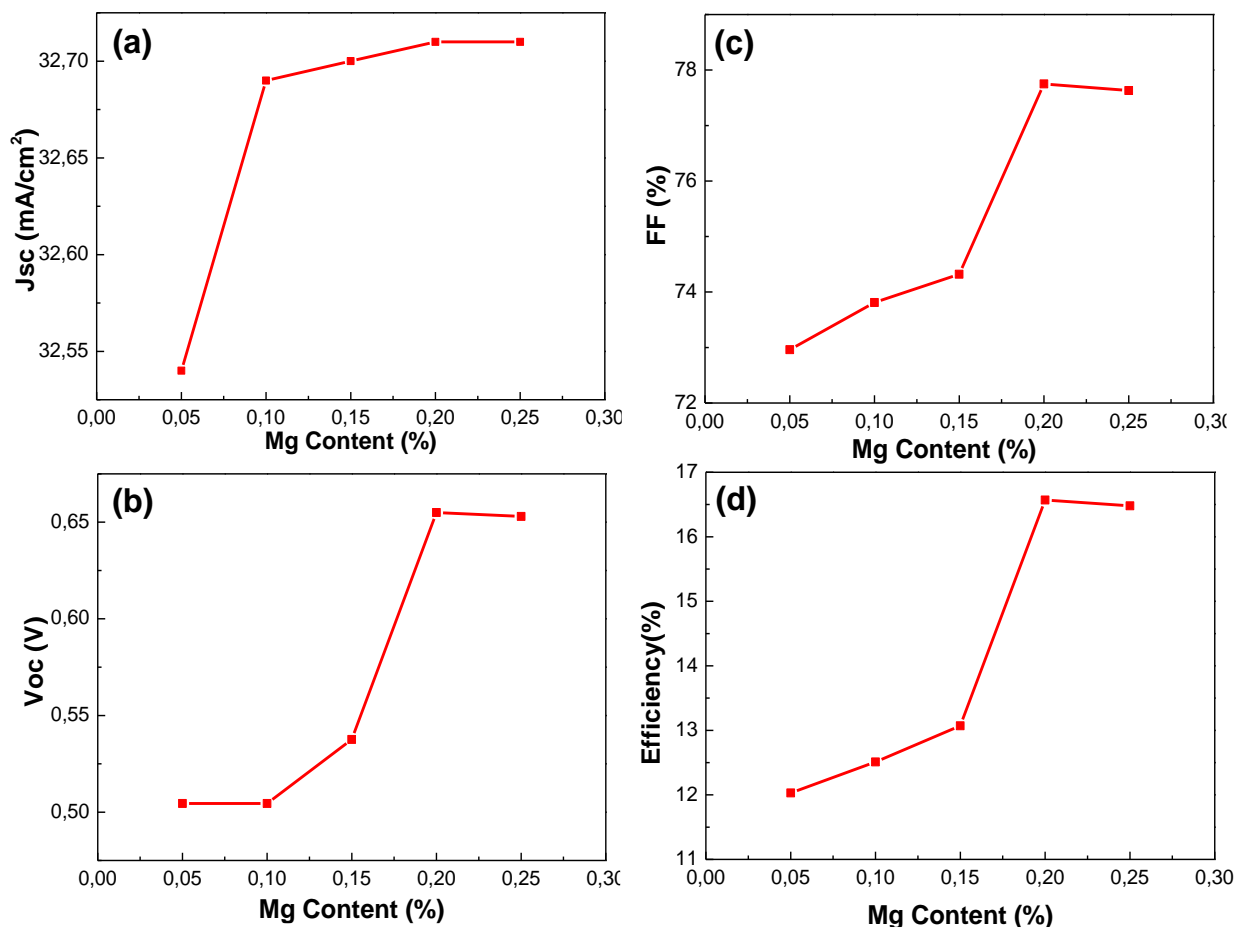


Figure 4. Performance of Si/ Zn_{1-x}Mg_xO cell with different Mg concentrations: (a) short circuit current , (b) open circuit voltage, (c) fill factor FF and (d) Conversion efficiency.

Although the CBO has a good band alignment, a slight degradation of performance is obtained beyond 25% due to the large VBO caused by widening of the bandgap of ZnMgO. The inclusion of a lower passivation layer using intrinsic silicon (i:a-Si) between Si and ZnMgO improves interface quality. Its optimal bandgap between the two hetero-interfaces can slow down the photon-

generated carrier recombination and induces a higher V_{oc} and J_{sc} , hence improved efficiency.

Table 2 summarizes the output performance of the Silicon solar cells with the different layers investigated in this work. similar efficiencies have been obtained for silicon structures with TCO layer [21].

Table 2. The simulated output performance for different structures.

Structure	V_{oc} (mV)	J_{sc} (mA/cm ²)	FF (%)	η (%)
Si/ZnO	635.1	33.11	76.57	16.10
Si/ZnMgO	655.0	32.54	77.57	16.57
Si/i-a-Si/ZnMgO	665.7	33.12	77.78	17.14

4. CONCLUSION

In summary, a comparative study of ZnO and ZnMgO front layers in Si-based solar cells have been analysed using Capacitance Simulator SCAPS-1D. The Mg content effect on conduction and valence band offset at the interface of ZnMgO/Si layers has been theoretically analysed. For a Mg concentration of 20%, the results demonstrate an optimal performance and an improvement relative to the pure ZnO. Cell performance is also closely related to interface defect states. The introduction of a thin intrinsic amorphous silicon layer significantly improves the cell output performance to 17.54%.

ACKNOWLEDGEMENTS

This work was funded under the Algerian General Directorate of Scientific Research and Technological Development (DGRSDT). Authors wish to acknowledge Marc Burgelman, University of Gent, Belgium for his kind provision of the SCAPS-1D solar cell simulator.

REFERENCES

- [1] N. Abas, A. Kalair, N. Khan, *Futures* **69**, 31- 49, (2015)
- [2] D. Gielen, F. Boshell, D. Saygin, M. D. Bazilian , N. Wagner, R. Gorini, *Energy Strategy Reviews* **24**, 38-50, (2019).
- [3] [A. Chel, G. Kaushik, *Alexandria Engineering journal* **57(2)**, 655-669, (2018).
- [4] D.N.F. Muche, S.A. Carminati, A. F. Nogueira, F. L. Souza, *Solar Energy Materials and Solar Cells* **208**, 1037, (2020).
- [5] A. Rawat, M. Sharma, D. Chaudhary, S. Sudhakar, S. Kumar, *Solar Energy* **110**, 691–703, (2014).
- [6] M.R. Sabour, M.A. Jafari, S.M.H. Gohar, *Silicon*, **12**, 2705-2720 (2020).
- [7] M. A. Green, E.D. Dunlop, J. Hohl-Ebinger, M. Yoshita, N. Kopidakis, & A.W.Y. Ho-Baillie, *Progress in Photovoltaics: Research and Applications*, **28(1)**, 3–15, (2020).
- [8] K. Yoshikawa, H. Kawasaki, W. Yoshida, T. Irie, K. Konishi, K. Nakano, T. Uto, D. Adachi, M. Kanematsu, H. Uzu, K. Yamamoto, *Nature Energy*, **2(5)**, 17032, (2017).
- [9] R. Pietruszka, B.S. Witkowski, E. Zielony, K. Gwozdz, E. Placzek-Popko, M. Godlewski, *Solar Energy*, **155**, 1282–1288, (2017).
- [10] S. Chala, N. Sengouga, F. Yakuphanoğlu, S. Rahmane, M. Bdirina, I. Karteri, *Energy*, **164**, 871-880, (2018).
- [11] F. Z. Bedia, A Bedia, M. Aillerie, N. Maloufi, F. Genty, B. enyoucef, *Energy Procedia*, **50**, 853–861. (2014).
- [12] B. Hussain, A. Ebong, I. Ferguson, *IEEE 42nd Photovoltaic Specialist Conference (PVSC)*, 15664803, (2015).
- [13] A. Bahfir, M. Boumaour, M. Kechouane, *Optik*, **169**, 196–202, (2018).
- [14] M. Burgelman, K. Decock, S. Khelifi, A. Abass, *Thin Solid Films* **535**, 296–301, (2013).
- [15] L. Chen, X. Chen, Y. Liu, Y. Zhao, X. Zhang, *Journal of Semiconductor*, **38**, 054005, (2017).
- [16] S.Vallisree, R.Thangavel, T. R. Lenkab , *Materials Research Express*, **6, No. 2**, (2018).
- [17] X Li, A. Kanevce, J. V. Li, I, Repins, B. Egaas, R. Nouf. *2009 34th IEEE Photovoltaic Specialists Conference (PVSC)*, (2009).
- [18] N. Touafek, R. Mahamdi, *International Journal of Renewable Energy Research*, **4, No.4**, 958-964 (2014).
- [19] K. E. Knutsen, R. Schifano, E. S. Marstein, B. G. Svensson, A. Yu. Kuznetsov, *Phys. Status Solidi A*, **210, No. 3**, 585–588. (2013).
- [20] A.Singh, A. Viji, D. Kumar, P. K. Khanna, M. Kumar, S. Gautam, K. H. Chae, *Semiconductor Science and Technology*, **28, No 2**, 025004, (2013).
- [21] A. Rawat, M. Sharma, D. Chaudhary, S.Sudhakar, S. Kumar, *Solar Energy*, **110**, 691-703, (2014).

Hybrid microwave sintering of alumina ceramics which contain waste alumina

Milan Vukšić*, Mihaela Ljubek, Irena Žmak and Lidija Ćurković

Faculty of Mechanical Engineering and Naval Architecture, Ivana Lučića 1, 10000 Zagreb, Croatia

**Corresponding author, e-mail address: milan.vuksic@fsb.hr*

Received 10 June 2020; accepted 1 December 2020; published online 15 December 2020

ABSTRACT

The use of microwave energy to sinter ceramic materials offers benefits compared to conventional sintering methods. Some of the benefits regarding less time consumption, achieving high heating rates and saving energy. The hybrid microwave sintering because of its advantages is a method of wide interest for improving the microstructure of sintered materials. In this study, the goal was to investigate the influence of the hybrid microwave sintering on the properties of alumina ceramics, which contain a considerable amount of waste alumina powder. The study was limited to hybrid microwave sintering of alumina green bodies in which the grain growth and densification were characterized. The waste alumina powder, which is generated during machining of alumina green compacts and high-purity (99.9 %) alumina powder, were used as starting materials. The alumina green bodies were obtained by the slip casting process. The dried green samples were then sintered by using a hybrid microwave furnace. The used hybrid microwave sintering atmospheric furnace consists of a 2.45 GHz microwave generator with a continuously adjustable power output from 0 to 3 kW and external heating elements. The sintered samples with the addition of waste alumina powder were showing higher density values, slightly smaller grain size, and higher linear shrinkage in comparison with the samples made of pure alumina powder. The observed microstructure for both samples was uniform with the average grain sizes smaller than 2 microns as a consequence of a hybrid microwave sintering.

1. INTRODUCTION

Sustainable development strategies of developed countries include the implementation of environmentally-friendly measures in terms of affecting production processes and efficient uses of the resource, as well as the generation and management of waste. The transformation of this waste into valuable materials is emerging as a possible solution to reduce environmental pollution. The reuse of recovered waste generated from the manufacturing processes involves the need for recycling as secondary raw materials [1-3]. This strategy is promoted by the recent Directive of the European Parliament and the Council on Waste (European Directive 2018/851) [4]. During the machining of the ceramic green body, a certain amount of waste ceramic powder is generated, which remains unused. Besides, the waste ceramic

powder should be disposed of as non-hazardous waste in a legally prescribed manner.

Alumina ceramics are interesting materials for researchers due to their excellent properties like high hardness, thermal, and chemical stability [5]. In recent years, continuous development can be observed in technologies of production of high-density sintered materials. A clear tendency exists in the research of methods, which use various dopants or sintering additives and require lower sintering temperatures and shorter process times [6]. In particular, magnesium oxide (MgO) is the most studied additive [7-9]. Various alternative additives have also been investigated to refine alumina ceramics microstructure by changing their composition, such as the addition of manganese oxide [10, 11], titan oxide [12, 13], graphene oxide [14-16], and many others.

Microwave sintering (MWS) has been studied as an alternative to conventional sintering to rapidly sinter and improve ceramic properties. During microwave heating, the energy is directly transferred to the material which couples with the electric field. Consequently, the material is self-heating from the interior, which allows rapid heating with suppressed grain growth. The microwave sintering has disadvantages such as the formation of a temperature gradient between the surface and core of heated materials with the low microwave dielectric loss. The poor microwave absorption occurs in some ceramic materials, including alumina ceramics (Al_2O_3). During microwave sintering of such ceramic materials, the thermal instabilities resulting in catastrophic overheating of the sintered sample were noticed [17-19].

However, these disadvantages can be overwhelmed by using hybrid microwave sintering, where direct microwave heating is combined with radiant (infrared) heating. In this way, the sample with low dielectric loss can be heated up to a temperature where it will begin to sufficiently absorb the microwaves. Also, uniform heating is achieved throughout the core and surface of the sample because the thermal gradients are significantly reduced. Based on these reasons, microwave hybrid sintering technique was proposed as a possible solution for microwave sintering of alumina ceramics [20-22].

In this study, the results of hybrid microwave sintering of alumina ceramic material which contains a considerable amount of waste alumina powder are presented. The optimal sintering conditions were determined by applying the Box-Behnken design. For the optimal conditions the final linear shrinkage, density, and microstructure characteristics were determined. Furthermore, the final densities, linear shrinkage, and microstructures of alumina samples prepared from commercial alumina powder were compared to the samples with the addition of waste alumina powder. The goal of this study was to investigate the possibility of recovering a non-hazardous waste alumina powder as secondary raw material in ceramic manufacturing processes, as an attempt to contribute to the sustainable development in terms of safe reuse of industrial waste.

2. MATERIALS AND METHODS

The components used in the study were commercially available Al_2O_3 (Alcan Chemicals, USA) with a chemical purity of 99.9% and the average particle size of 300-400 nm, waste (secondary) alumina powder which is obtained after green machining in factory production of ceramics. A commercial dispersant Tiron (4,5-dihydroxy-1,3-benzenedisulfonic acid disodium salt monohydrate) manufactured by Sigma-Aldrich Chemie GmbH, Germany was used to stabilize

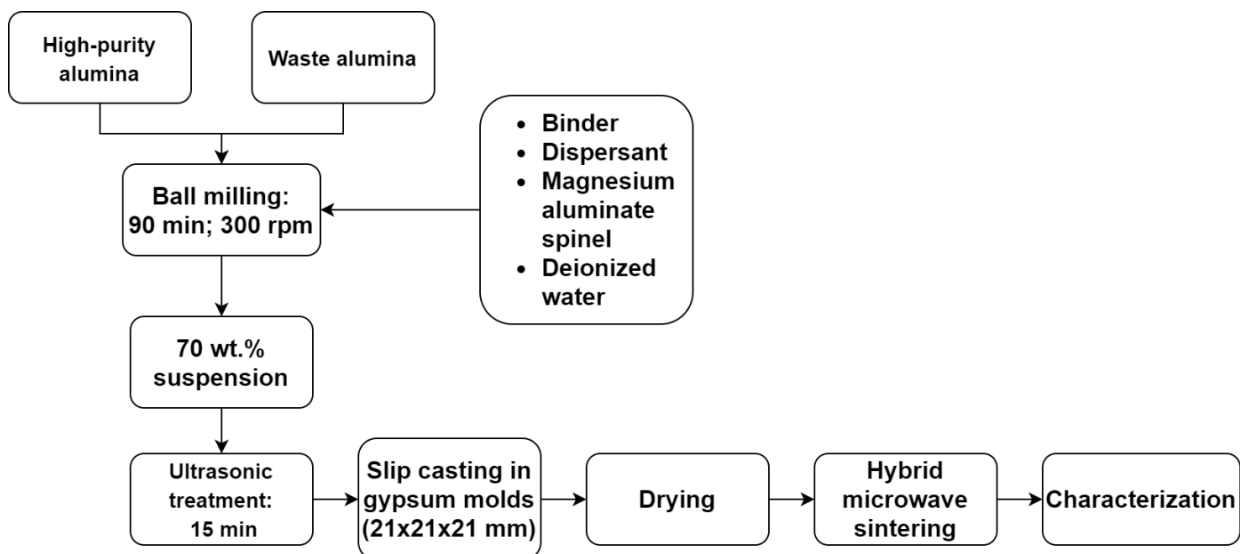


Figure 1. Process flow chart for sample preparation.

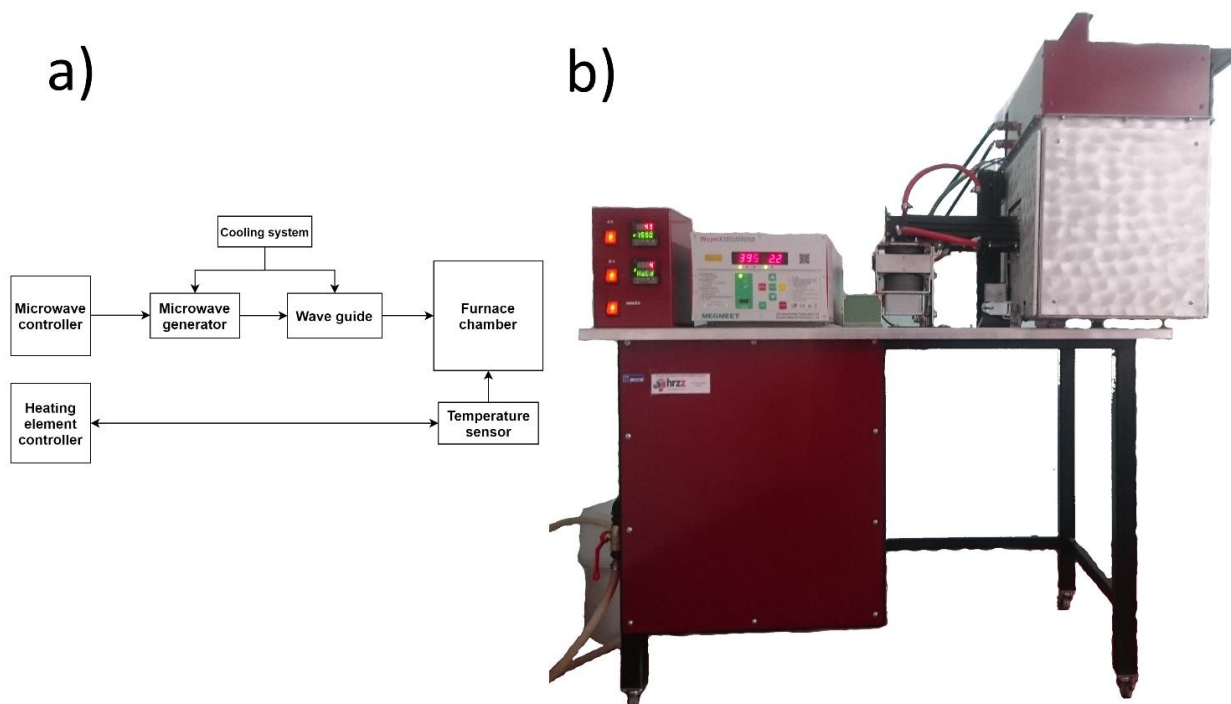


Figure 2. The schematic diagram (a) and photograph of the hybrid microwave furnace (b).

highly concentrated alumina suspensions [23]. The binder PVA manufactured by Sigma-Aldrich Chemie GmbH, Germany [24] was added to the ceramic suspension in order to improve the strength of the green bodies. Magnesium spinel (magnesium aluminate oxide) manufactured by Alfa Aesar, USA was used to inhibit the abnormal alumina grain growth during the sintering process of alumina green bodies [25].

The alumina samples were prepared through the procedure shown in Fig. 1. The mixture of dry alumina powders was prepared by mixing 20 wt.% of waste alumina powder versus 80 wt.% of high-purity alumina powder expressed on a dry weight basis of alumina powders. The solution of PVA – poly (vinyl alcohol) was prepared by dissolving the 0.1 wt.% of PVA in deionized water heated up to 80 °C. Afterwards, 0.05 wt.% of dispersant Tiron and 0.2 wt.% of magnesium aluminate spinel were mixed with the prepared solution and added into the grinding jar of the planetary ball mill PM 100 (Retsch GmbH, USA). Next, the previously prepared mixture of dry alumina powders was placed into the grinding jar of the planetary ball mill with ten alumina balls used for the suspension

homogenization. The homogenization lasted for 90 minutes at a speed of 300 rpm to make a suspension with a solids content of 70 wt.%. Alumina balls were separated from the suspension after the homogenization using a strainer (opening 2 mm). The suspension underwent an ultrasonic treatment for 15 min in an ultrasonic bath – BRANSONIC 220 (Branson Ultrasonics Corp., USA) to remove the air bubbles and achieve better homogeneity.

Finally, prepared suspensions were cast in gypsum molds (21x21x21 mm³) to prepare green alumina samples. In terms of comparison, the same experimental procedure was used to obtain pure alumina green samples just without the addition of waste alumina powder.

After drying, the green alumina samples were additionally cut into smaller pieces and sintered via a hybrid microwave furnace. The schematic diagram and photograph of the hybrid microwave furnace are given in Fig. 2., which was designed and made by OVER industrijska elektronika d.o.o., Kerestinec, Croatia.

The used hybrid sintering atmospheric furnace consists of a 2.45 GHz microwave generator with a

continuously adjustable power output from 0 to 3 kW and external (around the inner wall of the furnace) molybdenum disilicide heating elements. Temperature control is performed employing a thermocouple, which was positioned 1 cm from the sintered sample in order to avoid possible electric discharge at elevated temperatures. The furnace chamber was made of silicon carbide, which is commonly used as a susceptor material because of its excellent dielectric loss and oxidation resistance. By applying the Box-Behnken design the optimal sintering conditions were investigated. The input power of magnetron from 1 to 2 kW, sintering temperature from 1550°C-1650°C, and dwell time from 2-4 hours were monitored. The cooling rate of the samples in the furnace chamber was not controlled. After sintering and cooling, the microstructure analysis of the polished surface of sintered samples was conducted by a *Tescan Vega* scanning electron microscope (SEM). For determining the average grain size, the line intercept method was used. The bulk density of the samples was measured by using Archimedes principle by immersing in distilled water. The theoretical density of alumina for calculation of relative densities was taken as 3.98 g cm⁻³.

3. RESULTS AND DISCUSSION

In order to determine the optimal sintering conditions for alumina samples by using the experimental hybrid microwave furnace, the Box-Behnken design was applied.

The value range of each sintering factor was determined according to preliminary tests. The investigated range of sintering temperature was set from 1550 to 1650°C; the range of input power 1-2 kW; the range of holding time 2-4 hours. By combining the 3 factors at 3 levels a total sum of 15 experiments in randomized order, as per *Design Expert*® software, Box-Behnken response surface design was developed. The corresponding response, the density of each sintered sample was measured (Table 1). Then the response surface method was used to find out the optimal value of each factor to obtain maximum density.

By studying the ANOVA data (Table 2) the higher model *F*-value (34.35) and the associated lower *p*-value (*p*=0.0002) demonstrated that the polynomial regression model was suitable to determine the optimum sintering conditions of alumina ceramic samples, which contain 20 dwb. % waste alumina powder (expressed on dry weight basis dwb. %). The *p*-values less than 0.0500 indicate model terms are significant. In this case sintering temperature (*A*), holding time (*B*), as their interactions (*AB*, *AC*, *BC*, *B*², *C*²) were

Table 1. Box-Behnken design and experimental data.

Run	Factor A: Temperature, °C	Factor B: Holding time, h	Factor C: Input power, kW	Response: Density, g/cm ³	Predicted: Density, g/cm ³
1	1650	3	1	3.850	3.846
2	1600	3	1.5	3.857	3.859
3	1650	4	1.5	3.810	3.812
4	1600	2	1	3.841	3.843
5	1550	4	1.5	3.851	3.849
6	1550	3	1	3.845	3.844
7	1600	4	1	3.807	3.810
8	1600	2	2	3.827	3.824
9	1600	3	1.5	3.860	3.859
10	1550	3	2	3.846	3.851
11	1600	4	2	3.819	3.816
12	1650	3	2	3.825	3.826
13	1600	3	1.5	3.862	3.859
14	1650	2	1.5	3.856	3.858
15	1550	2	1.5	3.844	3.843

Table 2. ANOVA.

Source	Sum of Squares	df	Mean Square	F Value	p-value Prob > F
Model	0.0045	8	0.0006	34.35	0.0002
A- Temperature	0.0003	1	0.0003	15.61	0.0075
B-holding time	0.0008	1	0.0008	50.59	0.0004
C-Power	0.0001	1	0.0001	5.21	0.0625
AB	0.0007	1	0.0007	43.32	0.0006
AC	0.0002	1	0.0002	10.42	0.0179
BC	0.0002	1	0.0002	10.42	0.0179
B ²	0.0013	1	0.0013	79.72	0.0001
C ²	0.0011	1	0.0011	58.97	0.0006
Residual	0.0001	6	0.0000		
Lack of fit	0.0001	4	0.0000	3.34	0.2435
Pure Error	0.0000	2	6.333×10 ⁻⁶		
Cor Total	0.0046	14		R ²	0.9786
Std. Dev.	0.0040			Adjusted R ²	0.9501
Mean	3.84			Predicted R ²	0.8001
C.V. %	0.1049			Adeq. Precision	15.8499

significant. The remaining variable, input power of magnetron (C) showed negligible effect on the achieved density values according to high p-value ($p > 0.05$). High R^2 (0.979), $adjusted R^2$ (0.950), and smaller $predicted R^2$ (0.800) values indicate that the variation could be accounted for by the data satisfactorily fitting the model. Because of the higher difference between $predicted R^2$ and $adjusted R^2$ the model was tested by doing confirmation runs.

By applying multiple regression analysis on the experimental data, the following reduced quadratic

equation is obtained which describes the relationship between the dependent and the independent variables:

$$Y \left(\text{density, } \frac{\text{g}}{\text{cm}^3} \right) = +1.19734 + 0.001072 * A + 0.506298 * B + 0.579346 * C - 0.000265 * A * B - 0.000260 * A * C + 0.013000 * B * C - 0.018654 * B^2 - 0.069615 * C^2 \quad (1)$$

where A is sintering temperature (°C), B is holding time, and C is the input power of magnetron (kW).

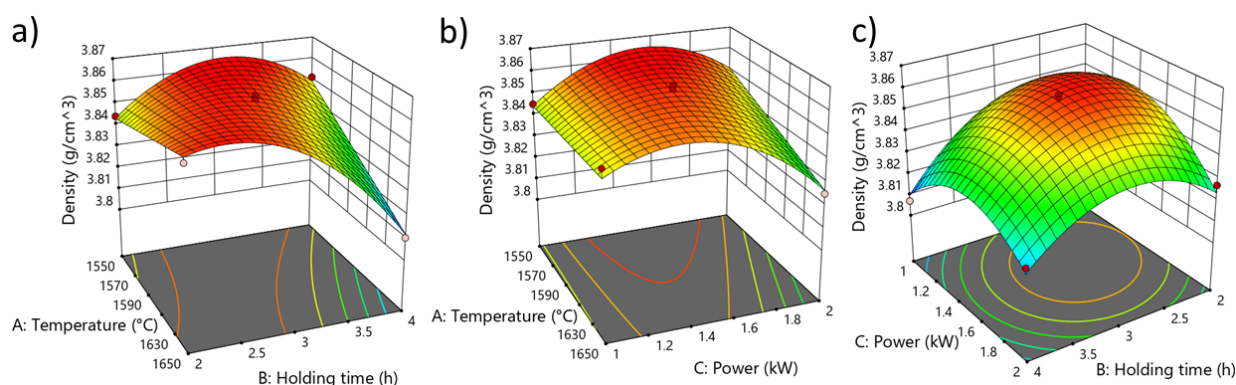


Figure 3. a-c) represents the response surface plots (3D) showing the effects of sintering parameters on the response density of sintered samples: a) fixed value of input power at 1.5 kW, b) fixed value of holding time at 3h, c) fixed value of sintering temperature at 1600 °C.

Table 3. The linear shrinkage of sintered samples.

	Total number	Dimensions	Shrinkage, %	Standard deviation
Pure alumina	30	a	7.59	2.83
	30	b	7.49	2.95
	30	c	8.03	4.08
20 dwb. % of waste alumina	30	a	9.24	1.93
	30	b	8.03	2.25
	30	c	8.53	2.56

Table 4. The obtained density values before and after sintering.

	Total number	Density, g/cm ³ (before sintering)	Standard Deviation	Density, g/cm ³ (after sintering)	Standard Deviation
Pure alumina	30	2.273	0.189	3.762	0.031
20 dwb. % of waste alumina	30	2.397	0.103	3.844	0.028

The criteria for optimization were set to maximize the density of sintered samples while keeping the independent variables in the investigated range. Based on Equation 1, multiple solutions were generated, where the ramp solution showed desirability of 1. Also, the obtained equation was used to calculate the predicted density values in Table 1. The determined optimum values were as follows, the sintering temperature of 1550°C, holding time in the duration of 2 hours, and the input power of 1.5 kW.

The determined optimal sintering conditions were tested by doing confirmation runs, which is usual practice for the empirical models. A total of 60 samples were sintered at optimal sintering conditions. More precisely, 30 samples with addition (20 dwb. %) of waste alumina powder and 30 samples without waste addition were sintered. After the sintering, linear shrinkage and density values were compared.

The determined linear shrinkage (Table 3), considering all three dimensions of sintered samples, is $7.69 \pm 3.31\%$ for the pure alumina samples and $8.13 \pm 2.26\%$ for waste alumina samples. The slight difference in the linear shrinkage can be explained by organic sintering

additives, which are present in the waste alumina. The organic components are removed during sintering, which results in higher shrinkage of sintered samples containing waste alumina.

The obtained density values before and after sintering are shown in Table 4. The determined density for the green samples is considerably lower than the density after the sintering process. The higher density values after sintering are a consequence of consolidating alumina particles during the sintering process. The density of green samples that contain waste alumina is higher than the density of samples without the addition of waste alumina powder. This difference also can be explained by sintering additives already present in waste alumina powder. Specifically, binders because their presence enhance the density of the green ceramic samples. The density after sintering remained higher for samples that contain waste alumina. Also, the calculated relative density suggests the presence of pores. The obtained relative density was $96.58 \pm 0.71\%$ for samples with the addition of waste alumina powder and 94.53 ± 0.78 respectively for pure alumina samples. The examined microstructure of the polished surface showed small, irregularly shaped alumina

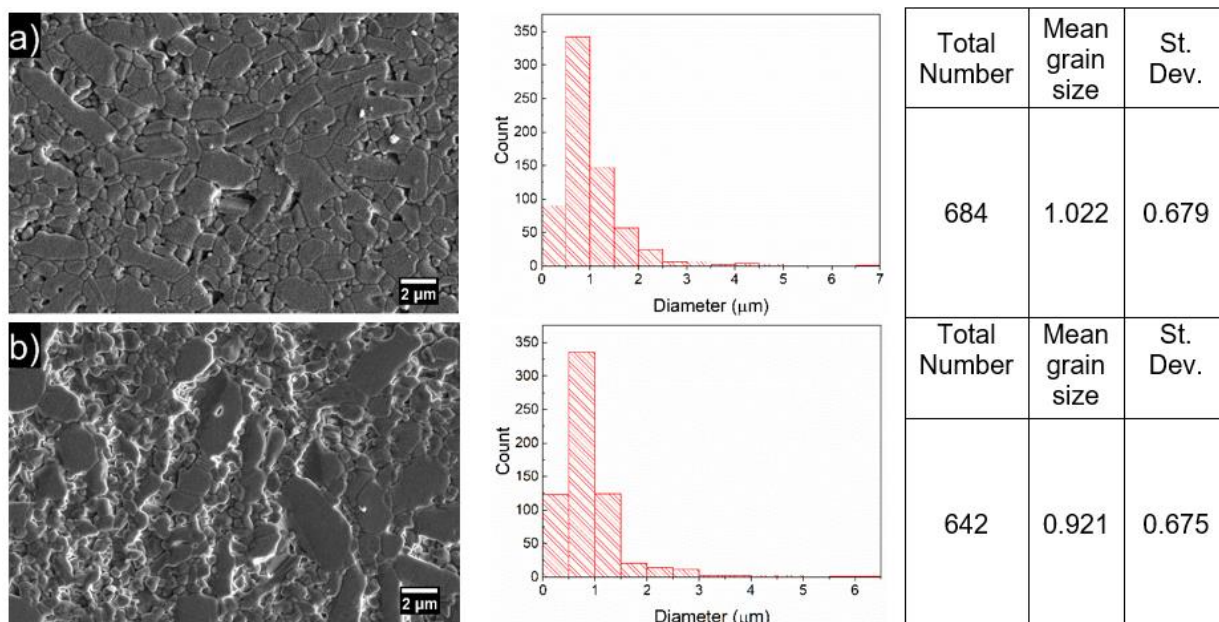


Figure 4. The micrographs of alumina samples a) pure alumina, b) with addition of waste alumina (20 dwb. %) and their corresponding grain size distribution from image analysis of SEM micrographs.

grains. The sample with the addition of waste alumina powder (Figure 4.b) showed a slightly smaller average grain size (0.92 ± 0.68) in comparison with the pure alumina sample (1.02 ± 0.68) as depicted in Figure 4.a). In general, the obtained average grain size for both compositions are smaller than 2 microns, which is a result of hybrid microwave sintering.

4. CONCLUSION

After the hybrid microwave sintering, the characterized samples with the addition of 20 dwb. % waste alumina powder exhibited slightly higher density values, smaller grain size, and higher linear shrinkage compared to samples prepared with pure alumina powder. The highest relative density was $96.58\pm 0.71\%$ for samples with the addition of waste alumina powder and 94.53 ± 0.78 respectively for pure alumina samples, which can be explained by the fact that alumina is a very poor microwave absorber. The average grain size was smaller than 2 microns for both observed compositions. The smaller grain size can be explained by the fact that the rapid heating of the microwave prevented grain size growth. The linear shrinkage was $7.69\pm 3.31\%$ for the pure alumina samples and $8.13\pm 2.26\%$ for waste

alumina samples. The slight difference in the linear shrinkage can be explained by organic sintering additives, which are present in the waste alumina powder. The burned organic components during sintering resulted in higher shrinkage of sintered samples containing waste alumina.

ACKNOWLEDGEMENTS

This work has been fully supported by Croatian Science Foundation under the project IP-2016-06-6000: Monolithic and Composite Advanced Ceramics for Wear and Corrosion Protection (WECOR).

REFERENCES

- [1] F. Andreola, L. Barbieri, I. Lancellotti, C. Leonelli, T. Manfredini, Recycling of industrial wastes in ceramic manufacturing: State of art and glass case studies, *Ceram. Int.* **42(12)**, 13333-13338 (2016).
- [2] M. Contreras, M.I. Martín, M.J. Gázquez, M. Romero, J.P. Bolívar, Valorisation of ilmenite mud waste in the manufacture of commercial ceramic, *Constr. Build. Mater.* **72**, 31-40 (2014).
- [3] A.S. El-Dieb, D.M. Kanaan, Ceramic waste powder an alternative cement replacement – Characterization and evaluation, *Sustain. Mater. Techno.* **17**, e00063 (2018).

- [4] Directive of the European Parliament and of the Council on Waste Amending Directive 2008/98/EC on Waste, in: EP (Ed.) 2018/851, Official Journal of the European Union, 2018.
- [5] E.G. Zemtsova, A.V. Monin, V.M. Smirnov, B.N. Semenov, N.F. Morozov, Formation and mechanical properties of alumina ceramics based on Al₂O₃ micro- and nanoparticles, *Phys. Mesomech.* **18(2)**, 134-138 (2015).
- [6] H. Li, X. Xi, J. Ma, K. Hua, A. Shui, Low-temperature sintering of coarse alumina powder compact with sufficient mechanical strength, *Ceram. Int.* **43(6)**, 5108-5114 (2017).
- [7] T. Ikegami, N. Iyi, I. Sakaguchi, Influence of magnesia on sintering stress of alumina, *Ceram. Int.* **36(3)**, 1143-1146 (2010).
- [8] K. Maca, V. Pouchlý, K. Bodišová, P. Švančárek, D. Galusek, Densification of fine-grained alumina ceramics doped by magnesia, yttria and zirconia evaluated by two different sintering models, *J. Eur. Ceram. Soc.* **34(16)**, 4363-4372 (2014).
- [9] D. Galusek, K. Ghillányová, J. Sedláček, J. Kozánková, P. Šajgalík, The influence of additives on microstructure of sub-micron alumina ceramics prepared by two-stage sintering, *J. Eur. Ceram. Soc.* **32(9)**, 1965-1970 (2012).
- [10] S.B. Dhuban, S. Ramesh, C.Y. Tan, Y.H. Wong, U. Johnson Alengaram, S. Ramesh, W.D. Teng, F. Tarlochan, U. Sutharsini, Sintering behaviour and properties of manganese-doped alumina, *Ceram. Int.* **45(6)**, 7049-7054 (2019).
- [11] S. Ramesh, S. Meenaloshini, C.Y. Tan, W.J.K. Chew, W.D. Teng, Effect of manganese oxide on the sintered properties and low temperature degradation of Y-TZP ceramics, *Ceram. Int.* **34(7)**, 1603-1608 (2008).
- [12] M. Sathiyakumar, F.D. Gnanam, Influence of MnO and TiO₂ additives on density, microstructure and mechanical properties of Al₂O₃, *Ceram. Int.* **28(2)**, 195-200 (2002).
- [13] H. Bian, Y. Yang, Y. Wang, W. Tian, H. Jiang, Z. Hu, W. Yu, Effect of Microstructure of Composite Powders on Microstructure and Properties of Microwave Sintered Alumina Matrix Ceramics, *J. Mater. Sci. Technol.* **29(5)**, 429-433 (2013).
- [14] T. Cygan, J. Wozniak, M. Kostecki, M. Petrus, A. Jastrzębska, W. Ziemkowska, A. Olszyna, Mechanical properties of graphene oxide reinforced alumina matrix composites, *Ceram. Int.* **43(8)**, 6180-6186 (2017).
- [15] C.F. Gutierrez-Gonzalez, A. Smirnov, A. Centeno, A. Fernández, B. Alonso, V.G. Rocha, R. Torrecillas, A. Zurutuza, J.F. Bartolome, Wear behavior of graphene/alumina composite, *Ceram. Int.* **41(6)**, 7434-7438 (2015).
- [16] J.-H. Shin, J. Choi, M. Kim, S.-H. Hong, Comparative study on carbon nanotube- and reduced graphene oxide-reinforced alumina ceramic composites, *Ceram. Int.* **44(7)**, 8350-8357 (2018).
- [17] M. Spotz, D. Skamser, D. Johnson, Thermal-Stability Of Ceramic Materials in Microwave-Heating, *J. Am. Ceram. Soc.* **78(4)**, 1041-1048 (2005).
- [18] K.I. Rybakov, E.A. Olevsky, E.V. Krikun, Microwave Sintering: Fundamentals and Modeling, *Journal of the American Ceramic Society* **96(4)**, 1003-1020 (2013).
- [19] Y. Chen, B. Fan, B. Yang, W. Ma, G. Liu, H. Li, Microwave sintering and fracture behavior of zirconia ceramics, *Ceram. Int.* **45(14)**, 17675-17680 (2019).
- [20] M.W. Khalid, Y.I. Kim, M.A. Haq, D. Lee, B.S. Kim, B. Lee, Microwave hybrid sintering of Al₂O₃ and Al₂O₃-ZrO₂ composites, and effects of ZrO₂ crystal structure on mechanical properties, thermal properties, and sintering kinetics, *Ceram. Int.* **46(7)**, 9002-9010 (2019).
- [21] M. Mizuno, S. Obata, S. Takayama, S. Ito, N. Kato, T. Hirai, M. Sato, Sintering of alumina by 2.45 GHz microwave heating, *J. Eur. Ceram. Soc.* **24(2)**, 387-391 (2004).
- [22] M. Bhattacharya, T. Basak, Susceptor-Assisted Enhanced Microwave Processing of Ceramics - A Review, *Crit. Rev. Solid State Mater. Sci.* **42**, 433-469 (2016).
- [23] B.J. Briscoe, A.U. Khan, P.F. Luckham, Optimising the dispersion on an alumina suspension using commercial polyvalent electrolyte dispersants, *J. Eur. Ceram. Soc.* **18(14)**, 2141-2147 (1998).
- [24] R. Taktak, S. Baklouti, J. Bouaziz, Effect of binders on microstructural and mechanical properties of sintered alumina, *Mater. Charact.* **62(9)**, 912-916 (2011).
- [25] Y. Emre, Effect of spinel addition on the sintering behavior and microstructure of alumina-spinel ceramics, *Ceram.-Silik.* **58(4)**, 314-319 (2014).

Photocatalytic degradation of organic pollutant using TiO₂/rGO nanocomposites under simulated sunlight

Martina Kocijan^{1,*}, Lidija Ćurković¹, Tina Radošević², Matejka Podlogar²

¹ Department of Materials, Faculty of Mechanical Engineering and Naval Architectur University of Zagreb, Ivana Lučića 5, 10000 Zagreb, Croatia

² Department for Nanostructured Materials, Jožef Stefan Institute, Jamova cesta 39, SI-1000, Ljubljana, Slovenia

*Corresponding author, e-mail address: martina.kocijan@fsb.hr

Received 6 June 2020; accepted 1 December 2020; published online 15 December 2020

ABSTRACT

Here, we present the development and performance of a nanocomposite photocatalyst based on titanium dioxide (TiO₂) and reduced graphene oxide (rGO). The material was prepared using a direct sol-gel method, followed by hydrothermal treatment. Different experimental conditions, such as time and temperature during the synthesis, were investigated with the aim to optimize photocatalytic degradation. The influence of the preparation conditions on the physicochemical properties of the synthesized powders was established by different characterization methods such as Scanning Electron Microscopy (SEM), and Raman spectroscopy. The effectiveness of the synthesized photocatalysts was examined through the photodegradation of caffeine under simulated sunlight irradiation. The influence of synthesized parameters on the TiO₂/rGO performance for the photodegradation of pharmaceutical caffeine was monitored by UV-Vis spectroscopy.

The obtained results show that the photocatalytic properties of the prepared TiO₂/rGO composites depend on different experimental parameters of their synthesis procedure, such as time and temperature. The TiO₂/rGO_6/400 composite presents a very efficient photo-degradation of caffeine by simulated sunlight irradiation, resulting in an efficiency of 95% within 90 minutes.

1. INTRODUCTION

At the beginning of the 21st century, mankind has to face the problem of unavailability of water as an important threat, due to the loss of the balance between the quantity and quality of this important resource. The ubiquitous pollutants such as drugs, pesticides, personal care products, and organic dyes, also known as emerging organic pollutants (EOP) have become a matter of increasing concern. They have raised considerable worries due to their frequent occurrence in drinking water, groundwater, and surface water, although in very low concentrations [1,2].

High concentrations of Caffeine (C₈H₁₀N₄O₂, CAF) can be found in natural sorts, such as cacao

seeds and coffee beans, and also in processed products (e.g. coffee, energy drinks, chocolates, and tea) [3–5]. The pharmaceutical industry is using CAF as an elementary compound for producing a variety of drugs that are used in medical therapy. Caffeine is the most frequently detected pharmaceutical in the groundwaters, and surface waters worldwide. The CAF in aqueous solutions, which has a high-water solubility of more than 10.0 mg/L, has negative effects on the environment. It is toxic for living organisms and it has a high resistance to natural degradation [3,4].

Advanced oxidation processes represent a facile route to remove EOP from the water and wastewater environment. Among them, photocatalysis [6,7], photo-Fenton [8], and

ozonation [9] appears the most appealing. Within this study, we investigated factors affecting the photocatalytic degradation of caffeine under simulated sunlight irradiation.

This study reports the photocatalytic degradation of CAF using TiO₂/rGO composites. Apart from the synthesis factors (time and temperature) affecting the photocatalytic degradation, an important aspect of this research was to understand how to synthesize the GO and TiO₂/rGO composites.

2. METHODS

2.1. Chemicals and Reagents

Commercially available natural graphite flakes (particle size $\leq 50 \mu\text{m}$) and titanium (IV) isopropoxide (Ti(C₃H₅O₁₂)₄, TTIP, 97%) were purchased from Sigma-Aldrich. Concentrated sulfuric acid (H₂SO₄, 95%-97%), and concentrated nitric acid (HNO₃, $\geq 65\%$) were obtained from Fluka and Lab Expert, respectively. Concentrated hydrochloric acid (HCl, 37%), potassium permanganate (KMnO₄), sodium nitrate (NaNO₃), hydrogen peroxide (H₂O₂, 30% w/v), *i*-propanol (C₃H₇OH), acetylacetone (CH₃(CO)CH₂(CO)CH₃) were supplied from Gram mol. The solutions with stated chemicals were prepared using ultrapure water (Millipore) obtained with a Direct-Q Millipore system.

2.2. Synthesis of graphene oxide (GO)

GO was synthesized by Hummer's method [10]. Firstly, flake-like graphite powder (3 g) was dispersed in H₂SO₄ (69 mL) and NaNO₃ (1.5 g) by magnetic stirring (30 min) at low temperature (0-5 °C). Then KMnO₄ (9.0 g) was dropwise added, to keep the reaction temperature lower than 20 °C. After addition, the mixture was heated to 35 °C and stirred for 30 min at which time water (138 mL) was slowly added. The process initiated an exothermic reaction, which gave rise to spontaneous heating to 98 °C. Additional heating was subsequently introduced to maintain the temperature at 98 °C for an additional 15 min, after which the reaction vessel was cooled down in a water bath. Additional water (420 mL) and 30% H₂O₂ (3 mL) were added one more time, resulting in another exothermic

reaction. After the reaction mixture was cooled to room temperature, the resultant suspension was centrifugated at 3000 rpm for 10 minutes to remove remaining impurities and to isolate the graphite oxide (GO). GO was first washed with dilute HCl (10%) and then with deionized water several times to produce a slurry of GO with a neutral pH.

2.3. Preparation of TiO₂ sol (colloidal solution)

TiO₂ sol was prepared using titanium (IV) isopropoxide (TTIP) as a precursor, *i*-propanol (PrOH) as a solvent, acetylacetone (AcAc) as a chelating agent and nitric acid (HNO₃) as a catalyst. The molar ratio of the reactants was: TTIP:PrOH:AcAc:HN = 1:35:0.63:0.015 [11].

2.4. Preparation of TiO₂/rGO nanocomposites

TiO₂/rGO composites were synthesized by the *in situ* procedure, using the TiO₂ colloidal sol prepared by the sol-gel route, which was hydrothermally treated in the presence of the GO substrates. The prepared slurry of GO was added into a colloidal solution of TiO₂ sol and stirred for 1 h until the liquid became a black-brown suspension. After that, the liquid was homogenized for 10 min in an ultrasonic bath. Subsequently, the suspension was transferred into a Teflon-lined autoclave and kept at 180 °C during the next 4 and 6 hours. The containers were removed from the oven and cooled to ambient temperature. The synthesized nanocomposite was washed to neutral pH value with *i*-propanol and deionized water and dried in an oven at 60 °C for 1 h. Finally, the synthesized powders were calcinated at 300 °C and 400 °C respectively. The obtained composites contained 5 wt.% of rGO and they were labelled TiO₂/rGO_4/300, TiO₂/rGO_6/400, TiO₂/rGO_4/300 and TiO₂/rGO_6/400.

2.5. Characterization of photocatalyst

The microstructural characteristics of the samples were obtained using scanning electron microscopy (SEM). Measurements were made with Jeol JEM-2100 equipment. The crystalline phases of the synthesized composites were analyzed by Raman microscope (NT-MDT Spectra II) using the Raman excitation energy at 633 nm.

2.6. Photocatalytic activity

To test the photocatalytic activity of the prepared nanocomposites, 9 mg of the synthesized photocatalyst were dispersed in the 9 mL of caffeine solution (10 mg/mL) and irradiated with simulated solar light (lamp: ULTRA-VITALUX, 230 V, 300 W, Osram) for 90 minutes. The degradation process was monitored by UV-Vis spectroscopy, taking aliquots at regular intervals (every 30 min). Each aliquot was centrifuged to remove the catalyst and, the resulting clear liquid was analyzed. The absorbance was recorded by a UV-Vis spectrophotometer (Lambda 950 Spectrophotometer, PerkinElmer) in the range from 200 to 400 nm using quartz cells with a path length of 10 mm.

Before the photocatalytic test, the prepared suspensions were kept in the dark for 30 minutes to achieve the adsorption equilibrium. The adsorption process in the dark was also monitored by UV-Vis spectroscopy.

3. RESULTS AND DISCUSSION

3.1. Characterization of photocatalyst

The representative morphologies of the synthesized GO and composites were evaluated by Scanning Electron Microscopy (SEM), as depicted in Fig.1. Fig.1A shows the SEM image of GO layers, indicating that GO is full of wrinkles and consists of thin layers. The size and the number of

layers is similar to reported investigations [12,13]. The morphology of the composite photocatalyst is significantly different compared to pure GO. Fig. 1B represents the TiO₂-rGO_6/300 composite. Small uneven agglomerates of TiO₂ particles can be found growing out from the GO surface [13].

The Raman spectra of synthesized materials are shown in Fig. 3. For both TiO₂-rGO composites, the characteristic peaks of the anatase phase are present. These peaks are at 158.5 cm⁻¹, 404.3 cm⁻¹, 519.5 cm⁻¹, and 638.7 cm⁻¹ for the sample TiO₂-rGO_6/300, and 157.3 cm⁻¹, 401.9 cm⁻¹, 521.7 cm⁻¹, and 644 cm⁻¹ for the sample TiO₂/rGO_6/400. Individual peaks are attributed to Eg, B1g, A1g+B1g, and Eg Raman modes. The rutile phase is not present in the synthesized composites [14]. Furthermore, it can be clearly seen that the Raman spectra of synthesized composites show characteristic peaks of graphene materials, which correspond to the D and G band (Table 1). The vibrations of the D and G peaks in rGO materials were significantly shifted compared to pure GO material. The laser excitation energy is the reason for the changes in peaks position in materials [13]. In our investigation, a laser with a wavelength of 633 nm was used. The reason for shifting is also in the changes of the graphene structure. Explicitly the G band represents the sp² hybridization in C-C bonds and the intensity of the D band corresponds to the sp³ hybridization which is in this structure associated with structural defects on the boundary [15]. Since the absolute intensity is difficult to determine from a solid-state sample



Figure 1. Synthesized graphene oxide slurry by Hummer's method.

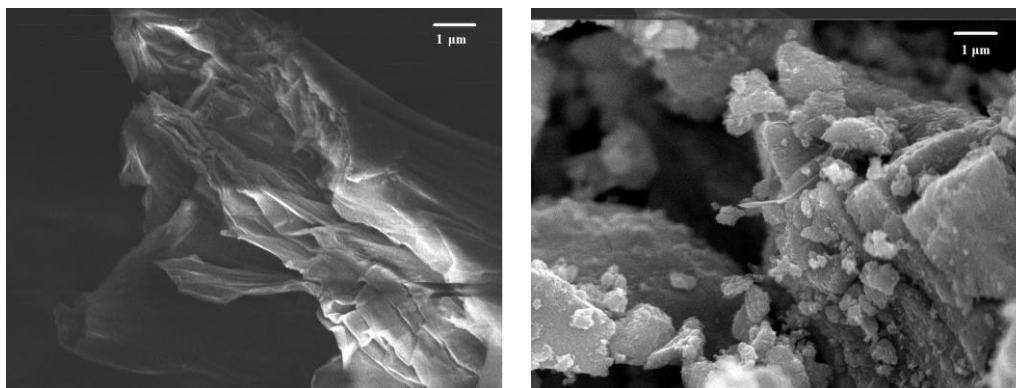


Figure 2. SEM images of synthesized GO (left image), and TiO₂-rGO_{6/300} composite (right image).

the intensity ratios between D and G peaks are more informative. It shows that the number of defects grows gradually from graphene where it is expectedly the smallest, to the composite with

TiO₂, where the ratio is the highest, as shown in Fig. 3 and Table 1.

The ratio of intensities between D and G bands is utilized to determine the crystal size parallel to basal planes (L_a), using the equation of Tuinstra

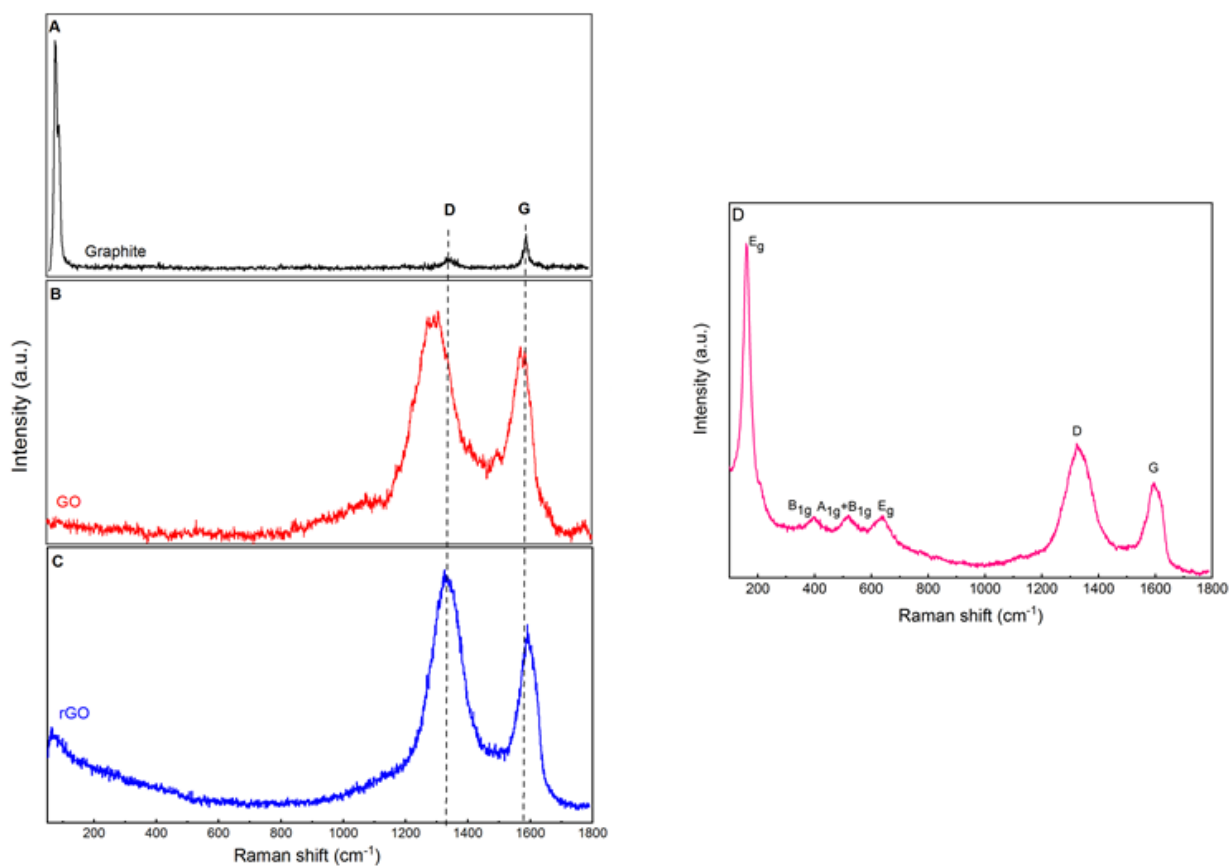


Figure 3. Raman spectra of (A) graphite, (B) graphene oxide (GO), (C) reduced graphene oxide (rGO), and (D) the respective TiO₂/rGO nanocomposite.

Table 1. Raman intensity and shift for the prepared materials.

Samples	D-band, cm^{-1}	I_D	G-band, cm^{-1}	I_G	I_D/I_G	L_a , nm
Graphite	1327.8	405	1583.5	579	0.70	55
GO	1348.0	139	1605.0	123	1.13	34
rGO	1325.8	774	1590.5	631	1.22	31
TiO ₂ /rGO_6/300	1331.0	327	1595.5	235	1.39	27

and Koenig, where the coefficient 38.5 is for measurements at 633 nm [16]:

$$L_a(\text{nm}) = \frac{38.5}{I_D/I_G} \quad (1)$$

The L_a values are 55 nm for graphite, 34 nm for GO, 31 nm for rGO, and 27 nm for TiO₂/rGO as shown

in Table 1. A lower L_a value demonstrates a decrease of sp^2 domains in the prepared materials.

3.2. Photocatalytic activity

The change in the maximum absorption peak for caffeine versus the irradiation time under simulated sunlight is shown in Fig. 4A-D. The maximum of the

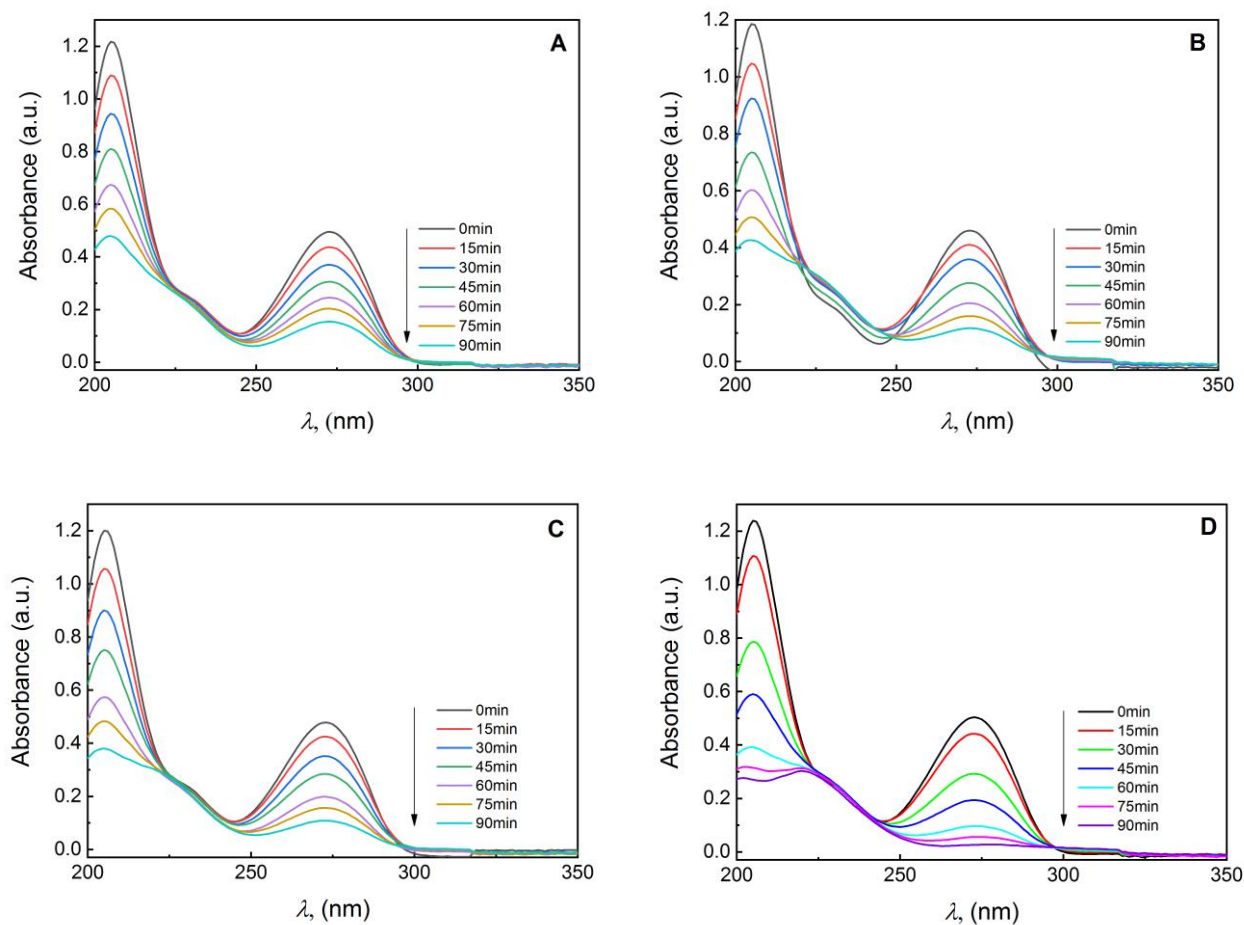


Figure 4. The absorption spectra for photo-degradation of caffeine as a function of irradiation interval in the presence of catalysts (A) TiO₂/rGO_4/300, (B) TiO₂/rGO_4/400, (C) TiO₂/rGO_6/300, and (D) TiO₂/rGO_6/400.

peak at 274 nm decreases with the longer irradiation time. The same trend can be observed for all four measured photocatalysts.

The performance of different TiO₂/rGO composites was evaluated based on the degradation of caffeine, shown in Fig. 5A. The degradation of caffeine was monitored through the change of its characteristic peak at 274 nm. Firstly, the adsorption in the dark was monitored for 30 minutes and subsequently, photocatalytic degradation of caffeine under simulated sunlight irradiation was measured, up to 90 minutes. Upon reaching the adsorption-desorption equilibrium (30 minutes), the irradiation source was turned on and the concentration of caffeine in the observed suspensions started to decrease, as seen in Fig. 5A. Results indicate that the caffeine was photo-degraded using the prepared TiO₂/rGO composites, as displayed in Fig. 5B.

The percentage of photoactivity of the synthesized photocatalysts, shown in Fig. 5C was calculated using the equation:

$$\eta = \frac{A_0 - A_t}{A_0} * 100\% \quad (2)$$

where, η is the percentage of the caffeine degradation, A_0 is the absorbance of the initial caffeine concentration (before irradiation) and A_t is the concentration of caffeine at time t , expressed as absorbance after irradiation at the determined time, t (min), during the whole photocatalytic process.

The first-order rate constant is calculated by the slope of the straight line obtained from plotting linear regression of $-\ln(A/A_0)$ versus irradiation time, t , as shown in Fig. 5D, and represented with the following equation [17]:

$$A_t = A_0 * e^{-k*t} \quad (3)$$

where, k (min⁻¹) is the degradation rate constant, A_t is the absorption of caffeine at the time of the photocatalytic process and A_0 is the absorption at the beginning of the experiment.

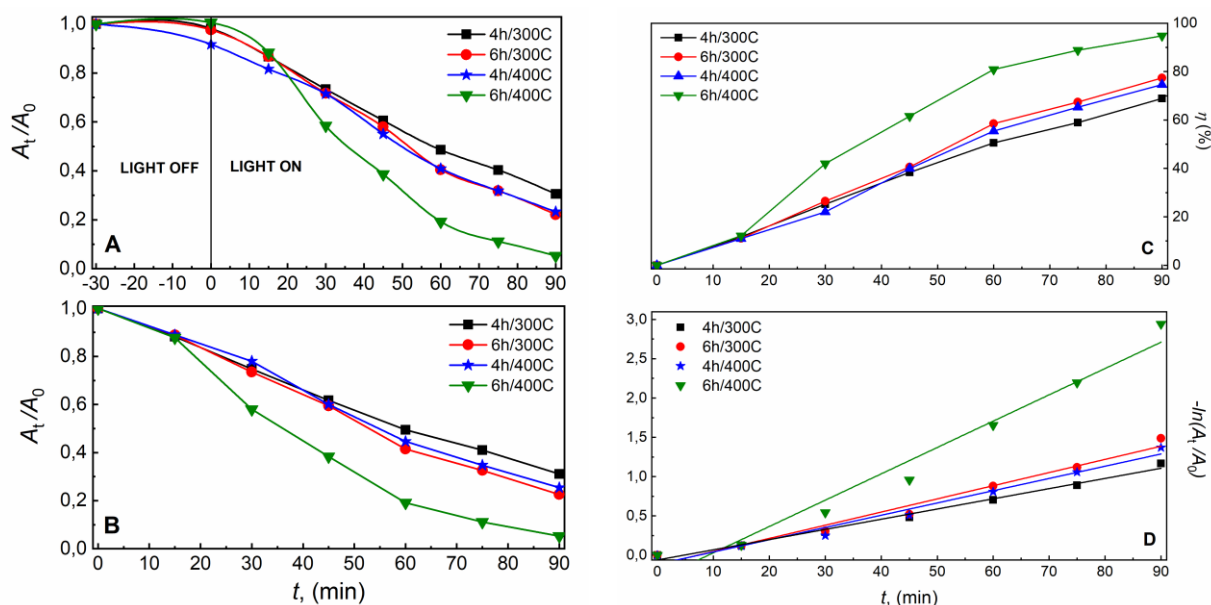


Figure 5. (A) Time evolution of CAF concentration in the presence of the as-prepared catalysts in the dark and under simulated sunlight irradiation, (B) time evolution of relative CAF concentration using synthesized composites, (C) photocatalytic degradation of CAF in percentage at different time, (D) first-order kinetic curves of the CAF degradation.

Table 2. Photo-degradation kinetics of caffeine under simulated sunlight irradiation.

Sample	R^2	$k \times 10^{-3}, \text{min}^{-1}$	$t_{1/2}, \text{min}$
TiO ₂ /rGO_4/300	0.9942	4.56	152.00
TiO ₂ /rGO_6/300	0.9880	7.12	97.35
TiO ₂ /rGO_4/400	0.9894	6.22	111.44
TiO ₂ /rGO_6/400	0.9882	19.5	35.55

The half-life ($t_{1/2}$) was calculated by the following equation [18]:

$$t_{1/2} = \frac{\ln(2)}{k} \quad (4)$$

Caffeine degradation efficiency increases from 69%, 75%, 77% to 95% for TiO₂/rGO_4/300, TiO₂/rGO_4/400, TiO₂/rGO_6/300, and TiO₂/rGO_6/400, respectively, after 90 min under simulated sunlight irradiation, Fig. 5C

In Table 2 the coefficient of determination (R^2), the reaction rate constant ($k \times 10^{-3}$), and half-life photo-degradation rate ($t_{1/2}$) are collected. The reaction rate constant and half-life of degradation were calculated for the composites, assuming the photo-degradation process followed the first-order kinetics model. The coefficient of determination is very high, proving first-order kinetics for the photocatalytic degradations. The reaction rate constant and the half-life degradation rate of TiO₂/rGO_4/300, TiO₂/rGO_4/400, and TiO₂/rGO_6/300 photocatalysts show slower removal of caffeine than TiO₂/rGO_6/400 photocatalyst, as depicted in Fig. 5A., the following was confirmed with constants in Table 2.

4. CONCLUSION

The GO was successfully prepared by Hummer's method. The TiO₂/rGO composites were effectively synthesized by exploring the two-step method that combines simple hydrothermal and calcination treatment. The successful synthesis of the composite was closely associated with the time of hydrothermal synthesis, and calcination temperature. Photocatalytic properties of powders

were determined by the degradation of caffeine under simulated sunlight irradiation.

These results show that the composites successfully synthesized with the proposed method can be used for the decomposition of caffeine by simulated sunlight. The TiO₂/rGO composites can also be used as highly efficient and "green" photocatalysts in effluent water treatment if the surface is exposed to sunlight.

REFERENCES

- [1] G. Luna-Sanguino, A. Tolosana-Moranchel, C. Duran-Valle, M. Faraldos, A. Bahamonde, Optimizing P25-rGO composites for pesticides degradation: Elucidation of photo-mechanism, *Catal. Today*. **328**, 172–177 (2019).
- [2] X. Sun, S. Ji, M. Wang, J. Dou, Z. Yang, H. Qiu, S. Kou, Y. Ji, H. Wang, Fabrication of porous TiO₂-RGO hybrid aerogel for high-efficiency, visible-light photodegradation of dyes, *J. Alloys Compd.* **819**, 153033 (2020).
- [3] M. Ghosh, K. Manoli, X. Shen, J. Wang, A.K. Ray, Solar photocatalytic degradation of caffeine with titanium dioxide and zinc oxide nanoparticles, *J. Photochem. Photobiol. A Chem.* **377**, 1–7 (2019).
- [4] A. Elhalil, R. Elmoubarki, M. Farnane, A. Machrouhi, M. Sadiq, F.Z. Mahjoubi, S. Qourzal, N. Barka, Photocatalytic degradation of caffeine as a model pharmaceutical pollutant on Mg doped ZnO-Al₂O₃ heterostructure, *Environ. Nanotechnology, Monit. Manag.* **10**, 63–72 (2018).
- [5] A.J.S.C. Vieira, E.M. Gaspar, P.M.P. Santos, Mechanisms of potential antioxidant activity of caffeine, *Radiat. Phys. Chem.* **174**, 108968 (2020).
- [6] R.R.N. Marques, M.J. Sampaio, P.M. Carrapiço, C.G. Silva, S. Morales-Torres, G. Dražić, J.L. Faria, A.M.T. Silva, Photocatalytic degradation of caffeine: Developing solutions for emerging pollutants, *Catal. Today*. **209**, 108–115 (2013).
- [7] M.K. Arfanis, P. Adamou, N.G. Moustakas, T.M. Triantis, A.G. Kontos, P. Falaras, *Chem. Eng. J.* **310**, 525-536 (2017).

- [8] A.G. Trovó, T.F.S. Silva, O. Gomes, A.E.H. Machado, W.B. Neto, P.S. Muller, D. Daniel, Degradation of caffeine by photo-Fenton process: Optimization of treatment conditions using experimental design, *Chemosphere*. **90**, 170–175 (2013).
- [9] R. Rosal, A. Rodríguez, J.A. Perdigón-Melón, A. Petre, E. García-Calvo, M.J. Gómez, A. Agüera, A.R. Fernández-Alba, Degradation of caffeine and identification of the transformation products generated by ozonation, *Chemosphere*. **74**, 825–831 (2009).
- [10] D.C. Marcano, D. V. Kosynkin, J.M. Berlin, A. Sinitskii, Z. Sun, A. Slesarev, L.B. Alemany, W. Lu, J.M. Tour, Improved synthesis of graphene oxide, *ACS Nano*. **4**, 4806–4814 (2010).
- [11] M. Čizmić, D. Ljubas, L. Ćurković, I. Škorić, S. Babić, Kinetics and degradation pathways of photolytic and photocatalytic oxidation of the anthelmintic drug praziquantel, *J. Hazard. Mater.* **323** 500–512 (2017).
- [12] S. Gurunathan, J.W. Han, V. Eppakayala, J.H. Kim, Green synthesis of graphene and its cytotoxic effects in human breast cancer cells, *Int. J. Nanomedicine*. **8**, 1015–1027 (2013).
- [13] E. Kusiak-Nejman, A. Wanag, J. Kapica-Kozar, Ł. Kowalczyk, M. Zgrzebnicki, B. Tryba, J. Przepiórski, A.W. Morawski, Methylene blue decomposition on TiO₂/reduced graphene oxide hybrid photocatalysts obtained by a two-step hydrothermal and calcination synthesis, *Catal. Today*. **357**, 630-637 (2019).
- [14] M. Mohammadi, M. Rezaee Roknabadi, M. Behdani, A. Kompany, Enhancement of visible and UV light photocatalytic activity of rGO-TiO₂ nanocomposites: The effect of TiO₂/Graphene oxide weight ratio, *Ceram. Int.* **45**, 12625–12634 (2019).
- [15] P. Wang, J. Wang, X. Wang, H. Yu, J. Yu, M. Lei, Y. Wang, One-step synthesis of easy-recycling TiO₂-rGO nanocomposite photocatalysts with enhanced photocatalytic activity, *Appl. Catal. B Environ.* **132–133**, 452–459 (2013).
- [16] M. Pawlyta, J.N. Rouzaud, S. Duber, Raman microspectroscopy characterization of carbon blacks: Spectral analysis and structural information, *Carbon* **84**, 479–490 (2015).
- [17] Y. Yang, L. Xu, H. Wang, W. Wang, L. Zhang, TiO₂/graphene porous composite and its photocatalytic degradation of methylene blue, *Mater. Des.* **108**, 632–639 (2016).
- [18] X. Zhou, S. Zhou, F. Ma, Y. Xu, Synergistic effects and kinetics of rGO-modified TiO₂ nanocomposite on adsorption and photocatalytic degradation of humic acid, *J. Environ. Manage.* **235**, 293–302 (2019).

Crystal structure and magnetic properties of $\text{Bi}_{1-x}\text{Sm}_x\text{FeO}_3$ ceramics across the phase boundary: effect of high pressure

S.I. Latushka^{1,*}, D.V. Zhaludkevich¹, A.L. Zhaludkevich¹, A. Pakalniškis², A.N. Chobot¹, M.V. Silibin^{1,3,4,5}, G.M. Chobot⁶, T.V. Latushka⁷, R. Skaudžius², A. Kareiva², D.V. Karpinsky^{1,3,**}

¹ Scientific-Practical Materials Research Centre of NAS of Belarus, 220072 Minsk, Belarus

² Institute of Chemistry, Vilnius University, LT-03225 Vilnius, Lithuania

³ National Research University of Electronic Technology "MIET", 124498 Zelenograd, Moscow, Russia

⁴ Scientific-Manufacturing Complex "Technological Centre", 124498 Zelenograd, Moscow, Russia

⁵ Institute for Bionic Technologies and Engineering, I.M. Sechenov First Moscow State Medical University, 119991 Moscow, Russia

⁶ Belarusian State Agrarian Technical University 220023 Minsk, Belarus

⁷ Belarusian State Medical University, 220116 Minsk, Belarus

*, ** Corresponding authors, e-mail: latushkasi@gmail.com; dmitry.karpinsky@gmail.com

Received 26 October 2020; accepted 1 December 2020; published online 15 December 2020

ABSTRACT

The solid solutions $\text{Bi}_{1-x}\text{Sm}_x\text{FeO}_3$ with chemical composition across the morphotropic phase boundary region specific for rhombohedral - orthorhombic structural transition were investigated by X-ray diffraction, electron microscopy and magnetometry. Structural measurements showed a concentration driven transition from the single phase rhombohedral structure to the single phase nonpolar orthorhombic structure through the formation of antipolar orthorhombic phase which coexists with the rhombohedral phase in the compounds with $x < 0.15$ followed by a coexistence with nonpolar orthorhombic phase in the compounds with $x \leq 0.18$. Application external pressure provides a stabilization of the orthorhombic phase, viz. the polar rhombohedral phase diminishes and transforms to the anti-polar orthorhombic phase, while the anti-polar orthorhombic phase transforms to the non-polar orthorhombic phase. Magnetic properties of the compounds subjected to external pressure demonstrate an increase in the magnetization of the compounds having dominant rhombohedral phase, wherein coercivity significantly increases, while the spontaneous magnetization remains nearly constant.

1. INTRODUCTION

Recently, the scientific community has seen widespread research focused on bismuth ferrite based materials [1,2,3]. Multiferroics based on BiFeO_3 are widely studied due to the great variability of chemical substitution methods that allow controlling chemical and physical properties in a wide range [4, 5]. Compounds with chemical composition near the structural phase transitions are of particular interest as such materials can be extremely sensitive to external influences as pressure, magnetic field, etc. while chemical

composition can be easily adjusted by chemical doping [6]. Multiferroics based on BiFeO_3 showing single phase or coexistent antipolar orthorhombic phase are of the specific interest due to their reduced structural stability in the phase boundary region controlled by chemical doping with rare earth elements [7].

Chemical substitution of bismuth ions by samarium ions leads to the formation of a single-phase antipolar orthorhombic phase in a narrow concentration range, up to 1% in the $\text{Bi}_{1-x}\text{Sm}_x\text{FeO}_3$ ceramics prepared by solid state reaction method [8], which attracts special attention, since the

concentration range described for the structural stability of the antipolar orthorhombic phase becomes extremely dependent on the conditions of preparation and processing of samples after synthesis [7, 9]. When using rare earth elements with an ionic radius smaller than that characteristic for samarium, a direct structural transition occurs from the rhombohedral to the nonpolar orthorhombic phase [10, 11].

This study shows a relationship between the type of structural distortions, the morphology of crystallites, and the appearance of remanent magnetization for Sm-doped BiFeO₃ compounds obtained by the sol-gel method as prepared and subjected to high pressure (5GPa). The results obtained show the difference in concentration-controlled phase transition observed for sol-gel powders having nanoscale crystallites, compared to the compounds having the same chemical composition after application of high pressure.

2. EXPERIMENTAL

Samples of Bi_{1-x}Sm_xFeO₃ compounds (x = 0.08, 0.12, 0.16, 0.18, 0.20) were obtained by the sol-gel method from components Bi(NO₃)₃·5H₂O, Fe(NO₃)₃·9H₂O, Sm₂O₃, and ethylene glycol. Initially, Sm₂O₃ was dissolved in 50 ml of H₂O, in which 2 ml of concentrated HNO₃ were previously dissolved. The solution was heated to 80 °C, the remaining compounds were added with constant stirring, after their dissolution, the solution was stirred for another 1 hour. After that, C₂H₆O₂ was added in a 2: 1 ratio to metal ions, after which it was stirred for another 1 hour. The resulting solution was evaporated at 200 °C. The resulting gel was dried for 12 hours at a temperature of 150 °C. The resulting xerogel was ground in an agate mortar and then heated in an oven for 1.5 hours at a temperature of 800 °C. Part of the compound Bi_{1-x}Sm_xFeO₃ was left as a powder, other part was pressed into tablets at high pressure (HP) of 5 GPa. X-ray diffraction patterns were recorded in the 2 theta range of 20 - 60° with a step of 0.02° using Bruker D8 Advance diffractometer with

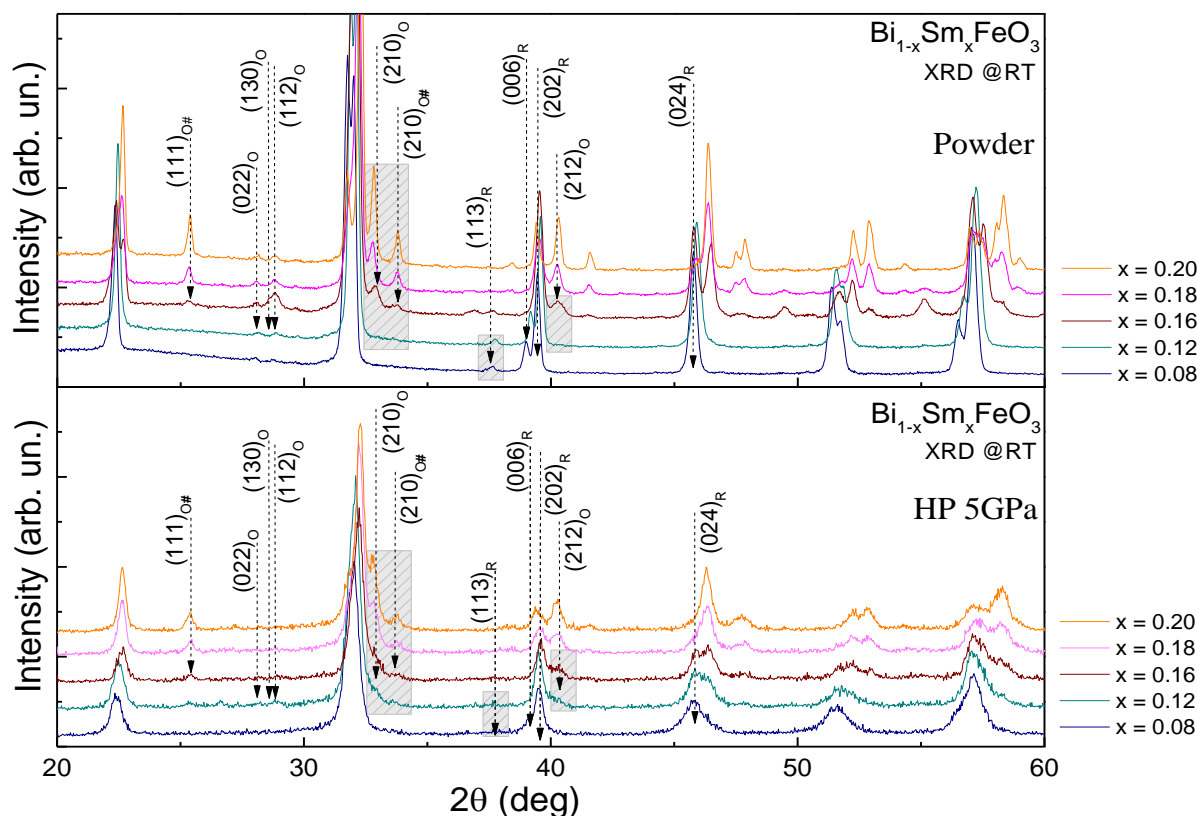


Figure 1. Room-temperature XRD patterns obtained for the compounds Bi_{1-x}Sm_xFeO₃ (x = 0.08, 0.12, 0.16, 0.18 and 0.20) as prepared (upper image) and after application of high pressure.

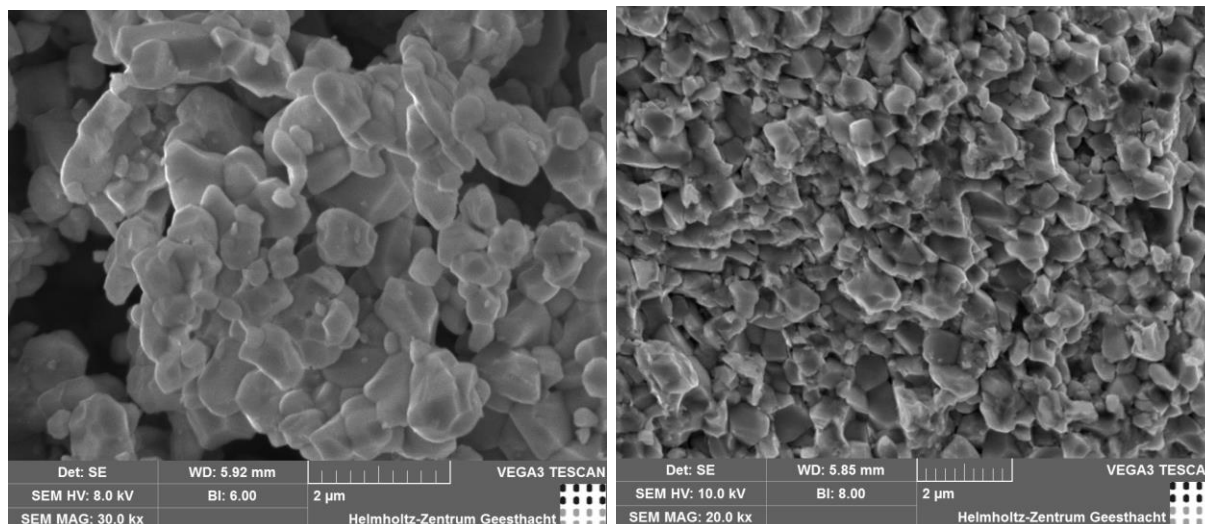


Figure 2. SEM images of the $\text{Bi}_{0.92}\text{Sm}_{0.08}\text{FeO}_3$ before (left) and after application of high pressure of ~ 5 GPa.

Cu-K α radiation. Magnetic measurements were performed at $T = 300$ K and magnetic fields up to ± 14 T using Physical Properties Measurement Systems from Cryogenic Ltd.

3. RESULTS AND DISCUSSION

The XRD data obtained for powder samples of the $\text{Bi}_{1-x}\text{Sm}_x\text{FeO}_3$ system ($x = 0.08, 0.12, 0.16, 0.18, 0.20$) showed that at low concentration of Sm

ions ($x < 0.12$) the compounds have a single-phase crystal structure with rhombohedral distortion of the unit cell similar to initial compound BiFeO_3 (Fig. 1).

The subsequent increase in the concentration of Sm ions ($x = 0.12$) results in the structural transition into the two-phase state characterized by a coexistence of orthorhombic and rhombohedral phases wherein there is a dominance of the rhombohedral phase with a small contribution of the antipolar orthorhombic phase. The XRD of the

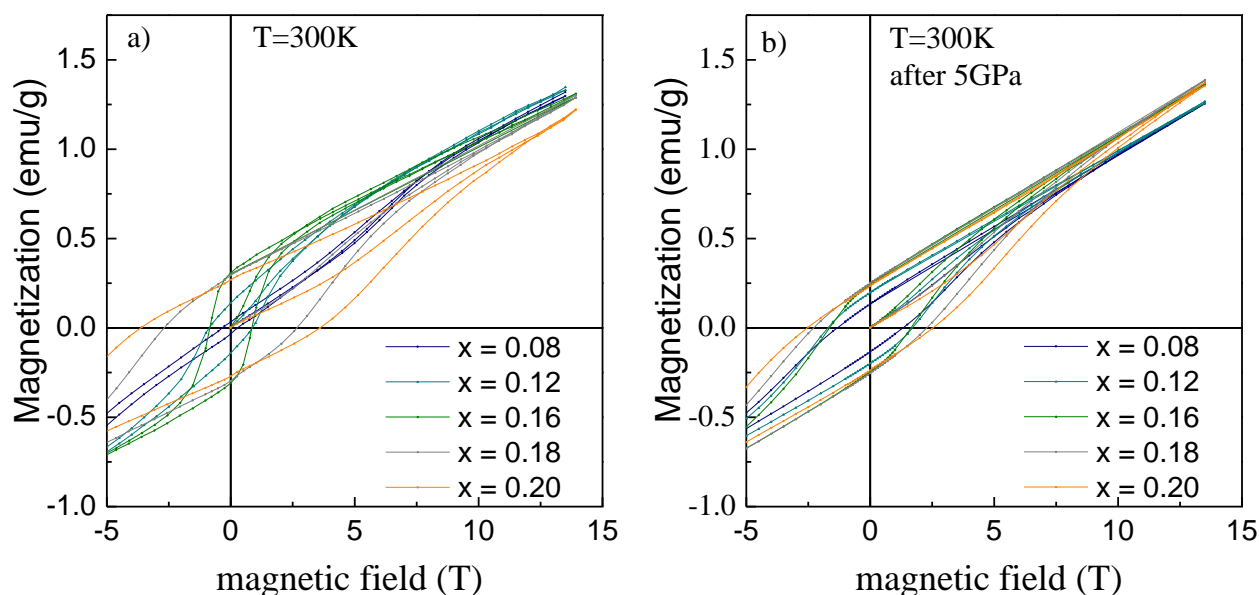


Figure 3. Magnetic field dependencies obtained for the compounds $\text{Bi}_{1-x}\text{Sm}_x\text{FeO}_3$ at temperature 300 K. a) as prepared compounds, b) compounds subjected to high pressure (~ 5 GPa).

compound with Sm content $x = 0.16$ also shows the two-phase structural state – a coexistence of the antipolar orthorhombic and the nonpolar orthorhombic phases with nearly equal phases content. The compound with Sm concentration $x = 0.18$ shows a two-phase crystal structure with a predominance of the non-polar orthorhombic distortions of the unit cell (Fig. 1).

The data obtained for the same compounds $\text{Bi}_{1-x}\text{Sm}_x\text{FeO}_3$ ($x = 0.08, 0.12, 0.16, 0.18, 0.20$) after application of a high pressure of 5 GPa showed the modification in the structural state of the compounds and crystallite morphology as confirmed by SEM measurements (Fig. 2). In the compound $\text{Bi}_{1-x}\text{Sm}_x\text{FeO}_3$ with $x = 0.12$, the amount of the antipolar orthorhombic phase is notably increased which is attested by the appearance of specific XRD reflections as $(210)_O$, $(212)_O$ and a decrease in the intensity of the $(113)_R$ peak. For compounds $x = 0.16, 0.18, 0.20$ a change in the phase ratio is also notable, which shows the diffusion of the reflections $(210)_O$, $(210)_{O\#}$ and $(212)_O$.

The study of the magnetization made it possible to determine the differences in the evolution of the magnetic properties of the $\text{Bi}_{1-x}\text{Sm}_x\text{FeO}_3$ compounds depending on the different concentration of the dopant ions and thus various structural states in the phase boundary region obtained in the form of a powder and after application of high pressure. In the compound $\text{Bi}_{0.92}\text{Sm}_{0.08}\text{FeO}_3$, the presence of the doping ions causes a reduction of the modulated magnetic structure characteristic of the BiFeO_3 compound; this modification occurs in magnetic field of 5T. The compound $\text{Bi}_{0.88}\text{Sm}_{0.12}\text{FeO}_3$ is characterized by a remanent magnetization of about $= 0.15$ emu/g. The compound with $x = 0.16$ has the antipolar structure and spontaneous magnetization of about 0.34 emu/g. In the compounds with $x \geq 0.18$, the magnetic structure is stabilized, the coercive force of the compounds increases notably, which is associated with a sharp decrease in the grain size and associated increase in magnetic anisotropy of the compounds (Fig. 3a). In spite of drastic modification of the structural state of the compounds from the rhombohedral phase to the nonpolar orthorhombic phase the evolution of the magnetic structure occurs monotonically.

For compounds $\text{Bi}_{1-x}\text{Sm}_x\text{FeO}_3$ ($x = 0.08, 0.12, 0.16, 0.18, 0.20$) subjected to high pressure, the coercivity corresponds to the powdered compounds with $x \sim 0.18$. This effect is associated with a decrease in the average crystallite size of the compounds (Fig. 2) which leads to increase in the magnetic anisotropy associated with orthorhombic structural phase observed in heavily doped compounds (Fig. 3b).

4. CONCLUSION

Based on the obtained results we conclude that in the powder compounds $\text{Bi}_{1-x}\text{Sm}_x\text{FeO}_3$ a release of the remanent magnetization is associated with a type of structural distortion, viz. the rhombohedral phase is characterized by nearly zero remanent magnetization while the orthorhombic phase with non-collinear orientation of the magnetic moments leading to non-zero remanent magnetization. An application external high pressure leads to a decrease in the average grain size of the compounds and thus to a release of remanent magnetization. A release of remanence is associated with uncompensated average magnetic moments ascribed to non-collinear orientation of the magnetic moments in the orthorhombic phases as well as an appearance of non-zero magnetization due to reduced grain size lower than a modulation period of the spatially modulated spin structure ascribed to initial BiFeO_3 .

ACKNOWLEDGEMENTS

This work was supported by the RFBR (projects # 20-58-00030), BRFFR (projects # F20R-123 and # T20R-121).

REFERENCES

- [1] A. Ghosh, D.P. Trujillo, H. Choi, S.M. Nakhmanson, S.P. Alpay, J.-X. Zhu, *Scientific Reports* **9**(1), 194 (2019).
- [2] S.H. Han, K.S. Kim, H.G. Kim, H.-G. Lee, H.-W. Kang, J.S. Kim, C. I. Cheon, *Ceramics International* **36**(4), 1365-1372 (2010).
- [3] W. Xing, Y. Ma, Z. Ma, Y. Bai, J. Chen, S. Zhao, *Smart Materials and Structures* **23** (8), 085030 (2014).
- [4] I. O. Troyanchuk; D. V. Karpinsky; M. V. Bushinsky; O. S. Mantyskaya; N. V. Tereshko; V. N. Shut, *J. Am. Ceram. Soc.* **94** (12), 4502-4506 (2011).

- [5] D. A. Rusakov; A. M. Abakumov; K. Yamaura; A. A. Belik; G. Van Tendeloo; E. Takayama-Muromachi, [Chem. Mater.](#) **23(2)**, 285 (2010).
- [6] D.C. Arnold, [IEEE Transactions on Ultrasonics, Ferroelectrics, and Frequency Control](#) **62(1)**, 62-82 (2015).
- [7] M. Kubota, K. Oka, Y. Nakamura, H. Yabuta, K. Miura, Y. Shimakawa, M. Azuma, [Japanese Journal of Applied Physics](#) **50(9)**, 09NE08 (2011).
- [8] D.V. Karpinsky, A. Pakalniškis, G. Niaura, D.V. Zhaludkevich, A.L. Zhaludkevich, S.I. Latushka, M. Silibin, M. Serdechnova, V.M. Garamus, A. Lukowiak, W. Stręk, M. Kaya, R. Skaudžius, A. Kareiva, [Ceramics International](#) (2020) (in press).
- [9] S. Liu, H. Luo, S. Yan, L. Yao, J. He, Y. Li, L. He, S. Huang, L. Deng, [Journal of Magnetism and Magnetic Materials](#) **426**, 267-272. (2017).
- [10] Y. Zheng, R. Ran, Z. Shao, [Rare Metals](#) **28(4)**, 361-366 (2009).
- [11] S. Cho, C. Yun, Y.S. Kim, H. Wang, J. Jian, W. Zhang, J. Huang, X. Wang, H. Wang, J.L. MacManus-Driscoll, [Nano Energy](#) **45**, 398-406 (2018).

Carbon fiber reinforced polymer use in space launch vehicle propellant tanks - concept and finite element method study

Miguel Fernandes* and Francisco Brojo

Aerospace Sciences Department, University of Beira Interior. Convento de Sto. António. 6201-001 Covilhã. Portugal

**Corresponding author, e-mail address: mig_16_ang@hotmail.com*

Received 10 June 2020; accepted 10 December 2020; published online 15 December 2020

ABSTRACT

Weight reduction is a never-ending goal in aerospace engineering, especially for a space launch vehicle (SLV), where every gram of mass has a penalty in the vehicle's performance. Since propellant tanks generally weigh more than half of the dry mass of a SLV, it is particularly advantageous to implement composite materials in their construction. Yet, difficulties with oxygen compatibility, permeability and manufacturing maturity dictate that aluminium alloys with high lithium content are still the state of the art in this field. Recent developments in the aerospace composites industry are starting to change this perception, especially regarding Carbon Fiber Reinforced Polymer (CFRP) application. Hence this study, which aims to propose an integral CFRP propellant tank concept and determine mass savings by comparing it to a metallic baseline, through finite element method (FEM) analysis with simulated flight loads. Tank dimensions, geometry and loads were chosen for micro-satellite SLV application. Also, Altair's Optistruct solver was used for FEM calculations, with Altair's HyperWorks for pre and post-processing. A mass reduction of close to 35% has been obtained with comparison to the metallic baseline design for the same boundary conditions. Therefore, a sound and competitive design for a micro-satellite SLV propellant tank has been successfully achieved.

1. INTRODUCTION

Propellant tanks account for more than half of the dry mass and close to 90% of the volume of a space launch vehicle (SLV) [1, 2]. This makes mass reduction in propellant tanks to have a major potential effect in the SLV's performance, as they are a centrepiece in its design. Composite materials, particularly carbon fiber reinforced polymers (CFRP), exhibit superior specific-strength and specific-stiffness than the currently used metallic alloys, even though they are possibly 30 to 40% lighter [3].

Propellant tanks are mostly cylindrically shaped to better use the space inside a missile-like vehicle, whilst holding the propellants under pressure. In vertical launch vehicles, they usually double as the main structure, becoming "load-bearing" or

"integral" propellant tanks [1, 2]. Moreover, because of the long cylindrical shapes, stiffness is as important as strength, to avoid buckling. Hence, they are expected to endure mostly axial compression and hoop stresses.

However, some of the properties of composite materials present challenges for their application in propellant tanks. First, there is always some rate of propellant diffusion with cryogenic propellants due to matrix porosity, but laminates that avoid micro-cracking and internal manufacturing imperfections have achieved acceptable diffusion rates [3]. Leakage can occur through the porosity of the matrix, damage by delamination and accumulation of micro-cracks between the matrix and fibres [3]. Micro-cracks can be caused by the different thermal expansion coefficients of the materials

during thermal cycles or by lighter impact damage. In addition, the chemical compatibility with oxygen is an issue, as organic materials can ignite in strong oxidising environments under certain conditions. Even though CFRPs often fail some of the standard flammability tests, work is being done to create modified flammability acceptance tests for propellant tank application [3, 4].

Several works have been conducted on the chemical stability of epoxies in pure oxygen environments [5, 6]. CFRPs typically have cryogenic strength performance close to room temperature [7]. Their upper service temperatures,

slightly above 100 degrees Celsius [8], are sufficient for launch vehicle application as they are now commonly used in solid propellant motor structural fuselages [2], with special care for thermal insulation.

The aim of this work is to develop an integral CFRP propellant tank concept and determine mass savings by comparing it to a metallic baseline, through finite element method (FEM) analysis with simulated flight loads.

2. LAUNCH VEHICLE AND TANK CONCEPTS

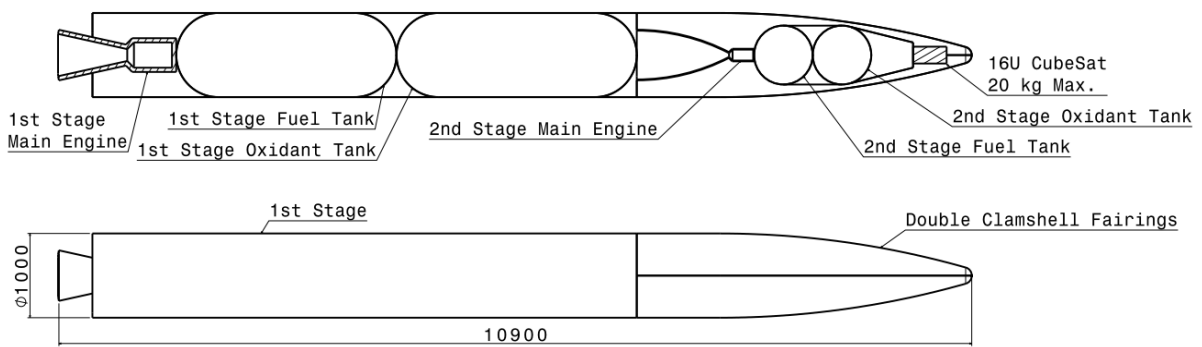


Figure 1. SLV Concept (section and exterior views; dimensions in millimetres).

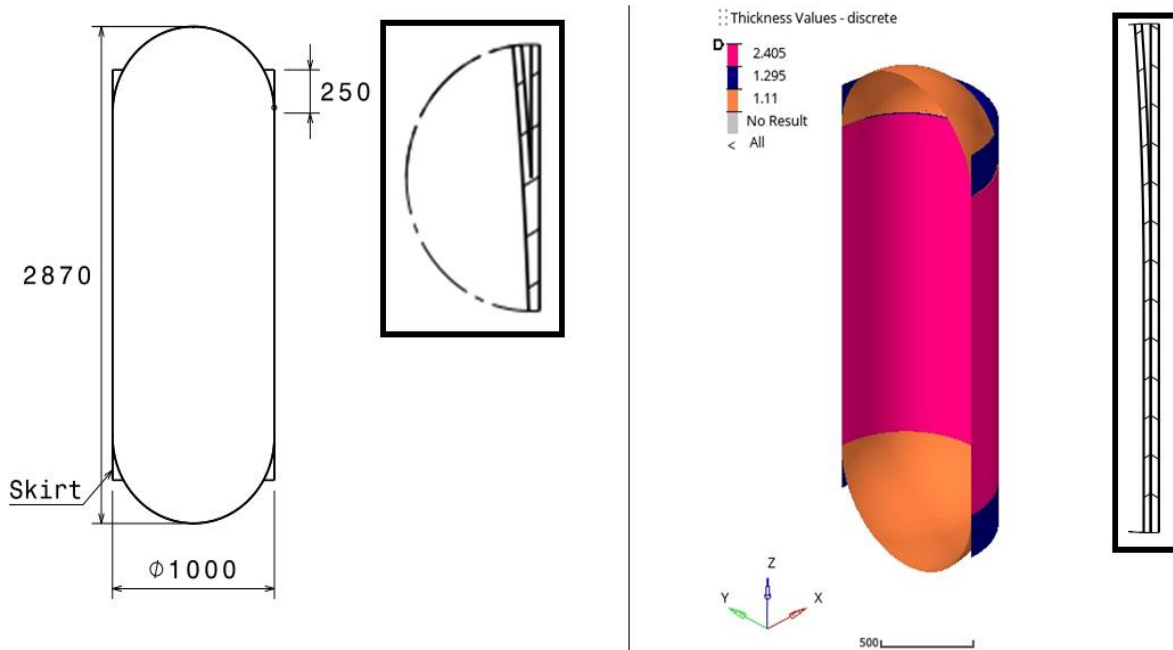


Figure 2. Aluminium (left) and composite (right) tank concepts with the respective skirt joint details.

The geometric and performance data of a space launch vehicle is required to calculate the flight loads to which the propellant tank will be subjected, wherefore a small SLV conceptual design was developed. Then, a metallic tank concept was designed for baseline comparison, followed by an equivalent CFRP propellant tank design. With the tank geometry defined, the respective FEM models were created and simulated to assess static strength and static stability behaviour taking into account safety factors used in launch vehicle design, as per Anon. (2016) [9].

Figure 1 shows the concept of the launch vehicle. As today's electronics allow for the construction of utilitarian microsatellites (10 to 100 kg) and nanosatellites (1 to 10 kg), this concept

was designed for the dedicated launch of small payloads of up to 20 kg to orbit. It is a 3,000 kg gross weight, two-stage, expendable SLV with composite construction and cryogenic propellants for their superior efficiency. The upper tank of the first stage is the one being analysed in this work.

The aluminium propellant tank baseline design is shown in Figure 2 (left side). Fabrication is assumed to be through forming and welding with a thickness of 1 mm. It is an integral tank, with the interface skirts to connecting to the rest of the vehicle, and spherical domes. The detail (Figure 2, left side) shows the transition zone between the tank itself and the skirts. Table 1 gives the chosen aluminium alloy mechanical properties. For the composite tank (Figure 2, right side), the overall

Table 1. Aluminium properties.

AL 2219-T87				
Tensile Yield Strength	Tensile Ultimate Strength	Density	Poisson's Ratio	Elastic Modulus
[MPa]	[MPa]	[kg.m ⁻³]	-	[MPa]
352	434	2,851	0.33	72,395

Table 2. CFRP properties.

AS4 Carbon Fiber Tow/Toughened Epoxy						
E1	E2	NU12	G12	G1Z	G2Z	Density
[MPa]	[MPa]	-	[MPa]	[MPa]	[MPa]	[kg.m ⁻³]
141,000	9,750	0.267	5,200	5,200	3,190	1,580
Xt	Xc	Yt	Yc	S	ILSS	Thickness
[MPa]	[MPa]	[MPa]	[MPa]	[MPa]	[MPa]	[mm]
2,200	1,500	81	260	80	128	0.185
E1 - Longitudinal Elastic Modulus E2 - Transverse Elastic Modulus NU12 - In-Plane Major Poisson Ratio G12 - Longitudinal In-Plane Shear Modulus G1Z - Longitudinal Out-of-Plane Shear Modulus G2Z - Transverse Shear Modulus Xt - Longitudinal Tension Strength Xc - Longitudinal Compression Strength Yt - Transverse Tension Strength Yc - Transverse Compression Strength S - In-Plane Shear Strength ILSS - Interlaminar Shear Strength						

dimensions are the same. No sandwich construction is used to avoid delamination caused by trapped gases due to permeation. Table 2 provides the mechanical properties of the selected carbon fiber tows with toughened epoxy matrix. The composite tank assumes filament wound manufacturing of an internal tank and external barrel. Both sub-components are then co-cured to form a single part. A detail of the transition zone can be seen in Figure 2, right side.

These are the ply orientations for both sub-components:

- [+30/+60/-30/90/+30/-60/-30] for the external barrel.

- [-45/+45]₃ for the internal tank.

3. FEM MODEL

After modelling the tank geometry, a FEM model of each tank was made. Bi-dimensional quadrilateral shell elements of the 1st order were used with an element size of 25 mm. Regarding the element size, a convergence study was made with element sizes of 20 mm and 15 mm, and the maximum von Mises stress varied about 0.3%, therefore, the 25 mm element size was maintained.

A one-dimensional rigid multi-point constraint (MPC) element is attached to the upper skirt edge and its function is to evenly distribute the flight resultant forces and moments, as can be seen in Figure 3.

As for boundary conditions, the lower skirt edge nodes have their displacement constrained in all 6 degrees-of-freedom (6DOF) with single point constraints (SPC).

Concerning the software used, the solver package was Altair's Optistruct, with Hyperworks for pre- and post-processing. The FEM models were subjected to linear static and static instability analysis to compare the tanks strength and rigidity when subjected to the flight loads. For the linear static analysis, Optistruct employs the BCS solver that is based on the stiffness matrix method. The von Mises distortion energy criterion was used to access the strength of the ductile isotropic metallic tank, while for the CFRP tank, with orthotropic laminates, the Hoffman Failure Index (FI) quadratic criterion was used, assuming First Ply Failure (FPF).

As to the static instability analysis, an Optistruct linear buckling solver was used that makes a real eigenvalue extraction using the Lanczos method.

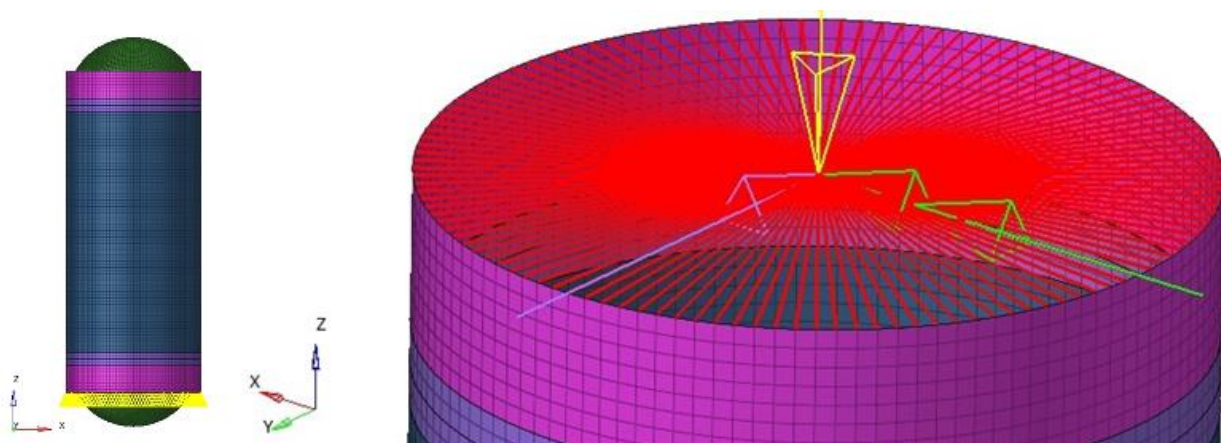


Figure 3. Propellant tank FEM model (left) and load application detail (right).

Table 3. Maximum tank loads.

Fz	Fy	Mx	MEOP	MSP
[N]	[N]	[N.m]	[MPa]	[MPa]
8,831	3,083	11,338	0.578	0.13

Table 4. Load case definition.

LC	Load Case Name	Axial	Shear	Moment	Inertial [g]	Internal Press.
1	MEOP Proof	-	-	-	1.0	MEOP
2	Max. Compression	-Fz	-Fy	Mx	3.0	MSP
3	Max. Tension	-Fz	-Fy	Mx	3.0	MEOP
4	Pressure failure	-Fz	-Fy	Mx	3.0	0

Table 5. Factors of Safety (FoS) by load case.

LC	Load Case Name	FoS Metallic		FoS Composite		Buckling Knockdown Factor (K)
		Yield	Ultimate	Continuous	Discontinuous	
1	MEOP Proof	1.05	-	1.05	N/A	0.65
2	Max. Compression	1.25*	1.4*	1.5*	2.0*	
3	Max. Tension	1.25	1.4	1.5	2.0	
4	Pressure failure	-	1.0	1.0	N/A	

Assuming no imperfections, the first positive eigenvalue provides the factor of the load at which the structure will buckle for the respective load case.

Table 3 contains the maximum resultant flight loads and internal pressures that were calculated for the launch vehicle shown previously. MEOP is the maximum expected operational pressure, including the hydrostatic pressure contribution of the contained propellant, while MSP is the defined minimum stabilizing pressure. Fz, Fy and Mx are the resultant maximum compression and shear forces and bending moment, respectively, and surmise all flight loads acting on the vehicle.

Table 4 has the load case definition, while Table 5 shows the safety factors (from Anon. (2016) [9]) included in the respective load cases. The first load case is to access the behaviour of the tank under maximum pressure and has no flight loads applied. The second load case accounts for the tank operating near the minimum pressure (close to depletion), where the maximum compressive stresses might appear. The pressure for this load case has no factor of safety to prevent increasing the stabilizing effect that the internal pressure has on the structure, and that may increase rigidity. This is noted as an asterisk in the load case safety

factors. On the other hand, the third load case has all loads at full strength with the appropriate factors of safety. Finally, the fourth load case has no internal pressure or factors of safety. This load case is to access the structural behaviour in case of a sudden critical pressure drop during the flight, like in the event of a rupture or valve malfunction. Regarding the factors of safety, they are different for metallic and composite materials. Metallic load cases also have separate factors for yield and ultimate tensions, and composite materials for zones with and without discontinuities. A buckling knockdown factor is applied to the eigenvalue factors to account for material and geometric imperfections.

4. RESULTS

After design and modelling iterations, the final mass for the aluminium tank was 30.18 kg and 19.65 kg for the CFRP tank. So, by changing the material from aluminium to CFRP, mass savings of close to 35% were achieved in spite of the increased thickness of the composite laminates. The strength and rigidity analysis results are surmised by Table 6 for the aluminium tank and Table 7 for the CFRP tank. It can be observed that

Table 6. Aluminium tank results.

Aluminium Tank					
LC	von Mises [MPa]	MoS -	Max. Disp. [mm]	Buckling Factor -	MoS (w/ K-factor) -
1	240.37	0.46	1.96	N/A	N/A
2(y)	108.14	2.26	2.60	2.93	0.90
3(y)	333.20	0.06	4.05	2.62	0.70
4	46.63	8.31	2.03	3.65	1.37
2(u)	114.32	2.80	2.90	N/A	N/A
3(u)	373.18	0.16	4.54	N/A	N/A

Table 7. CFRP tank results.

CFRP Tank				
LC	Hoffman FI -	Max. Disp. [mm]	Buckling Factor -	MoS (w/ K-factor) -
1	0.18	1.25	N/A	N/A
2	0.09	2.84	2.65	0.72
3	0.37	4.24	2.46	0.60
4	0.03	1.84	3.99	1.59
2(disc)	0.12	3.75	N/A	N/A
3(disc)	0.55	5.65	N/A	N/A

load case 3 is the critical one, having the highest stresses and the lowest bucking margin of safety.

The two bottom rows show the results with the greater factors of safety for the ultimate strength (aluminium, Table 6) and discontinuous zones (CFRP, Table 7).

In Figure 4 the two left side images (a and b) show the criterion results for both tanks for the third load case (LC03) with the greatest factors of safety. It can be seen that the aluminium tank is stressed close to the ultimate strength of the material (a) as this is the most critical load case. In the composite tank, only the zones with discontinuities are relevant for this factor of safety, and, therefore, are the only ones shown (b). This was the limit that led to a final increase in the composite interior tank

thickness during the design process, hence, the final composite design is lightly loaded.

The two right side images (c and d) show the criterion results for the fourth load case (LC04) for both tanks, were the internal relative pressure is zero. The bending and shear effects are clearly visible with one side of the tanks being more loaded. By comparing both load cases, it is noticeable that the internal pressure is the most critical load, as the other load cases have a similar stress distribution to LC03.

Lastly, Figure 5, to the left (a and b), shows LC03 criterion distribution, with the lower factors of safety for yield and continuous zones, while to the right (c and d) are the buckling failure modes for the same load case with the respective margins of

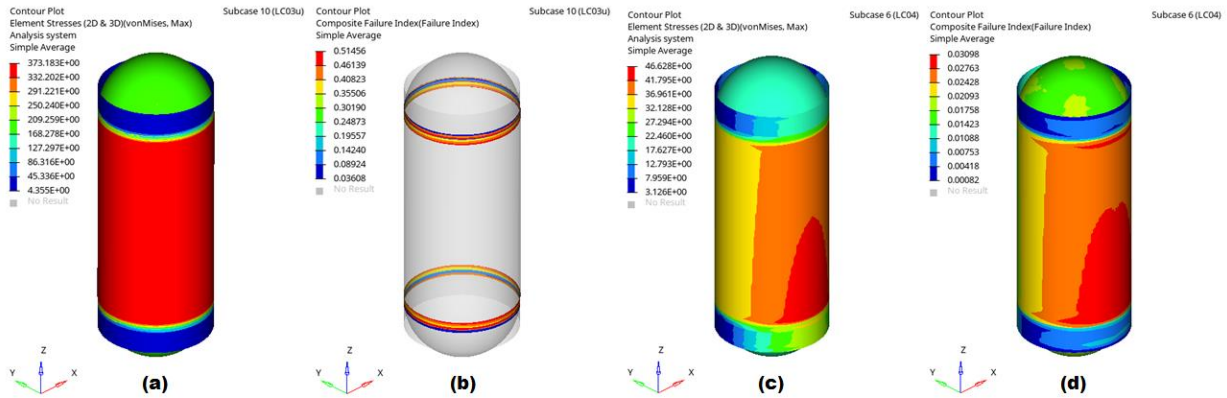


Figure 4. Results: (a) LC03 - Aluminium, von Mises Ultimate; (b) LC03 - Discontinuous CFRP, FI; (c) LC04 - Aluminium, von Mises; (d) LC04 - CFRP, FI.

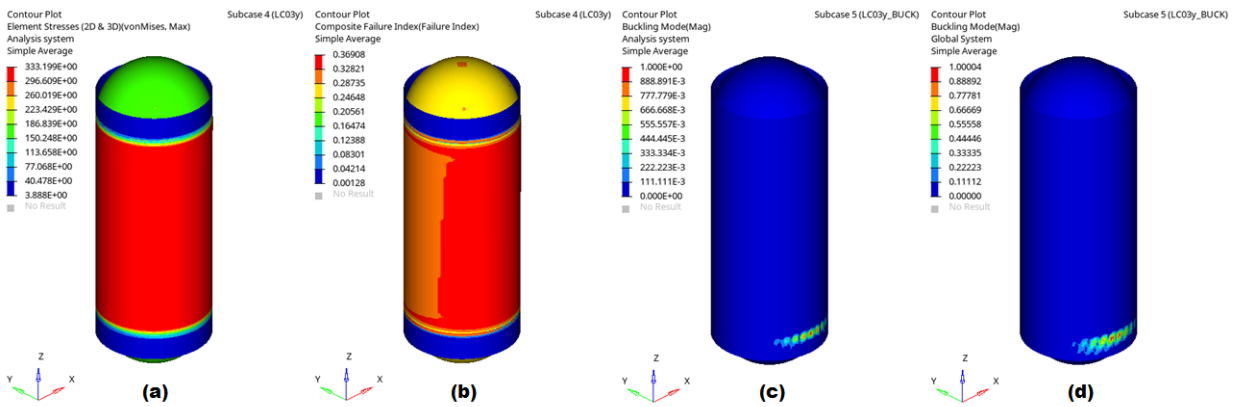


Figure 5. Results: (a) LC03 - Aluminium, von Mises Yield; (b) LC03 - Continuous CFRP, FI; (c) LC03 - Aluminium, Buckling, MoS 0.7; (d) LC03 - CFRP, Buckling, MoS 0.6.

safety. Buckling behaviour is similar in the other load cases and therefore not shown.

No positive eigenvalues could be found for the first load case. This should be due to the stabilizing effect of the internal pressure and no other significant loads being applied to the tank.

As it was previously noted, the composite tank concept is lightly loaded and sub-optimized owing to discreet ply increase as a function of fiber roving thickness. For the internal tank subpart, the ply number increase was done to decrease in-plane shear stress concentrations at the discontinuous zones in the worst load case. As to the external barrel subpart, the increase of plies was done to increase rigidity of the composite tank at the skirts for bulking knockdown factor

compliance. Also, the internal tank ply orientation is optimized for the spherical domes.

4. CONCLUSION

As can be seen, an equivalent CFRP composite propellant tank design has been achieved with 35% mass reduction. However, the final thickness of the composite tank is greater than its aluminium counterpart, even though no sandwich construction was used.

Also, this concept has potential for further mass reduction. For example, stiffeners can be applied to the barrel to increase rigidity and allow ply reduction.

We believe that small launch vehicles can benefit the most from composite components. This is because of the trend of the mass ratio of a launch vehicle becoming worse with the decrease in launch vehicle gross mass, leading to less structural efficiency in small launch vehicles.

ACKNOWLEDGEMENTS

The current study was funded in part by Fundação para a Ciência e Tecnologia (FCT), under project UID/EMS/00151/2013 C-MAST, with reference POCI-01-0145-FEDER-007718. Also, the authors would like to thank Altair for providing the HyperWorks FEM software package that made this study possible.

REFERENCES

- [1] D. H. Huang and D. K. Huzel, *Modern Engineering for Design of Liquid-Propellant Rocket Engines*, American Institute of Aeronautics and Astronautics, Washington DC (1992).
- [2] G. P. Sutton and O. Biblarz, *Rocket Propulsion Elements*, 9th ed., John Wiley & Sons, Inc., Hoboken, New Jersey (2016).
- [3] R. J. Wright, D. C. Achary, and M. C. Mcbain, in *Composite Development & Applications for RLV Tankage*, AIAA/ICAS International Air and Space Symposium and Exposition, Dayton, OH (2003).
- [4] D. A. McCarville et al., [*Compr. Comp. Mat. II*, **3**, 153 \(2018\)](#).
- [5] G. Wang et al., [*Mater. Sci. Eng. B Solid-State Mater. Adv. Technol.*, **132\(1-2\)**, 70–73 \(2006\)](#).
- [6] T. Sun et al., [*High Perform. Polym.*, **26\(3\)**, 319–325 \(2014\)](#).
- [7] R. P. Reed and M. Golda, [*Cryogenics \(Guildf.\)*, **34\(11\)**, 909–928 \(1994\)](#).
- [8] D. Cree et al., [*J. Compos. Constr.*, **19\(2\)**, 04014043 \(2015\)](#).
- [9] Anon., *NASA-STD-5001B W/ CHANGE 1 - Structural Design and Test Factors of Safety for Spaceflight Hardware*, Washington DC (2016).

Modeling of the 2D-materials hybrid nanostructures based on ferroelectric polymer PVDF/P(VDF-TrFE) and MoS₂ dichalcogenide

V. S. Bystrov^{1, *}, E.V. Paramonova¹, A.V. Saprionova^{1,2}, Hong Shen³, Xiangjian Meng³, Jianlu Wang³, L.A. Avakyan⁴

¹ *Institute of Mathematical Problems of Biology, Keldysh Institute of Applied Mathematics, RAS, 142290 Pushchino, Moscow region, Russia*

² *PetraOS AS, Straume, 5353, Norway*

³ *Shanghai Institute of Technical Physics, Chinese Academy of Sciences, Shanghai 200083, China*

⁴ *Southern Federal University, Department of Physics, 344090 Rostov-on-Don, Russia*

*Corresponding author, e-mail address: vsbys@mail.ru

Received 3 November 2020; accepted 10 December 2020; published online 15 December 2020

ABSTRACT

Transition metal dichalcogenide MoS₂ monolayers is very promising for many applications, especially in the fields of optics as emitters and detectors, in electronics as transistors. It is first of all due that they have a direct band gap E_g , which is dependent on external applied electric fields.

To create such an electric field, it is proposed to use the field induced polarization of ferroelectric polymers such as PVDF and P(VDF-TrFE). These polymers in the ferroelectric phase are capable to create significant polarization in very thin layers, about 5 Å. By combining such ferroelectric layers and MoS₂ layers, hybrid nanostructures can be created, that are convenient for design of new photodetectors with controlled properties. The prominent properties of this hybrid structure arise and benefit namely from the ferroelectric-polarization-induced ultra-high electric field of the PVDF or P(VDF-TrFE), that impact on MoS₂ layers and control the band gap E_g .

In this work, we simulate such a hybrid structure based on PVDF and MoS₂ layers and study their features and properties. For calculating MoS₂, the methods of density functional theory (DFT) are used, implemented in the VASP program. Semi-empirical methods based on the HyperChem software package are used to model and study both individual layers of the hybrid structure and the features of their joint interaction. The results obtained convincingly show a strong influence on the width of the MoS₂ bandgap E_g from the side of the PVDF layers, creating polarization P and an electric field E , which affects MoS₂ layers. In addition, the dependence of the band gap E_g under the action of electric field E from the distance between the layers PVDF and MoS₂ has been established.

1. INTRODUCTION

Transition metal dichalcogenides (TMD) constitute an important class of 2D materials: they have great potential for future applications as photodetector components due to their excellent optoelectronic performance [1, 2]. Bulk dichalcogenide materials have been studied for several decades, however, only recently new approaches to the creation and

study of nanoscale devices have opened up new possibilities for using monolayers with molybdenum disulfide (MoS₂), tungsten (WS₂), and other TMDs in nanoelectronics and optoelectronics. Layered molybdenum and tungsten dichalcogenides are semiconductors with a band gap of 1.3–2.1 eV, while bulk materials are indirect-gap semiconductors, but monolayers are direct-gap semiconductors [2, 3].

Naturally, such 2D materials have attracted much attention in the last decade for the manufacture of photodetectors [3 - 5]. Among them, the optoelectronic properties of the field-effect transistor, especially for the MoS₂ photodetector (sometimes called the phototransistor), have attracted the most intense attention of researchers.

Here, photodetectors and transistors based on, for example, 2D graphene [6, 7] and MoS₂, as well as their combinations, including those with other van der Waals structures [8], are promising.

On the other hand, the use of the properties of organic polymer ferroelectrics (FEP) [9-11], especially the discovery of two-dimensional ferroelectrics based on polymers (FEP) such as polyvinylidene fluoride (PVDF) and its copolymer with trifluoroethylene - polyvinylidene fluoride-trifluoroethylene P(VDF-TrFE) [12-22] turned out to be a significant breakthrough here, as it made it possible to create more and more efficient and at the same time nanoscale composite structures that have an ever wider range of adjustable properties, including pyroelectric, optical and piezoelectric properties) [9 - 22]. At the same time, composite nanostructures based on PVDF/ P(VDF-TrFE) in combination with Graphene/Graphene oxide [23-27]) are now being created and studied here. Note that in the study of such nanomaterials, computer methods for modeling structures and calculating the physical properties of these materials are also widely used [16-27].

As a result, interest in such new composite and hybrid nanomaterials with a two-dimensional structure (2D materials) has grown dramatically recently. Thus, in [4], it is proposed to use MoS₂ in combination with an organic polymer ferroelectric based on PVDF, which is safe and biocompatible. Such a photodetector [4], built on the basis of a hybrid quasi-autonomous FEP structure of the PVDF / P(VDF-TrFE) type in combination with MoS₂, already has more possibilities. The 2D MoS₂ ultrafine structure brings a great advantage for the heat dissipation of such a pyroelectric infrared detector. At the same time, the P(VDF-TrFE) polarization ferroelectric electric field significantly improves the photoconductive properties of MoS₂ and reduces the dark current and noise.

A further development of this approach is also work [5], which presents a version of the prototype photodetector with a broader spectral response, built on a quasi-autonomous hybrid structure of an organic FEP (P(VDF-TrFE)) and a two-dimensional semiconductor MoS₂. The two-dimensional 2D ultrafine structure of MoS₂ brings here a great heat dissipation advantage for such a pyroelectric infrared detector.

In addition, the electric field of ferroelectric polarization can not only restrain and reduce the dark current in the entire spectrum, but also change and narrow the band gap of MoS₂, thereby regulating the width of the optical absorption zone here, which significantly increases the photoconductive properties of MoS₂. The most impressive characteristic of this type of detector is that these mechanisms are synergistic [5].

In the present work, the main attention is focused to the study of the structural and physical properties, the interaction of FEP of the PVDF and P(VDF-TrFE) types with two-dimensional 2D structures of dichalcogenides of the MoS₂ type - using the methods of computer molecular modelling and calculations by different methods. These numerical and computer studies in this work are carried out on the basis of the developed and already well-tested approaches on other materials (PVDF, Graphene, Hydroxyapatite) using the density functional theory (DFT) [28-31] and quantum-chemical semi-empirical methods (such as PM3, ZINDO/1, etc.) [16-27, 49]. Theoretical studies and calculations of the properties of a number of TMD have already been carried out by various methods [32-36], and we use these results for comparison with data obtained in our calculations. In this work, we consider not only the TMD and FEP themselves, but also the models and properties of hybrid nanostructures based on them, for example, such as "PVDF + MoS₂" [31].

In the future, a similar simulation and study of nanomaterials and heterostructures for photodetectors based on MoTe₂ [37], MoSe₂ [38], MoSe₂-Cr [1, 39] and other dichalcogenides of transition metals and related ferroelectric nanostructures will be carried out.

2. COMPUTATIONAL METHODS AND DETAILS

The calculations were carried out using the first principles DFT methods, implemented in Vienna Ab Initio Simulation Package (VASP) [40–43]. The generalized gradient approximation (GGA) with the exchange-correlation potential was evaluated using the Perdew, Burke, and Ernzerhof (PBE) functional [43,44]. Core states were described by means of the projector augmented wave (PAW) method [45]. The values of the Kohn-Sham energies of the ground states of systems were calculated using plane waves with kinetic energy up to $E_{\text{cut}} = 400$ eV to expand the wave functions with fairly satisfactory convergence.

The primitive cell of single-layer MoS_2 containing one Mo atom and two S atoms was used under periodic boundary conditions. A vacuum space of 19 Å adopted along z-axis was used to be able to decouple possible periodic interactions. The valence electrons $s2p4$ for S and $4p5s4d$ for Mo were included in the PAW pseudopotentials.

For single layer MoS_2 calculation (with a direct band gap) GGA-PBE method was used taking into consideration of the van der Waals (vdW) interactions based on the method for VdW correction developed by Grimme S., Antony J., Ehrlich S., and Krieg S. [46] and named D3. This method is compatible with PBE and is implemented in VASP (as “PBE + D3”).

For the self-consistent calculations the Brillouin zone (BZ) was sampled by 11 x 11 x 1 Gamma-centred k-point grid obtained with Monkhorst-Pack scheme [47]. The band structure was evaluated on a path with k-spacing 0.05 \AA^{-1} . The real-space grid of 20 x 20 x 128 points was chosen to keep approximately constant spacing proportional to the length of a_1 , a_2 , and a_3 lattice vectors. The experimental data [4, 35, 48] provides the lattice constants $a_1 = a_2 = a = b \sim 3.19 \text{ \AA}$ of the known crystal structures MoS_2 and with $a_3 = c = \sim 19.0 \text{ \AA}$, which corresponds to the vacuum length between two adjacent layers in the supercell. The relevant grid density appears to be about ~ 6 points/Å along all the three directions.

To obtain the values of the energy, dipole moment, and polarization of the various MoS_2 and PVDF cluster structures the HyperChem package [49] was used with various quantum-mechanical

semi-empirical methods. The method PM3 (Parametrization No. 3, developed by Stewart J.J.P. [50-52]) in the restricted Hartree-Fock (RHF) approximation was mainly used. This PM3 method is based on the AM1 method (Austin Model 1, developed by Dewar M.J.S., et al. [53]). However, in this our work another method named as ZINDO/1 [54] is used widely. This method ZINDO/1 is based on a modified version of the intermediate neglect of differential overlap (INDO) [55], which was developed by Michael Zerner [54] is most suitable for **transition metals**. An intermediate neglect of differential overlap (INDO, ZINDO/1 scheme retains some of the one-center terms of the overlapped integrals and the neglect of diatomic differential overlap (NDDO) [52] schemes used in these approaches keep all of the one-center terms. Zerner's original INDO/1 used the Slater orbital exponents with a distance dependence for the first row transition metals only. However, in HyperChem [49] constant orbital exponents are used for all the available elements too, as recommended by Anderson, Edwards, and Zerner [54].

The main part of all quantum-chemical calculations in HyperChem was made using Single Point (SP) calculation method, which allow to obtain all necessary molecular electronic orbitals energy data values, such as, energy of the highest occupied molecular orbital (HOMO) and the lowest unoccupied molecular orbital (LUMO). Difference of these energies determine the forbidden band gap $E_g = E_{\text{LUMO}} - E_{\text{HOMO}}$. For some cases, when is necessary to taken into account the changes of geometry of the molecular systems, the optimization of molecular systems and finding of their optimal geometry is performed in this work using the Polak–Ribere (conjugate gradient method) algorithm, included in HyperChem package [49]. This approach is a especially important for the case of the dipole momentum rotation switching (and polarization switching) in the applied electric field at the critical point of the systems, such as, phase transition and reversal point of the hysteresis loop of the ferroelectric polar system. Simulation of the system under an imitated applied constant electric field is available in HyperChem packages too [49].

3. RESULTS AND DISCUSSION

Results of calculations performed using VASP [40-43] are shown on Fig. 1., where is presented the structure of the single monolayer MoS₂ with several unit cells (top and side views – Fig. 1 a, b). The lattice constant from self-consistent GGA-PBE calculations ($a = 3.18999 \text{ \AA} \sim 3.19 \text{ \AA}$) is close to the experimental data [33, 48] and theoretical value of other authors [32, 35, 56].

The electronic band structure obtained for single-layer MoS₂ with $E_g = 1.632 \text{ eV}$, is presented on Fig. 1 c. It was intensively investigated recently by both experiments and theory [2-5, 32-39, 56]. The data obtained by different authors varies in some wide range.

A direct band gap, for example, of about 1.75 eV was obtained from the measurements [2]. The dispersion of bandgap in the range of 1.75 -1.90 eV in experiments may be come from the different

preparation and measurement methods. Emilio Scalise [56] reported a value of 1.72 eV from GGA-PBE method calculation. The theoretical findings on direct bandgap calculations disperse also from 1.63 eV up to 2.76 eV. (depending on the exchange and correlation functionals used) [35]. Otherwise, C. Ataca [36] calculated a direct band gap of about 1.63 eV by GGA-PBE method taking into consideration of the van der Waals corrections (vdW) [46], and 1.87 eV by linear density approximation (LDA) method. As it can be seen, the LDA data turn out to be somewhat overestimated, while taking into account van der Waals interactions seems to give more realistic results. Data recently obtained by Wang et al. (published in Supplementary Materials section to [4]) shown very close similar data with $E_g = 1.63 \text{ eV}$ (Fig. 2 a).

It is worth to mention that the width of the band gap E_g significantly depends here on the applied

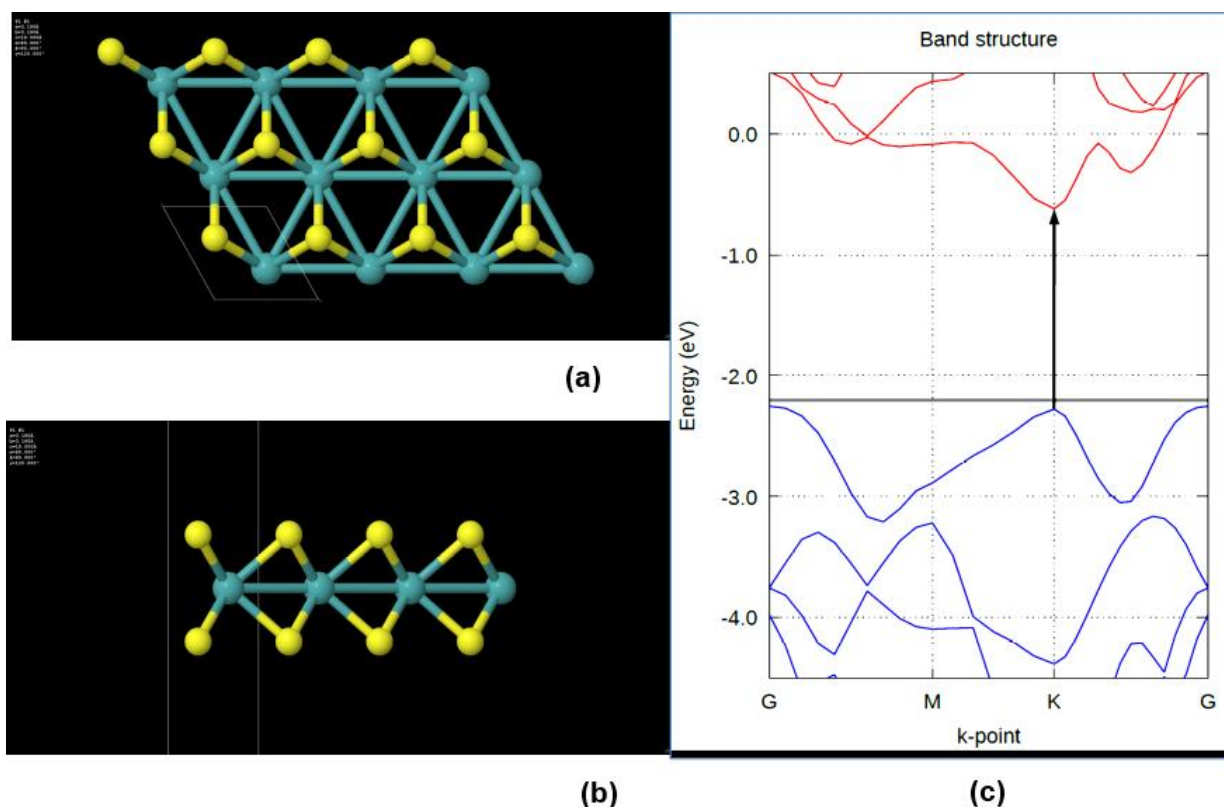


Figure 1. The structure of single-layer MoS₂ (obtained using Jmol after VASP calculations): a) top view, b) side view; and c) the computed electronic band structure of MoS₂ single monolayer with direct band gap transition along k-point variation with direct transition localization at K with computed energy value $E_g = 1.632 \text{ eV}$.

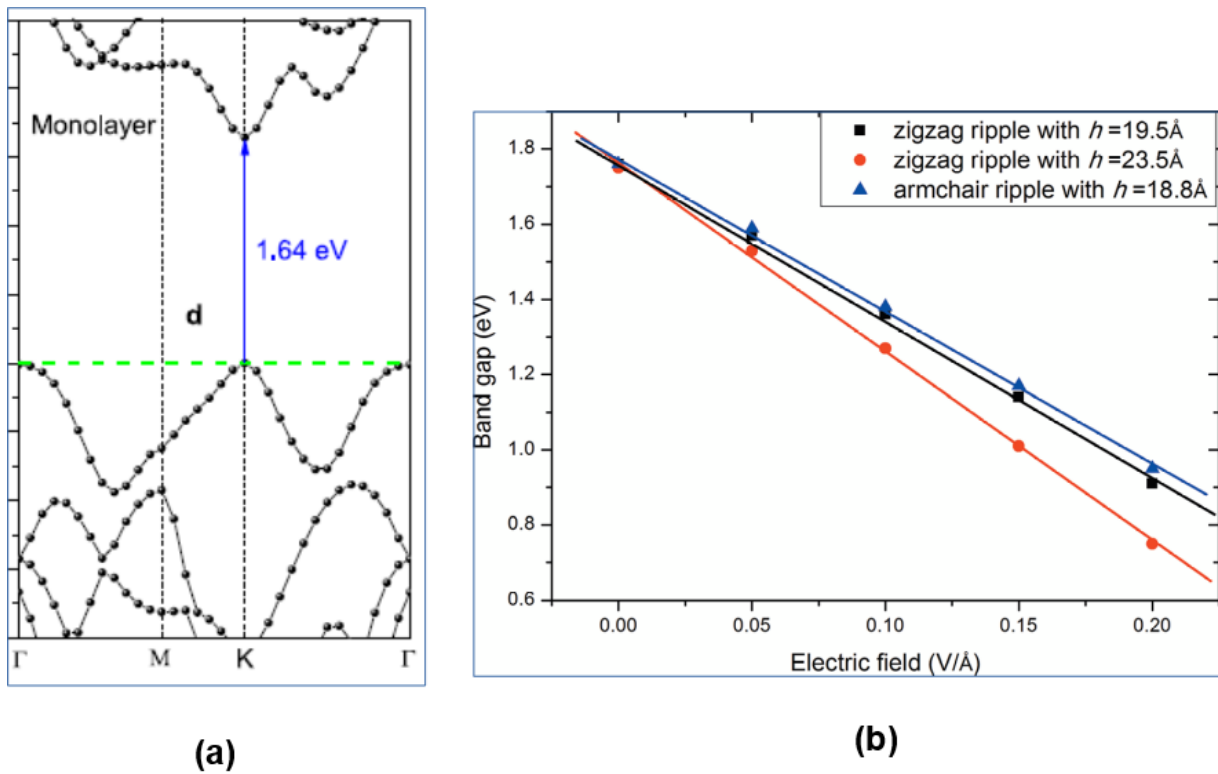


Figure 2. The band gap computed by DFT method [4] (a) and dependence $E_g(E)$ from [35] (b).

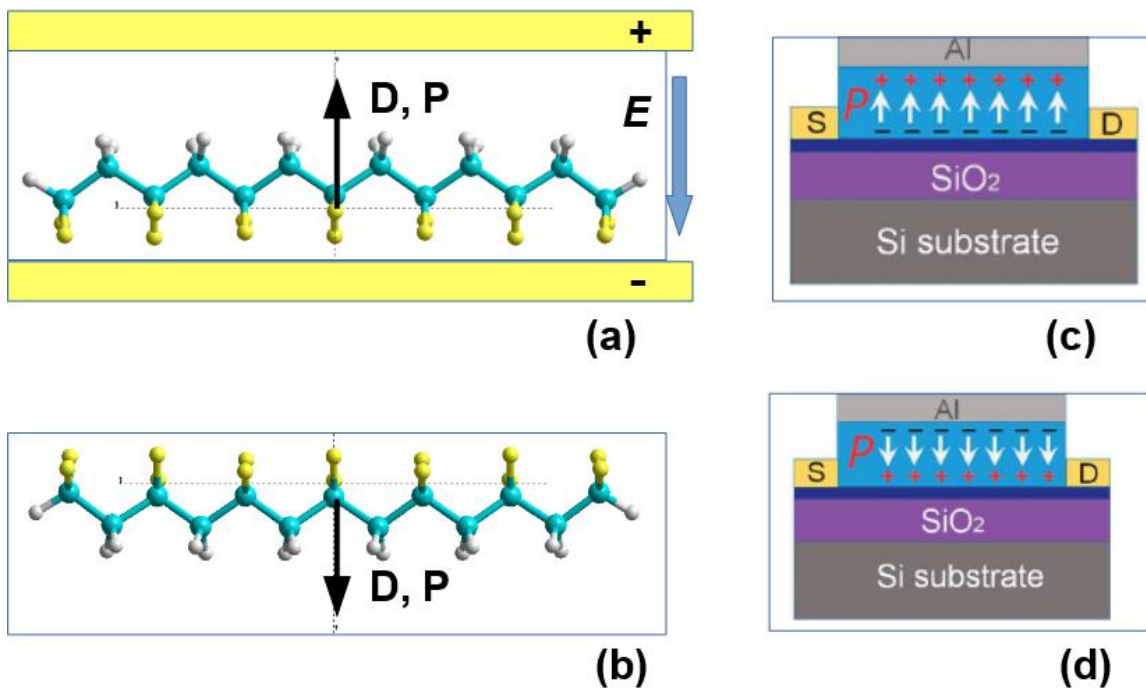


Figure 3. The PVDF single layer model structure under applied electric field E : a) direct position, b) switched on the opposite orientation position, c) and d) show the similar design of experimental units from Wang et al. work [4]. (D and P are the dipole moment and polarization of the PVDF chain of single layer, consequently).

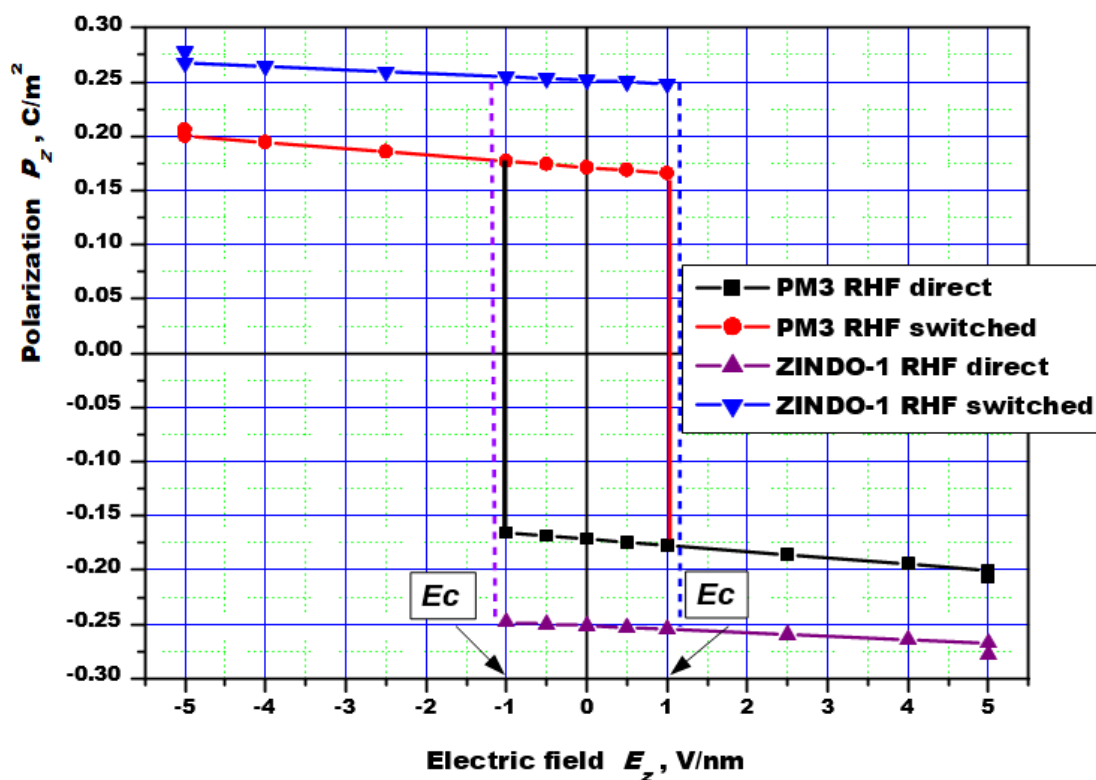


Figure 4. Hysteresis loop of the polarization depending on electric field $P(E)$, computed by both PM3 and ZINDO/1 methods in RHF approximation using HyperChem package [49].

both experimentally and theoretically [2-5, 34-39]. Moreover, this dependence is different (as well as the value of E_g itself at an electric field $E = 0$) for different multi-layered MoS₂ structures (besides single mono-layer, were studied bilayer MoS₂ [32, 33], triple-layers MoS₂ [4]). But here we are primarily interested in the single MoS₂ structure with direct bandgap.

In particular, a similar structure was recently investigated and calculated in [35] and this dependence is shown in Fig 2 b. Typical values of the applied electric field E in the range of 0.0–0.001...0.2 V/Å = 0.0 — 0.01...2 V/nm lead to a change in E_g from 1.7 eV to 1.0 - 0.6 eV. The band gap E_g value as a function of electric field is displayed in Figure 2b for single MoS₂ layer structure (from work [35]). Despite the ripple character of studied MoS₂, it is clearly shown that E_g is linear dependent on electric field for any case. The similar linear relationship of E_g with rise of the electric field was reported also in the other

transition-metal dichalcogenide, such as, bilayers under external electric field [33].

Among other things, it turned out that this range of variation of $E_g \sim 1.8 - 0.6$ eV is very important for optical measurements. From experimental studies and the bandgap calculations, it can be seen that the single-layer MoS₂ seems to be active for visible light absorption spectrum. For example, the peaks of the imaginary dielectric constant (which is usually used for measures the light absorption ability of materials) lie among the visible light range (350 nm – 700 nm, or 0.34 eV – 1.77 eV) for single-layer MoS₂. Since it would display high absorption of the sunlight and could be ideal for various photocatalysts applications, etc.

Another important point here was the search for the most suitable tools for controlling and regulating the change in the width of E_g in the MoS₂ layers of the vehicle, including, by influencing on MoS₂ samples by an electric field. The problem and the important task here was to find such a method

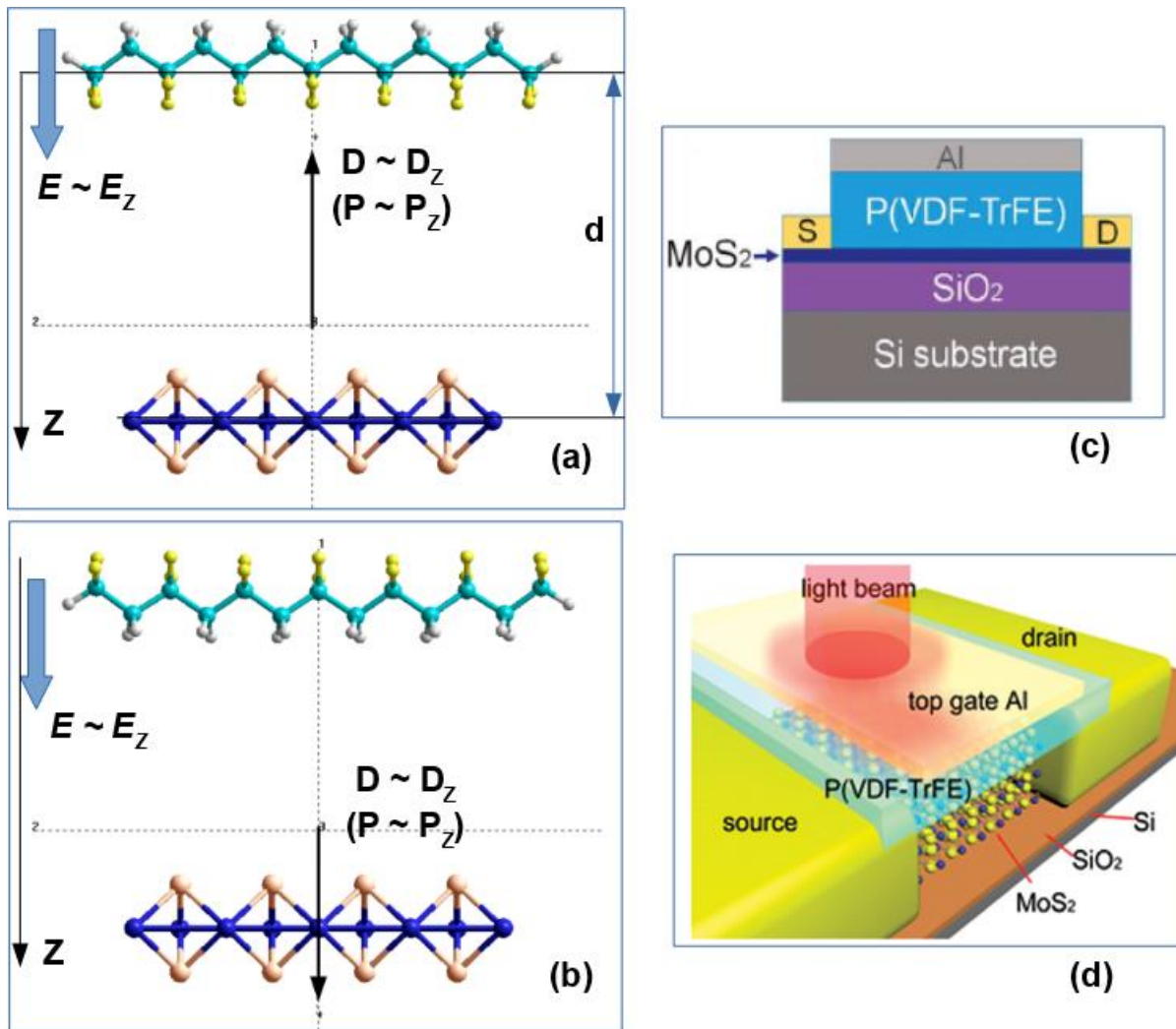


Figure 5. The MoS₂ single monolayer model interacting with PVDF layer (“PVDF + MoS₂” model): a) with direct PVDF orientation of the polarization vector P and with atoms F directed to atoms S, b) with switched PVDF on the opposite orientation of the polarization vector P and with atoms H directed to atoms S of MoS₂, c) and d) present the corresponding samples design of the hybrid structure configuration, which was used in Wang et al. work [4].

and means that would allow us the manipulation at the nanoscale, at sufficiently small micro-sizes, to create the appropriate technology, nano-devices and equipment.

It turned out that for this purpose, embedded layers of such a ferroelectric polymer films as PVDF and its copolymers P (PVDF-TrFE) can be very convenient. These materials are capable of creating and maintaining their spontaneous ferroelectric polarization just at the nanoscale sizes. And the electric field created by their polarization is capable of penetrating into the MoS₂ layers and affecting its E_g .

This idea was realized by Wang et al., for example, in their work [4].

It should be taken into account that the value of the PVDF polarization itself also depends on the electric field, which can be applied to layers of PVDF sandwiched between two electrodes. Thus, it is possible to easily change and render both the magnitude of this polarization and the width of the bandgap E_g in MoS₂ layers at the nano level.

The magnitude and direction of polarization P of this polymer ferroelectric is easily controlled by applying an electric field to the PVDF layers. It is also important here that on the basis of this polymer ferroelectric it is possible to create ultrathin layers up to one monolayer with a thickness of $d \sim 0.5$ nm, which nevertheless has a highly ordered polar structure. Practically important polymer

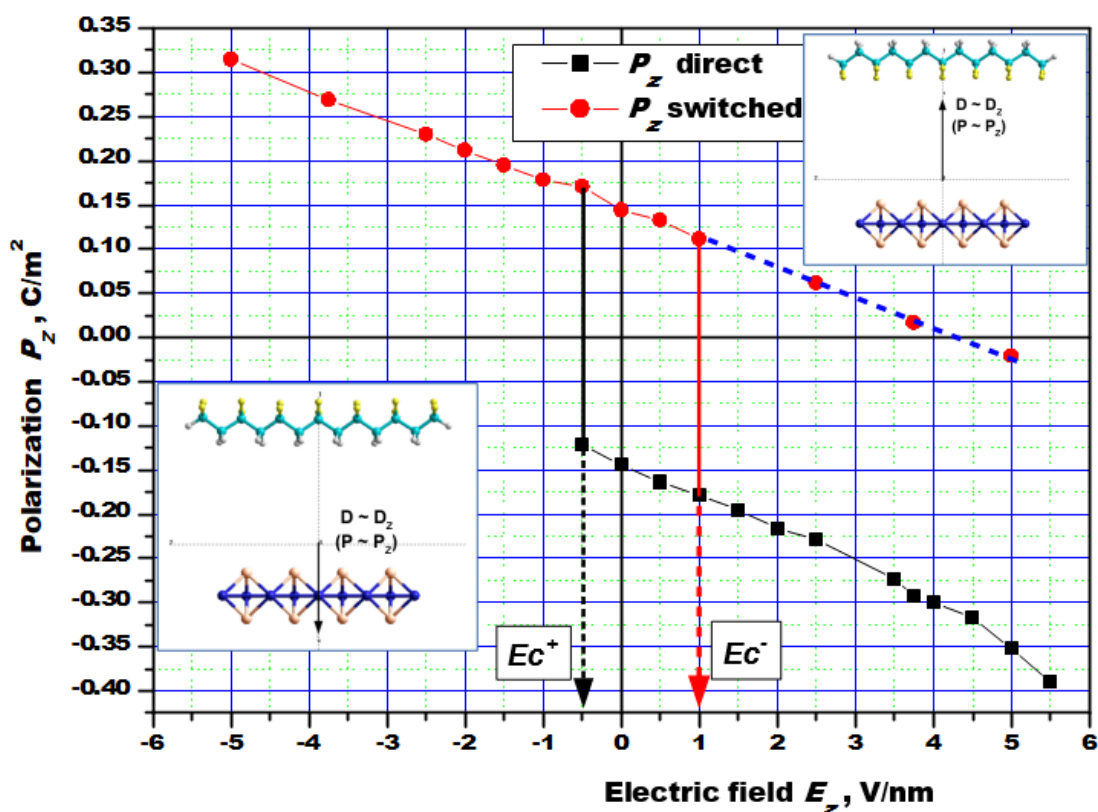


Figure 6. Computed dependence $P(E)$ for the hybrid “MoS₂+PVDF” model with hysteresis loop behaviour, having the asymmetric $P(E)$ branches and various coercive field E_c^+ and E_c^- .

structures of various thicknesses, including copolymers based on PVDF with tri-fluoroethylene (P (VDF-TrFE), can be easily removed either by ultracentrifugation methods (spun or spin coating films, with thickness ~ 100 -300 nm) or by Langmuir-Blodgett (LB) technique (for ultra-thin films 0.5 - 100 nm). And these films are now quite well studied, including by the methods of molecular modeling [12-22].

In this work, we consider such a hybrid structure of «PVDF + MoS₂» - using the approaches of computer molecular modeling methods. First of all, we will consider and evaluate PVDF itself their main characteristic features and properties that allow them to be applied as a control factor on the E_g inside MoS₂ structure. This first model of the PVDF single layer and its behaviour in electric field E is shown in Fig. 3.

It is important that the polarization P and the field created by P outside the PVDF layers also

depend on the electric field applied to the PVDF layers. Changing the magnitude and direction of the applied field E changes the magnitude of polarization P and switches the direction of polarization and, accordingly, changes the magnitude of the electric field induced in the MoS₂ layers.

We here simulate these properties, calculate and investigate the methods of semi-empirical calculations in the HyperChem software package. Here we have enough experience of such calculations [16-27]. The example of the main results and features for such simple PVDF chain (layer), computed by two semi-empirical quantum-chemical methods, is presented on Fig. 4. The main peculiarity of PVDF behaviour in applied electric field is following: 1) proportional rise of the polarization in the direct electric field, 2) switching on the opposite orientation of the polarization

Table 1. Computed data for both PM3 and ZINDO/1 methods at the distance d between two components of the “MoS₂+PVDF” model: $d=10$ Å, RHF approximation, both MoS₂ and PVDF, total calculating volume of the system $V= 469.96$ Å³.

E_z , V/nm	D_z , Debye	$ P_z $, C/m ²	$ E_z^* $ = $=P_z/(2\epsilon\epsilon_0)$, V/nm	E HOMO, eV	E LUMO, eV	E_g , eV
ZINDO/1						
-1.0	-15.2632	0.1083	1.22	-6.235692	-1.790490	4.445202
-0.5	-19.0451	0.1352	1.53	-6.295287	-1.889087	4.406200
0.0	-20.4119	0.1449	1.64	-6.065749	-1.996101	4.069648
0.25	-21.7524	0.1544	1.74	-6.324941	-1.654380	4.670561
0.5	-21.9214	0.1556	1.76	-6.231306	-1.912776	4.328530
1.0	-25.7201	0.1825	2.06	-6.305033	-1.865325	4.439708
2.5	-32.1791	0.2284	2.58	-6.09897	-1.981790	4.117167
4.0	-39.1240	0.2777	3.14	-5.116526	-1.968208	3.148328
5.0	-43.8091	0.3109	3.51	-4.040537	-2.051025	1.989512
PM3						
-1.0	-	-	-	-	-	-
-0.5	-13.4113	0.0952	1.075	-9.569354	-3.372284	6.197070
0.0	-14.3315	0.1017	1.15	-9.563627	-3.360310	6.203317
0.25	-14.8299	0.1053	1.19	-9.422036	-3.280216	6.141820
0.5	-15.2687	0.1084	1.22	-9.533896	-3.335629	6.198267
1.0	-16.0992	0.1143	1.29	-9.451263	-3.760474	5.690789
2.5	-19.0066	0.1349	1.59	-9.530275	-3.347384	6.182891
4.0	-21.8701	0.1547	1.75	-8.486326	-3.464778	5.021548
5.0	-23.6958	0.1677	1.89	-7.425726	-3.320158	4.105568

vector P under influence of the electric field E , when E reached its critical coercive values E_c .

The simplest model of the more complex hybrid structure, consisting of PVDF and MoS₂ single layer, is shown in Fig. 5. This model we also investigate by various methods from HyperChem package software [49]. Note that here besides PM3 here we wide use the ZINDO/1 method, available for transition metals. In any case we compare the data obtained by both methods for the case of the distance between PVDF and MoS₂ layer $d = 10$ Å (see below in Table 1).

The dependence $P(E)$ have hysteresis loop character with switching points at the $E = \pm E_c$ (Fig. 4).

For hybrid model “MoS₂ + PVDF” (Fig. 5) this behaviour have the similar character, but transforming to the more complex dependence with two asymmetric branches of the polarization P

behaviour (up and down zero field E) and having two different coercive field E_c^+ and E_c^- (Fig. 6).

For comparison computed data of both used semi-empirical RHF methods (PM3 and ZINDO/1), the calculations performed at the distance $d = 10$ Å (between PVDF and MoS₂ components) were presented in the Table 1.

In HyperChem software after self-consistent calculations of the molecular structures by any quantum-chemical semi-empirical methods (as well by *ab initio* and DFT methods, included into HyperChem package) the data resulted and obtained have following main magnitudes (and its values in corresponding units): 1) dipole moment (in Debye unit), 2) total energy (in a. u. or can be converted to other units too), 3) energy of the highest occupied molecular orbital (HOMO in eV units) and energy of the lowest unoccupied molecular orbital (LUMO, eV), etc. We can

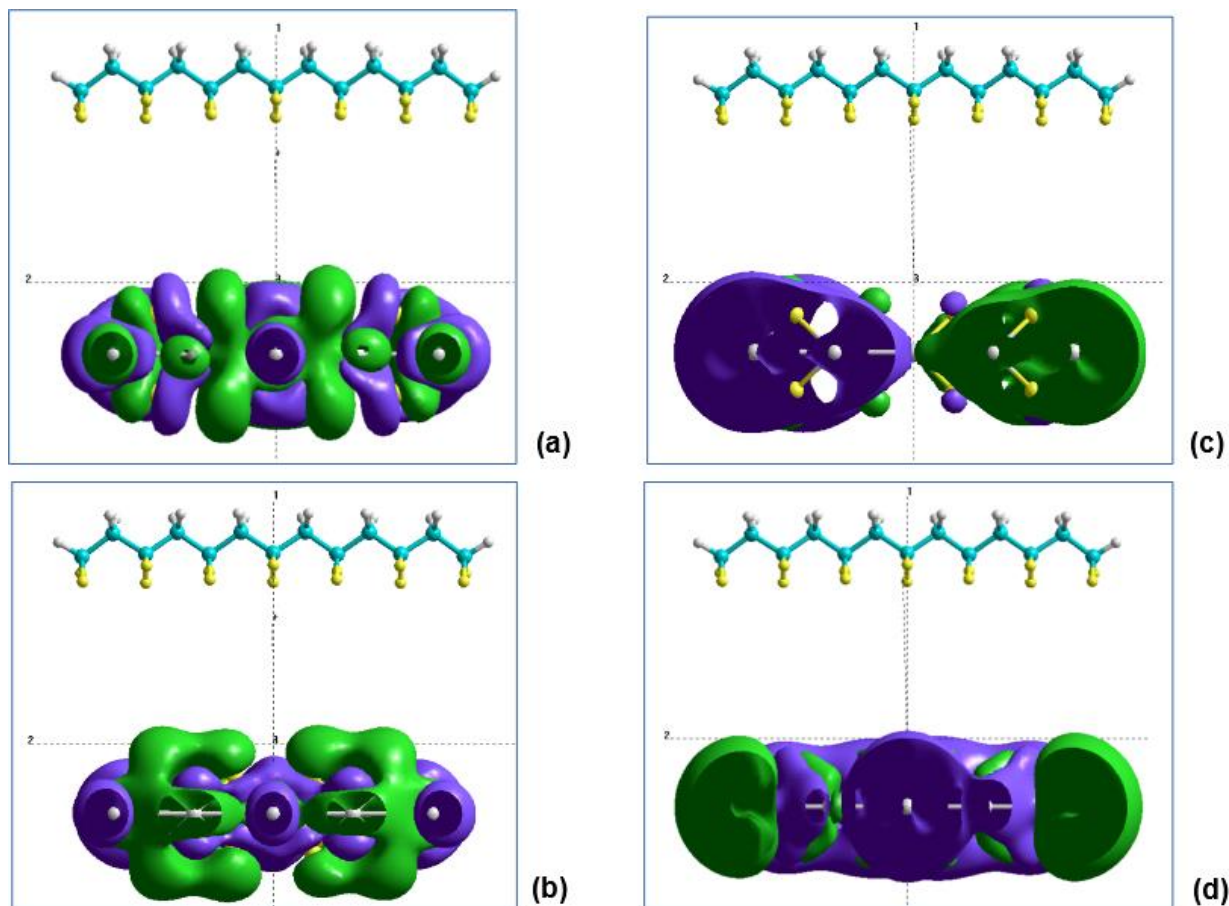


Figure 7. Electronic molecular orbitals for main energy states of the hybrid “MoS₂+PVDF” model and using the different semi-empirical computing methods:

- a) LUMO and b) HOMO computed by PM3 in RHF approximation;
 c) LUMO and d) HOMO computed by ZINDO/1 in RHF approximation.

calculate also the volume V , using special program. The band gap $E_g = E_{\text{LUMO}} - E_{\text{HOMO}}$. These data are presented in Table 1.

As usual, the value of the polarization P is obtained from dipole moment D (in Debye units):

$$P = 3.33558255 \cdot D / V \text{ (in } C/m^2\text{)},$$

where V is structure's volume on the Van der Waals surface.

Here we should note that, the prominent properties of this hybrid structure arise and benefit from the ferroelectric-polarization-induced ultra-high electric field of the PVDF (or P(VDF-TrFE) as in real usual samples).

To determine and estimate the magnitude of this local electric field E_z^* at the interface between PVDF and MoS₂ layers, which is created inside the MoS₂ layer from PVDF polarization P , we use the

expression $E_z^* = P_z / (2\epsilon\epsilon_0)$. Here ϵ is the dielectric constant (permittivity) of the material (for MoS₂ it is $\epsilon = 4 - 6$ [57, 58], ϵ_0 is the vacuum constant ($\epsilon_0 = 8.85 \cdot 10^{-12} \text{ C}/(\text{V}\cdot\text{m})$). For our estimation in this our work, and presented in Table 1 as an example for the calculations at $d = 10 \text{ \AA}$ (as well for other estimations), we use the middle value $\epsilon = 5$.

As results, we obtained data for $E_z^* \sim 1\text{-}2 \text{ V/nm}$ for PM3 calculations and more high values $E_z^* \sim 1.2 - 3.5 \text{ V/nm}$ for ZINDO/1 at the interface distance $d = 10 \text{ \AA}$ (see in Table 1). These data are some higher than estimations in [4] about of 0.5 V/nm . But, in [4] was used the experimental data for polarization estimation as remnant polarization $\sim 7 \text{ mC}\cdot\text{cm}^{-2} = 0.07 \text{ C/m}^2 \sim 0.1 \text{ C/m}^2$, which is less from our estimation. But, we must mentioned, that we consider an ideal and simplified PVDF model, while the experimental value of remnant polarization for P(VDF-TrFE) is some less then

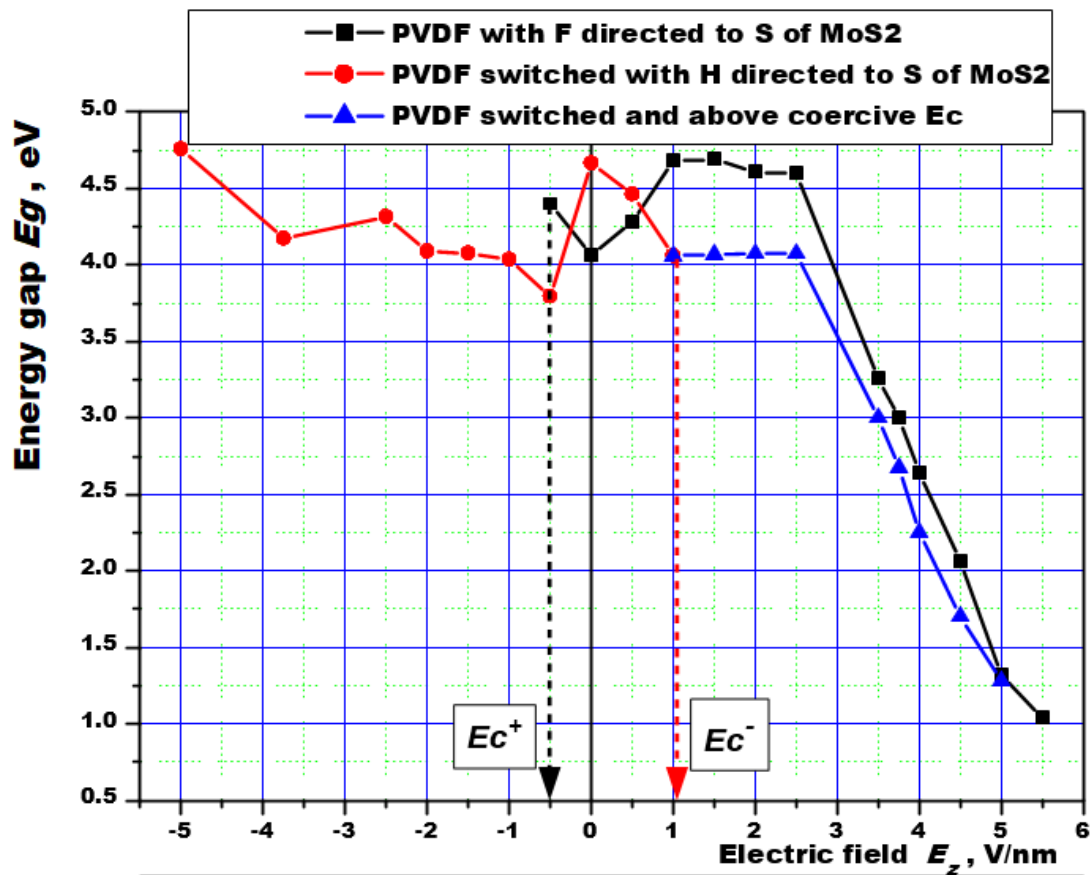


Figure 8. Computed energy band gap $E_g(E)$ for hybrid model “MoS₂ + PVDF” (Fig. 5 a) from the applied electric field E . This data is computed for distance d between MoS₂ and PVDF components $d = 10 \text{ \AA}$ as one of example of this hybrid system.

computed one. Therefore, these estimates can be considered as quite close.

The more detailed computed data of the $P(E)$ for this case are presented on the Fig. 6. These data shown two various branches of $P(E)$ with different asymmetric coercive field. This asymmetry occurs because the MoS₂ layers is located only from one side of the PVDF layers (see on Fig. 5). As a result, we obtain the similar hysteresis behaviour of the $P(E)$ for the hybrid model system (Fig 6) as for alone PVDF (Fig. 4), but it is shifted and having some different asymmetric shape of this hysteresis loop.

It means also that the additionally applied electric field E to the PVDF layers (using electrodes shown on Fig. 3) influences then trough risen polarization $P(E)$ directly on the MoS₂ layer, which

is positioned at the some distance d from PVDF place (Fig 5).

Further interesting and very important characteristic features is that the electronic molecular orbitals HOMO and LUMO are localized precisely on the MoS₂ layer positions remote at a distance d from the PVDF layer, as are shown in Fig. 7 (where are presented HOMO and LUMO computed using both PM3 and ZINDO/1 methods). Therefore, it is clearly show that the ferroelectric-polarization-induced ultra-high electric field of the PVDF (or P(VDF-TrFE) impact directly on the MoS₂ layer structure and influence on the $E_g = E \text{ LUMO} - E \text{ HOMO}$.

The next most important feature of this hybrid model system “PVDF + MoS₂” is that the dependence of band gap $E_g(E)$ clearly exists only

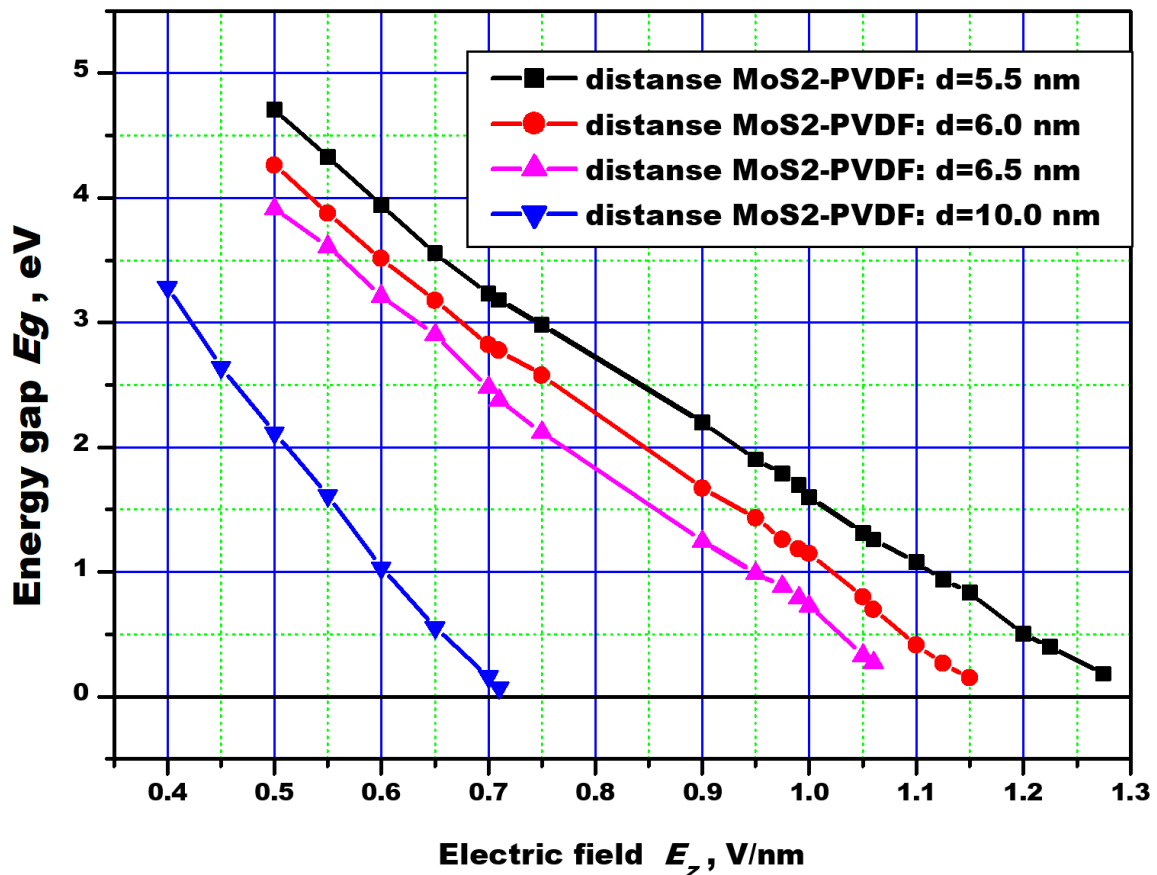


Figure 9. Computed dependence of the $E_g(E)$ for different distances d - between MoS₂ and PVDF components of the hybrid model system.

for electric field $E > 0$ (shown in Fig. 8), while for the $E < 0$ we obtain only fluctuations around the average E_g value, close to the value existing without electric field. (see in Fig. 8 left side at the $E < 0$).

The specific feature of the $E_g(E)$ behaviour is again asymmetric dependence of the band gap E_g from electric field E and existence of two different coercive field E_c^+ and E_c^- , which limited the region of the existence of the electric field from PVDF layer impact on the MoS₂ layer.

The most characteristic feature here is that namely only at $E > 0$ there is a pronounced dependence of E_g from the electric field E (Fig. 8).

Another important founded and observed (possibly obvious) factor is the dependence on the distance between the PVDF and MoS₂ layers (Fig. 9). The calculations performed using ZINDO/1 method show that this dependence have the similar close to linear behaviour $E_g(E)$ (see details in Fig. 9) as it was founded for several different MoS₂ structures by various authors [4-6,32-35, 56].

The very important feature is that this behaviour depends also from the distance d - between MoS₂ and PVDF. It is characteristic that this behaviour $E_g(E)$ has a similar, close to linear type of behaviour at different distances d between both components of the hybrid structures. But at the same time, with an increase in this distance d , the slope of the dependence becomes steeper and it shifts along the E axis.

It is the results obtained here for very simple theoretical molecular models and they describe approximative results of its features and behaviours. But these data obtained show the main principal features of the E_g behaviour from electric field E and intermediate distance d between both nanostructures MoS₂ and PVDF, which would be very important for further practical design of the device unit of the created photodetector samples.

The results obtained are, of course, somewhat different from the most precise DFT calculations.

But they are qualitatively very similar and reflect the main characteristics and dependencies. A more in-depth study will be carried out in further investigations using the DFT VASP methods.

4. CONCLUSION

Performed modelling and calculations presented in this study directly show that the band gap E_g of the MoS₂ layer is strongly affected by external electric field. The E_g changes are influenced, controlled and regulated by the electric field formed by a polarization in the ferroelectric polymer layers such as PVDF and its copolymers P(VDF-TrFE) depending on the discussed distance d . The electric field formed in the ferroelectric layers strongly affects the band gap E_g of the MoS₂ layered structure. The nano-size devices created on the basis of such hybrid nano-structures can be considered as the prototypes of the photodetectors and other photosensitive units for numerous practical applications. Further studies based on the most powerful DFT software (such as VASP, etc.) will open many new features for fundamental knowledges and practical usage.

ACKNOWLEDGEMENTS

The authors are greatly thankful to the Russian Foundation for Basic Researches (RFBR): grants # 19-01-00519_A and # 20-51- 53014_ A. The authors are indebted to the Phys. Dept. of the University of Aveiro (UA), Portugal, for the opportunity of using Linux-cluster for the computational studies within the framework of non-profit Scientific Agreement between UA and IMPB/KIAM.

Prof. Xiang-Jian Meng expresses his gratitude to the National Natural Science Foundation of China (NNSFC) for grant # 61574151 and Prof. Hong Shen – for grant # 62011530043.

REFERENCES

[1] A. Eftekhari. Tungsten dichalcogenides (WS₂, WSe₂, and WTe₂): materials chemistry and applications. *Journal of Materials Chemistry A*, **5** (35), 18299–18325 (2017).

[2] A. Splendiani, L. Sun, Y. Zhang, T. Li, J. Kim, C. Y. Chim, G. Galli, F. Wang. Emerging Photoluminescence in Monolayer MoS₂. *Nano Letters*, **10** (4), 1271–1275 (2010).

[3] O. Lopez-Sanchez, D. Lembke, M. Kayci, A. Radenovic, A. Kis. Ultrasensitive photodetectors based on monolayer MoS₂. *Nature Nanotechnology*, **8** (7), 497–501 (2013).

[4] Xudong Wang, Peng Wang, Jianlu Wang, Weida Hu, Xiaohao Zhou, Nan Guo, Hai Huang, Shuo Sun, Hong Shen, Tie Lin, Minghua Tang, Lei Liao, Anquan Jiang, Jinglan Sun, Xiangjian Meng, Xiaoshuang Chen, Wei Lu, and Junhao Chu. Ultrasensitive and Broadband MoS₂ Photodetector Driven by Ferroelectrics. *Adv. Mater.*, **27**, 6575–6581 (2015).

[5] Xudong Wang, Hong Shen, Yan Chen, Guangjian Wu, Peng Wang, Hui Xia, Tie Lin, Peng Zhou, Weida Hu,* Xiangjian Meng, Junhao Chu, and Jianlu Wang. Multimechanism Synergistic Photodetectors with Ultrabroad Spectrum Response from 375 nm to 10 μm. *Adv. Sci.*, **6**(15), 1901050 (2019).

[6] A. K. Geim. Graphene: Status and Prospects. *Science*, **324**, 1530–1534 (2009).

[7] X. Li, L. Tao, Z. Chen, H. Fang, et. al. Graphene and related two-dimensional materials: Structure-property relationships for electronics and optoelectronics. *Appl. Phys. Rev.*, **4**, 021306 (2017).

[8] A. K. Geim, I. V. Grigorieva. Van der waals heterostructures. *Nature*, **499**, 419–425 (2013).

[9] M. E. Lines, A. M. Glass. Principles and Applications of Ferroelectrics and Related Materials. Oxford: Clarendon (1977).

[10] T. T. Wang, J. M. Herbert, A. M. Glass. The Applications of Ferroelectric Polymers. New York: Chapman and Hall (1988).

[11] H. S. Nalwa. Ferroelectric Polymers. New York: Marcel Dekker (1995).

[12] A.V. Bune, Ch. Zhu, S. Ducharme, L. M. Blinov, V. M. Fridkin, S. P. Palto, N. G. Petukhova, S. G. Yudin. Piezoelectric and pyroelectric properties of ferroelectric Langmuir-Blodgett polymer films. *J. Appl. Phys.*, **85**, 7869 (1999).

[13] A. V. Bune, V. M. Fridkin, S. Ducharme, L. M. Blinov, S. P. Palto, A. V. Sorokin, S. G. Yudin, A. Zlatkin. Two-dimensional ferroelectric films. *Nature (London)*, **391**, 874-877 (1998).

[14] L.M. Blinov, V.M. Fridkin, S.P. Palto, A.V. Bune, P.A. Dowben, S. Ducharme, Two-dimensional ferroelectrics, *Physics-Uspeski* **43**, 243–257 (2000).

[15] V. Fridkin, S. Ducharme. Ferroelectricity at the Nanoscale. Basics and Applications. Berlin: Springer-Verlag (2014).

[16] V. S. Bystrov and V. M. Fridkin. Domain and homogeneous switching in ferroelectrics. On the 75th anniversary of the Landau–Ginzburg theory of ferroelectricity. *Ferroelectrics*, (2020).

[17] V. S. Bystrov, V. M. Fridkin. Two-dimensional ferroelectrics and homogeneous switching. To the 75th anniversary of the Landau—Ginzburg theory of ferroelectricity. *Phys. Usp.*, **63**, 417–439 (2020).

[18] E. Paramonova, V. Bystrov, Xiangjian Meng, Hong Shen, Jianlu Wang, V. Fridkin. Polarization switching in 2D nanoscale ferroelectrics: Computer simulation and experimental data analysis. *Nanomaterials*, **10** (9), 1841 (2020).

- [19] V. S. Bystrov, E. V. Paramonova, I. K. Bikin, A. V. Bystrova, R. C. Pullar, A. L. Kholkin. Molecular modeling of the piezoelectric effect in the ferroelectric polymer poly(vinylidene fluoride) (PVDF). *J. Mol. Model.*, **19**, 3591–3602 (2013).
- [20] V. S. Bystrov. Molecular modeling and molecular dynamic simulation of the polarization switching phenomena in the ferroelectric polymers PVDF at the nanoscale. *Physica B: Condensed Matter*, **432**, 21–25 (2014).
- [21] E.V. Paramonova, S.V. Filippov, V.E.Gevorkya, L.A. Avakyan, X.J.Meng, B.B. Tian, J.L. Wang and V.S. Bystrov. Polarization switching in ultrathin polyvinylidene fluoride homopolymer ferroelectric films. *Ferroelectrics*, **509**, 143–157, (2017).
- [22] V. S. Bystrov, E. V. Paramonova, A. V. Bystrova, V. E. Gevorkyan, X. J. Meng, B. B. Tian, J. L. Wang, L. A. Avakyan. Analysis of the computational and experimental studies of the polarization switching in the PVDF and P(VDF-TrFE) ferroelectric films at the nanoscale. *Mathematical Biology and Bioinformatics*, **10** (2), 372-386 (2015).
- [23] V. S. Bystrov, I. K. Bdkin, M. V. Silibin, D. V. Karpinsky, S. A. Kopyl, G. Goncalves, A. V. Saponova, T. Kuznetsova, V. V. Bystrova. Graphene/Graphene oxide and polyvinylidene fluoride polymer ferroelectric composites for multifunctional applications. *Ferroelectrics*, **509**, 124–142, (2017).
- [24] M. V. Silibin, V. S. Bystrov, D. V. Karpinsky, N. Nasani, G. Goncalves, I. M. Gavrilin, A. V. Solnyshkin, P. A. A. P. Marques, B. Singh, I. Bdkin. Local mechanical and electromechanical properties of the P(VDF-TrFE)-graphene oxide thin films. *Applied Surface Science*, **421**, Part A, 42-51 (2017).
- [25] V. S. Bystrov, I. K. Bdkin, M. V. Silibin, D. Karpinsky, S. Kopyl, E. V. Paramonova, G. Goncalves. Molecular modeling of the piezoelectric properties in the Graphene/Graphene oxide and polyvinylidene fluoride (PVDF) polymer ferroelectric composites. *J. Mol. Mod.*, **23**, 128 (14 pages) (2017).
- [26] V. S. Bystrov, M. V. Silibin, X. J. Meng, T. Lin, H. Shen, B. Tian, J. L. Wang, D. V. Karpinsky, A. V. Bystrova, E. V. Paramonova. Modelling of the Piezoelectric and Pyroelectric properties of the Ferroelectric composites thin films based on the polyvinylidene fluoride (PVDF) with Graphene and Graphene Oxide layers and fibers. *Nanomaterials Science & Engineering*, **2** (2), 83-92 (2020).
- [27] V. S. Bystrov, I. K. Bdkin, M. V. Silibin, X. J. Meng, T. Lin, J. L. Wang, D. V. Karpinsky, A. V. Bystrova, E. V. Paramonova. Pyroelectric properties of the ferroelectric composites based on the polyvinylidene fluoride (PVDF) with graphene and graphene oxide. *Ferroelectrics*, **541**, 17–24 (2019).
- [28] L. A. Avakyan, E. V. Paramonova, J. Coutinho, S. Öberg, V. S. Bystrov, L. A. Bugaev. Optoelectronics and defect levels in hydroxyapatite by first-principles. *J. Chem. Phys.*, **148**, 154706 (12 pages). (2018).
- [29] V. S. Bystrov, L. A. Avakyan, E. V. Paramonova, J. Coutinho. Sub-Band Gap Absorption Mechanisms Involving Oxygen Vacancies in Hydroxyapatite. *J. Chem. Phys. C.*, **123** (8), 4856–4865 (2019).
- [30] V. S. Bystrov, J. Coutinho, L. A. Avakyan, A. V. Bystrova and E. V. Paramonova. Piezoelectric, ferroelectric, and optoelectronic phenomena in hydroxyapatite with various defect levels. *Ferroelectrics*, Vol. **559** (1), pp. 45-55 (2020).
- [31] V. S. Bystrov, H. Shen, X. J. Meng. Modeling of dichalcogenide MoS₂ monolayers and its composites with PVDF/P(VDF-TrFE). In: 2nd International Conference on Nanomaterials Science and Mechanical Engineering. Book of Abstracts. (University of Aveiro, Portugal, July 9-12, 2019). Editors: I. Bdkin, B.Singh, R. Simoes. Publisher: UA Editora, Universidade de Aveiro (2019). - pages 163-164. ISBN 978-9732-789-544-1
- [32] A. Ramasubramaniam, D. Naveh and E. Towe. Tunable band gaps in bilayer transition-metal dichalcogenides. *Phys. Rev. B*, **84**, 205325 (2011).
- [33] N. Zibouche, P. Philippsen, A. Kuc and T. Heine. Transition-metal dichalcogenide bilayers: Switching materials for spintronic and valleytronic applications. *Phys. Rev. B*, **90**, 125440 (2014).
- [34] T. Wozniak, P. Scharoch and M.J. Winiarski. Structural Parameters and Electronic Structure of Monolayers of Transition Metal Dichalcogenides from *Ab Initio* Calculations. *ACTA PHYSICA POLONICA A*, **129** (1A), A56-A58 (2016).
- [35] Yunguo Li, Yan-Ling Li, C.M. Araujo, W. Luo and R. Ahuja. Single-layer MoS₂ as an efficient photocatalyst. *Catal. Sci. Technol.*, **3**, 2214 (2013).
- [36] C. Ataca and S. Ciraci. Dissociation of H₂O at the vacancies of single-layer MoS₂. *Phys. Rev. B*, **85**, 195410 (2012).
- [37] Guangjian Wu, Xudong Wang, Yan Chen, Shuaiqin Wu, Binmin Wu, Yiyang Jiang, Hong Shen, Tie Lin, Qi Liu, Xinran Wang, Peng Zhou, Shantao Zhang, Weida Hu, Xiangjian Meng, Junhao Chu, and Jianlu Wang. MoTe₂ p–n Homojunctions Defined by Ferroelectric Polarization. *Adv. Mater.*, 1907937 (2020).
- [38] Dan Li, Xudong Wang, Yan Chen, Sixin Zhu, Fan Gong, Guangjian Wu, Caimin Meng, Lan Liu, Lin Wang, Tie Lin, Shuo Sun, Hong Shen, Xingjun Wang, Weida Hu, Jianlu Wang, Jinglan Sun, Xiangjian Meng and Junhao Chu. The ambipolar evolution of a high-performance WSe₂ transistor assisted by a ferroelectric polymer. *Nanotechnology*, **29**, 105202 (2018).
- [39] Yan Chen, Chong Yin, Xudong Wang, Yiyang Jiang, Haoliang Wang, Binmin Wu, Hong Shen, Tie Lin, Weida Hu, Xiangjian Meng, Piyi Du, Junhao Chu, Zongrong Wang, and Jianlu Wang, Multimode Signal Processor Unit Based on the Ambipolar WSe₂-Cr Schottky Junction. *ACS Applied Materials & Interfaces*, **11**(42), 38895-38901 (2019).
- [40] VASP (Vienna Ab initio Simulation Package). Available online: <https://www.vasp.at/> (accessed on 17 November 2020).
- [41] G. Kresse, J. Furthmüller. Efficient iterative schemes for ab initio total-energy calculations using a plane-

- wave basis set. *Phys. Rev. B Condens. Matter Mater. Phys.*, **54**, 11169–11186 (1996).
- [42] G. Kresse, D. Joubert. From ultrasoft pseudopotentials to the projector augmented-wave method. *Phys. Rev. B Condens. Matter Mater. Phys.*, **59**, 1758–1775 (1999).
- [43] J. P. Perdew, K. Burke, M. Ernzerhof. Generalized Gradient Approximation Made Simple. *Phys. Rev. Lett.*, **77**, 3865–3868 (1996).
- [44] J. Paier, R. Hirschl, M. Marsman, G. Kresse. The Perdew-Burke-Ernzerhof exchange-correlation functional applied to the G2-1 test set using a plane-wave basis set. *J. Chem. Phys.* **122**, 234102 (2005).
- [45] P. E. Blochl. Projector augmented-wave method. *Phys. Rev. B Condens. Matter Mater. Phys.*, **50**, 17953–17979 (1994).
- [46] S. Grimme, J. Antony, S. Ehrlich, S. Krieg. A consistent and accurate ab initio parametrization of density functional dispersion correction (dft-d) for the 94 elements H-Pu. *J. Chem. Phys.*, **132**, 154104 (2010).
- [47] H. J. Monkhorst, J. D. Pack. Special points for Brillouin-zone integrations. *Phys. Rev.*, **13**, 5188–5192 (1976).
- [48] D. Yang, S. Jiménez Sandoval, W. M. R. Divigalpitiya, J. C. Irwin, and R. F. Frindt. Structure of single-molecular-layer MoS₂. *Phys. Rev. B*, **43**, 12053 (1991).
- [49] Hypercube Inc. HyperChem, versions 7.51 and 8.0; Hypercube Inc.: Gainesville, FL, USA, 2002. Available online: <http://www.hyper.com/?tabid=360> (accessed on 7 November 2020).
- [50] J. J. P. Stewart. Optimization of Parameters for Semiempirical Methods. I. Method. *J. Comput. Chem.*, **10**(2), 209–220 (1989).
- [51] J. J. P. Stewart. Optimization of parameters for semiempirical methods. II. Applications. *J. Comput. Chem.*, **10**(2), 221–264 (1989).
- [52] J. J. P. Stewart. Optimization of parameters for semiempirical methods V: modification of NDDO approximations and application to 70 elements. *J. Mol. Mod.*, **13**(12), 1173–1213 (2007).
- [53] M. J. S. Dewar, E. G. Zoebisch, E. F. Healy, J. J. P. Stewart. Development and use of quantum-mechanical molecular models. 76. AM1: A new general purpose quantum mechanical molecular model. *J. Am. Chem. Soc.*, **107**, 3902–3909 (1985).
- [54] W. P. Anderson, W. D. Edwards, M. C. Zerner. Calculated spectra of hydrated ions of the first transition-metal series. *Inorg. Chem.*, **25**, 2728–2732 (1986).
- [55] L. A. Carreira, W. B. Person. INDO (intermediate neglect of differential overlap) calculations of properties of molecular complexes. *J. Am. Chem. Soc.*, **94**(5), 1485-1495 (1972).
- [56] E. Scalise, M. Houssa, G. Pourtois, V. Afanas'ev, A. Stesmans. Strain-Induced Semiconductor to Metal Transition in the Two-Dimensional Honeycomb Structure of MoS₂. *Nano Res.* **5** (1), 43-48 (2012).
- [57] X. Chen, Z. Wu, S. Xu, et al. Probing the electron states and metal-insulator transition mechanisms in molybdenum disulphide vertical heterostructures. *Nat. Commun.*, **6**, 6088 (2015).
- [58] E. J. G. Santos, E. Kaxiras. Electrically Driven Tuning of the Dielectric Constant in MoS₂ Layers. *ACS Nano*, **7** (12), 10741-10746 (2013).

Nanomaterials Science & Engineering (NMS&E), Vol.2, No.4, 2020

**Department of Mechanical Engineering
University of Aveiro
Aveiro 3810-193
Portugal**

<https://proa.ua.pt/index.php/nmse/>

ISSN: 2184-7002